DI Patrick Kraus, BSc

Classical and quantum-mechanical atom-surface interaction models applied to He-scattering measurements on Bi(111) and Sb(111) surfaces

DOCTORAL THESIS

For obtaining the academic degree
Doktor der technischen Wissenschaften

Doctoral Programme of Technical Sciences
Technical Physics

Graz University of Technology

Supervisor:
Univ.-Prof. Mag. Dr.rer.nat Wolfang E. Ernst
Institute of Experimental Physics

Graz, July 2014

There is a theory which states that if ever anyone discovers exactly what the Universe is for and why it is here, it will instantly disappear and be replaced by something even more bizarre and inexplicable. There is another theory which states that this has already happened.

Douglas Adams, The Restaurant at the End of the Universe

Abstract

Angular helium atom scattering measurements reveal small variations of the background intensity in between the elastic scattering positions. The observed discrete features are remnants of the attractive interaction between the helium particle and the sample surface. These selective adsorption features have been analyzed for angular spectra on the Bi(111) and Sb(111) surfaces to determine analytical expressions for the interaction potential shape. The exact positions of the interaction potentials bound state energies were used to selectively enhance the inelastic signal in the high-energy phonon creation side of HAS-time-of-flight measurements. This way, the surface and subsurface optical phonon modes on the Bi(111) surface were clearly distinguished from the background noise. To furthermore include the potential shapes into the corrugation analysis, a close-coupling code was implemented and applied to the angular scattering spectra of Sb(111). Effective corrugation heights between 9.5 % and 12.4 % of the lattice constant, dependent on the interaction potential used, have been determined. It was additionally found that the plain corrugated Morse interaction potential can neither describe the second order scattering interactions in $\overline{\Gamma M}$-, nor any scattering in $\overline{\Gamma K}$-direction, while the hybrid Morse potential succeeds at these cases, too. Because of the importance of the potential shape, a comparative study of different interaction potentials in close-coupling calculations on the Sb(111) surface has been conducted. Within this study, a different approach for determining the potential parameters from the measured bound state energies has been applied and the whole spectrum of interaction potentials used gave rise to corrugation heights between 13.65 % and 19.05 % of the lattice constant dependent on the potential in use. In general, hybrid-Morse interaction potentials yielded the best results, while the plain corrugated Morse potential still fails. To additionally eradicate the quietly accepted Debye-Waller model for describing the thermal intensity attenuation, the close-coupling formalism was extended to include phononic movement of the surface atomic positions. The obtained code was applied to angular scattering spectra of the Bi(111) surface. It was found that the measured scattering intensities can be described using much lower corrugation heights if phononic interaction is included. The corrugation heights obtained using either approximative methods or the quantum mechanically exact inelastic close-coupling formalism are ≈ 10 % and 6.32 %, respectively. A more striking finding is furthermore that in the inelastic formalism the problems encountered with plain corrugated Morse potentials vanish, and the intensity prediction fits the measured values exceedingly well.

Kurzfassung

Winkelaufgelöste Helium-Streuspektren zeigen kleine Intensitätsvariationen im Hintergrundsignal zwischen den elastischen Streupositionen. Diese Signale werden durch das attraktive Interaktionspotential zwischen dem Heliumkern und der Probe verursacht. Diese *selektiven Adsorptionssignale* wurden aus angularen Spektren von Sb(111) und Bi(111) extrahiert und dazu benutzt, analytische Ausdrücke für die Form der jeweiligen Interaktionspotentiale zu ermitteln. Das Wissen um die genauen Energien der gebundenen Zustände konnte zur selektiven Verstärkung des inelastischen Signals höherenergetischer Phononenerzeugung in Streuungs-Flugzeitmessungen genutzt werden. Auf diesem Weg konnten die Oberflächenvibrationen - und auch darunter liegende Moden im Bereich optischer Phononenenergien eindeutig aus dem ansonsten stark verrauschten Hintergrund hervorgehoben und gemessen werden. Um diese weichen Potentiale weiters in die Berechnung der Oberflächenwelligkeit miteinfließen lassen zu können, wurde ein sogenannter *close-coupling* Code implementiert und auf die Sb(111) Messungen angewandt. Abhängig vom verwendeten Interaktionspotential wurden Welligkeitshöhen von 9.5 % bis 12.5 % der Gitterkonstante ermittelt. Es wurde weiters festgestellt, dass das *Corrugated Morse potential* nicht in der Lage zu sein scheint, Streuintensitäten zweiter Ordnung in $\overline{\Gamma\mathrm{M}}$- sowie irgendeine Streuintensität in $\overline{\Gamma\mathrm{K}}$-Richtung zu reproduzieren, während das modifizierte *hybrid Morse potential* diese Probleme nicht aufzeigt. Angeregt durch diese Hinweise auf die Wichtigkeit der benutzten Potentialform wurde eine vergleichende Studie der vorhergesagten Streuintensitäten aus dem *close-coupling* Formalismus auf der Sb(111) Oberfläche bei verschiedenen Interaktionspotentialen durchgeführt. Während dieser Studie wurde ein alternativer Algorithmus verwendet, um die Fitparameter für die Interaktionspotentiale zu ermitteln. Das gesamte Spektrum der betrachteten Interaktionspotentiale führte zu Welligkeitshöhen zwischen 13.65 % und 19.05 % der Gitterkonstante. Generell erzielten die hybrid-Morse Interaktionspotentiale die besten Ergebnisse, während das einfache *corrugated Morse potential* die selben Probleme wie zuvor aufwies. Um des Weiteren den stillschweigend akzepierten Debye-Waller Faktor, welcher den Intensitätsverlust der Streupeaks durch thermische Oberflächenschwingungen erklären soll, zu umgehen, wurde der *close-coupling* Formalismus auf phononische Vibration der Gitteratome erweitert. Das so erhaltene Programm wurde auf die angularen Streuspektren der Bi(111) Oberfläche angewendet. Durch diese Vorgehensweise konnten die erhaltenen Streuspektren mit viel kleineren Werten der Oberflächenwelligkeit erklärt werden. Verglichen mit den approximativen Methoden konnte die angenommene Höhe der Ober-

flächenwelligkeit von $\approx$ 10 % auf 6.32 % abgesenkt werden. Ein weiterer Vorteil der inelastischen Betrachtung ist, dass unter Inklusion der inelastischen Effekte die zuvor erwähnten Probleme des einfachen Morsepotentials die Streuintensitäten höherer Ordnung zu beschreiben, verschwinden und auch diese höheren Ordnungen sehr gut beschrieben werden.

Articles related to this work

(1) Vibrational dynamics and surface structure of Bi(111) from helium atom scattering measurements
Michael Mayrhofer-Reinhartshuber, Anton Tamtögl, **Patrick Kraus**, Karl-Heinz Rieder and Wolfgang E. Ernst
Journal of Physics: Condensed Matter, **24**:104008 (2012)

(2) Surface and subsurface phonons of Bi(111) measured with helium atom scattering
Anton Tamtögl, **Patrick Kraus**, Michael Mayrhofer-Reinhartshuber, Davide Campi, Marco Bernasconi, Giorgio Benedek and Wolfgang E. Ernst
Phys. Rev. B, **87**:035410 (2013)

(3) Resonance-enhanced inelastic He-atom scattering from sub-surface optical phonons of Bi(111)
Patrick Kraus, Anton Tamtögl, Michael Mayrhofer-Reinhartshuber, Giorgio Benedek, and Wolfgang E. Ernst
Physical Review B, **87**:245433 (2013)

(4) Surface Debye temperature and vibrational dynamics of Antimony(111) from helium atom scattering measurements
Anton Tamtögl, Michael Mayrhofer-Reinhartshuber, **Patrick Kraus** and Wolfgang E. Ernst
Surf. Sci., **617**:225-228 (2013)

(5) Helium Atom Scattering Investigation of the Sb(111) Surface
Michael Mayrhofer-Reinhartshuber, Anton Tamtögl, **Patrick Kraus** and Wolfgang E. Ernst
Journal of Physics: Condensed Matter, **25**:395002 (2013)

(6) The Helium-Surface Interaction Potential of Sb(111) from Scattering Experiments and Close-Coupling Calculations
Michael Mayrhofer-Reinhartshuber, **Patrick Kraus**, Anton Tamtögl, S. Miret-Artés and Wolfgang E. Ernst
Phys. Rev. B, **88**:205425 (2013)

(7) A Comparative Study of the He-Sb(111) Interaction Potential from Close-Coupling Calculations and Helium Atom Scattering Experiments
Patrick Kraus, Michael Mayrhofer-Reinhartshuber, Ch. Gösweiner, F. Apolloner, Salvador Miret-Artés and Wolfgang E. Ernst
Submitted to Surface Science

(8) The surface structure of Bi(111) calculated from Helium Atom Scattering measurements using the inelastic Close Coupling formalism
Patrick Kraus, Anton Tamtögl, Michael Mayrhofer-Reinhartshuber, F. Apolloner, Ch. Gösweiner, Salvador Miret-Artés and Wolfgang E. Ernst *submitted to Phys. Rev. B*

Notes: The articles (3), (7) and (8) are contained in this work. As this work is based on the description of interaction processes in gas-surface scattering interactions, the reader interested in elastic properties of antimony as well as the elastic and inelastic properties of bismuth is refered to the PhD thesis of MICHAEL MAYRHOFER-REINHARTSHUBER and the PhD thesis of ANTON TAMTÖGL, respectively. The work of AT furthermore contains a much more detailed description of the apparatus used for the measurements presented in these papers as well as in the rest of this thesis.

EIDESSTATTLICHE ERKLÄRUNG

AFFIDAVIT

Ich erkläre an Eides statt, dass ich die vorliegende Arbeit selbstständig verfasst, andere als die angegebenen Quellen/Hilfsmittel nicht benutzt, und die den benutzten Quellen wörtlich und inhaltlich entnommenen Stellen als solche kenntlich gemacht habe. Das in TUGRAZonline hochgeladene Textdokument ist mit der vorliegenden Dissertation identisch.

I declare that I have authored this thesis independently, that I have not used other than the declared sources/resources, and that I have explicitly indicated all material which has been quoted either literally or by content from the sources used. The text document uploaded to TUGRAZonline is identical to the present doctoral dissertation.

Datum / Date

Unterschrift / Signature

Contents

List of Figures

1 Introduction

With the advent of two-dimensional materials and the development of materials with special surface restricted properties such as the class of topological insulators, the quality of analysis of surface specific measurements is facing more and more extreme demands. Obviously, it is beneficial if the measurement method used is surface specific from the beginning, so bulk values will not mix into the desired measurements. It is this surface sensitivity at which helium atom scattering (HAS) excels. While the probe particles of other scattering methods as neutron or electron scattering penetrate the surface at least a few layers even at low energies, low-energetic helium atoms are already repelled from the electron density 2-3 Å above the first atomic layer. The features recorded from HAS are thus completely dependent on the electron density variations above the surface and do in general not depend on bulk properties. A surface sensitivity like this is otherwise only achieved with the most sophisticated Atomic-Force-Microscopy (AFM) methods. AFM on the other hand can not easily supply information on the phononic dispersion of the underlying material. Measurement techniques capable of this difficult analysis are usually slightly destructive at least - depending on the kinetic energies used in the measurements. The most commonly utilized probe particle for investigating phononic dispersions are neutrons. While possessing an equally usable probability for interacting with single-phonon processes, neutrons generally have a very low probability to interact with matter, resulting in extreme penetration depths. It is therefore exceedingly hard to deduct surface specific properties from neutron scattering experiments. The extreme surface sensitivity, paired with the gentle surface treatment and the possibility to probe not only surface structure and dynamics, but also the interaction with the probe particle itself renders HAS an indispensable tool for any serious material property analysis.
It is hard to overestimate the importance of surface properties. All physical interactions between materials, all chemical processes using a catalysator take place at materials surfaces. The exact structure as well as the interaction between the surface and the interacting particles take important roles in these procedures. It is the exact structural corrugation and electronic configuration of the platinum surface that forces the adsorbed carbon-monoxide to remain in an upright position for example, enabling so many catalytic processes. Astonishingly, not much is known about the exact structural parameters of material surfaces, especially for the semimetal surfaces that have been under investigation in this thesis. The determination of surface properties is without doubt a complex problem. While theorists struggle with broken periodicities and large

vacuum layers in their simulations, experimentalists struggle with preparation and contamination.
Besides posing a certain challenge to experimental surface scientists, the surfaces of the semimetals bismuth (Bi) and antimony (Sb) have received renewed interest over the last couple of years. One of the most difficult problems was the determination of the Bi(111) acoustic phonon dispersion with the Bi(111)-Rayleigh branch peaking at an energy of only 3.5 meV. Naturally, the corresponding measurements contained multiple overlapping features which rendered the analysis a nontrivial task. The distinction of the measured phonon peaks as well as the identification of features attributed to other effects than phononic movement introduced the necessity of more refined analysis tools. Up to then the interaction between the probe particle and the surface was assumed to be of a hard-wall type and related approximative methods for describing the measured elastic scattering peaks delivered satisfying results. This hard-wall type however could not account for a lot of the measured features in the angular as well as in the time-of-flight measurements. The soft interaction potential between the particle and the surface harbors certain bound state energies which are responsible for so-called *selective adsorption resonances* (see section 3.8). If the resonance conditions are met, a certain position in the angular or the time-of-flight measurements can be selectively enhanced to accurately pinpoint the phononic interaction energy or related effects. Chapter 5 presents a publication where this effect was utilized to selectively enhance the optical phonon modes on the Bi(111) surface. The very same resonant effects however can alter the measured elastic intensities and thus lead to an erroneous estimation of the surface corrugation (see section 3.9). To include the newly found interaction potentials into the corrugation calculations, the quantum mechanically exact close-coupling formalism was introduced (see section 3.9.4) and utilized to analyze not only the surface corrugation of Sb (see chapter 6), but also to further refine our understanding of the interaction potential shape between the related scattering objects (see chapter 7). The very same formalism can be alterated to furthermore include inelastic contributions present due to the thermal vibrations of the lattice ions. This so-called inelastic close-coupling formalism was introduced to describe the surface corrugation of Bi(111), since due to its comparatively low surface Debye temperature of 84 K the usually applied Debye-Waller (DW) attenuation (see section 3.9.5) does not yield comparable results, ignoring the fact that this theory was developed for x-ray scattering on ionic bulk crystals which may not be applicable to HAS on semimetal surfaces. The inelastic close-coupling analysis however succeeds in describing the scattering spectrum on the surface (see chapter 8) and finally resolves the mystery why semimetallic surfaces like Sb(111) and Bi(111) seem to be highly corrugated while possessing conducting surface states.

1.1 Organization of this Thesis

This work is designed as a cumulative thesis, i.e. the main scientific results are presented in their original form as articles - published or under review - in peer-reviewed journals (chapters 5, 7 and 8). Each chapter corresponding to such a publication is introduced with a short description and listing of the contributions of the several authors. To protect the reader from jumping head-first into the subject of particle-surface interaction analysis and our respective measurements, chapters 2-4 try to provide a summary of the experimental and theoretical background. Subsequently, chapter 9 gives a short summary of the novel findings of this work.

2 Experimental Setup

All measurements contained in this work have been recorded on the helium atom scattering apparatus H.Å.N.S (Helium Atom Nondestructive Scattering) originally designed and built at the FU Berlin. After transfer to Graz, where the machine was remounted, characterization measurements were performed on the well-known surface of LiF[3,88]. After several adaptions and enhancements[68], a first complete analysis of the static and dynamic behavior of the Bi(111) surface was performed[55,71,88,90,91]. Further investigations revealed the static and basic dynamic properties of Sb(111)[53,68–70,92]. The following pages summarize the most important parameters of the apparatus. A much more detailed description including construction details, beam geometry and vacuum architecture is documented in the PhD thesis of Anton Tamtögl[88].

2.1 Beam Production - The Source Arm

The two chambers of the source arm contain all the necessary equipment to produce and control a nearly monoenergetic atomic beam. The gas is supplied in a reservoir kept at constant temperature and pressure (T_0, P_0) and expanded through a narrow nozzle of diameter d (typically 10 μm) into the surrounding vacuum chamber which is held at a low pressure of $p_a \leqslant 10^{-6}$ mbar. Due to the high pressure difference between the in- and the outside of the nozzle, the gas enters the chamber at a higher pressure than the ambient pressure p_a. This 'underexpanded' gas expands and consequently accelerates further into the vacuum chamber reaching high velocities. Since this expansion can be considered as very fast, the process may be assumed to be adiabatic, giving rise to transformation of thermal to translational particle energy[72,79].
The central part of the expanded beam is selected by a 'skimmer', a conical-shaped aperture between the first and the second chamber. This central part is mainly characterized by a very narrow velocity distribution width of usually $\Delta v_\parallel / v_\parallel \simeq 1\%$, with the beam reaching a final particle velocity of

$$v_\parallel = \sqrt{\frac{5 \cdot k_\mathrm{B} \cdot T_0}{m_{He}}}, \tag{2.1}$$

with k_B being Boltzmann's constant and m_{He} the atomic mass of helium. From this velocity, the relevant parameters for atomic scattering processes can easily be derived.

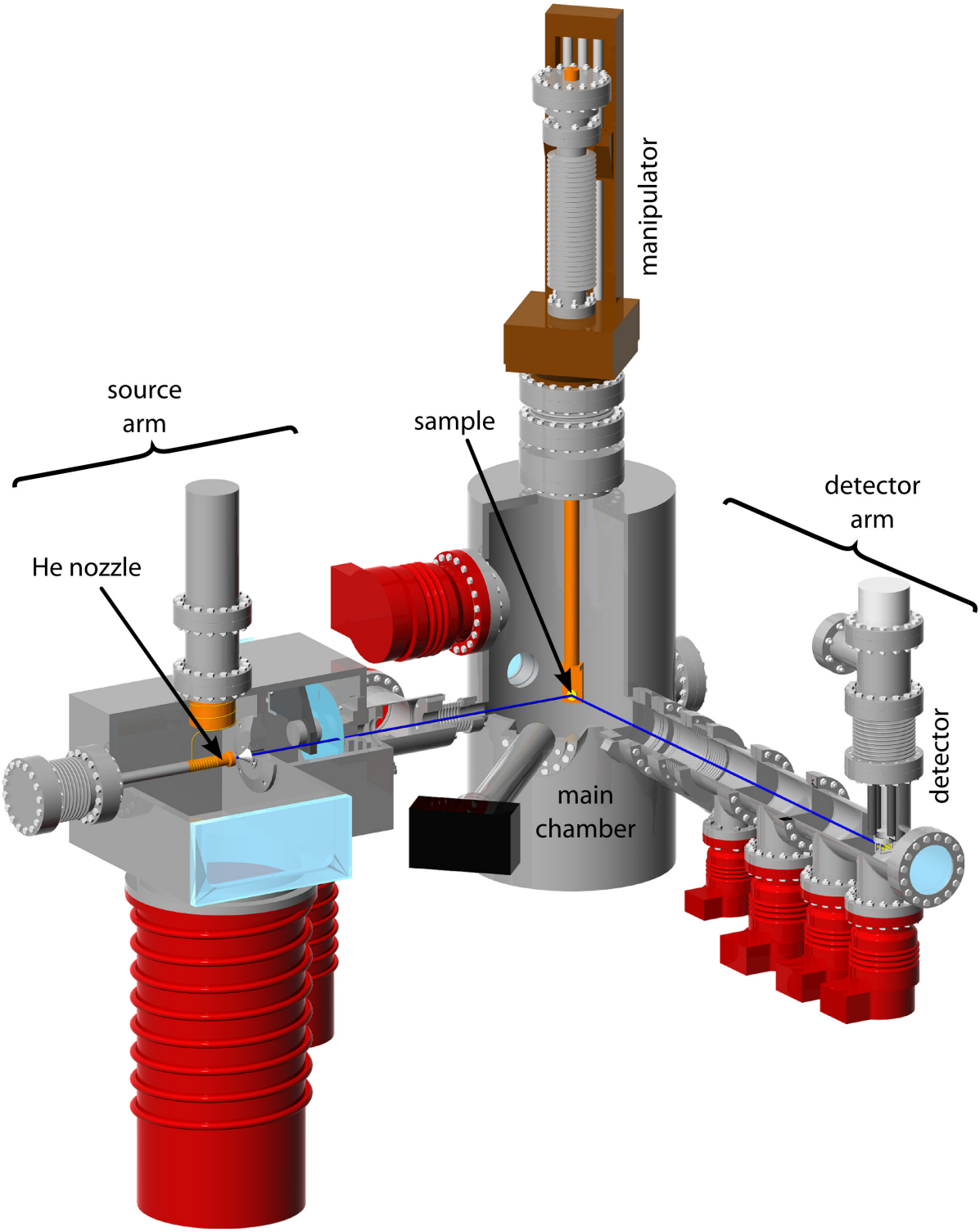

Figure 2.1: 3D representation of the used HAS apparatus. Image taken from A. Tamtögl[88]

Especially, the beam energy,

$$E_i = \frac{5}{2} k_B T_0 \tag{2.2}$$

and the related absolute value of the particle wavevector $\mathbf{k}_i$,

$$\mathbf{k}_i^2 = \frac{2m_{He}}{\hbar^2} E_i \tag{2.3}$$

are of special importance for the analysis of measurement data[88]. An important aspect of these equations is that the beam energy and thus the wavevector can be easily tuned by changing the temperature of the nozzle reservoir T_0. The present apparatus can be adjusted to stable nozzle temperatures between 60 K and 165 K, resulting in scattering energies between 13 meV and 35 meV.
After passing the skimmer, the beam enters the second chamber of the source arm, containing the rotating chopper disc. In order to perform Time-of-Flight (TOF) measurements, the particles arriving at the detector must be identified and distinguished. If a continuous beam is scattered from the sample, the intensity measured by the detector will be temporally uniform. To be able to distinguish the particles velocities, the incoming particle beam is 'chopped' into discrete packets by passing the beam through the thin slits on a rotating chopper disc. While reducing the problem of energy-sensitive measurements to the time-resolved detection of the produced packets (using a 'single-slit chopper'), this method usually reduces the total intensity of the incoming beam to about 1% of its original value, resulting in unbearably long measurement times. By using a 'pseudo-random chopper', the decline in beam intensity can be limited to about 50%. In this method, the chopper disc contains not only one or two single slits along the whole rim of the disc, but is patterned by a complete sequence of alternating broad or thin passages. The resulting signal at the detector is far more complicated, but can be described by a convolution of a single-slit signal with the known sequence of the chopper disc. Obviously, while granting the ability to perform the measurements faster by a factor of up to 50, the obtained datasets are more complicated to analyze[68].

2.2 Manipulation and Interaction - The Main Chamber

After passing through the chopper chamber, the beam is directed through an additional aperture into the main chamber (MC). Here the sample is positioned into the beamline via a seven-axis manipulator. Apart from adjusting the sample to the desired scattering position, the manipulator is also used to transfer the crystal under investigation to the target positions of the other analysis and preparation methods. The main chamber is generally kept at UHV conditions (varying in pressures between 10^{-10} and 10^{-11} mbar) to prevent the surface from getting dirty as long as possible. The residual gases within

the MC can be measured using a quadrupole mass spectrometer. For cleaning purposes, the MC is equipped with an Ar^+-ion gun for sputtering. After each sputtering cycle, the surface can be annealed using a button heater attached directly to the backside of the sample as well as a Thermocoax heating wire to heat the manipulator itself. The heating wire is wrapped around a liquid nitrogen reservoir which when in use, enables the surface to be cooled down to 100 K. To check the surface cleanliness as well as to align the crystal rotation, a combined LEED (Low-energy electron diffraction) and AES (Auger electron spectrograph) using a retarded field detector built into the LEED screen are in use.
Furthermore, the MC is supplied with a controllable source of molecular hydrogen for potential applications on metal surfaces. This source will be replaced with a combined monoatomic & molecular hydrogen source. This way, the range of materials where a hydrogen layer can be applied to is extended to semimetals and covalent crystals.

2.3 Separation and Detection - The Detector Arm

The detector arm setup is flanged to the main chamber at a total angle of 91.5° from the source arm. In this setup, the position of both arms is fixed, providing a so-called 'moving threshold' scattering geometry. The detector arm mainly consists of a differentially pumped separation stage, a straight distance the helium atoms have to traverse to arrive at the quadrupol mass spectrometer for detection. After inelastic interaction with the surface, some of the helium atoms gained or lost energy, resulting in a different total speed in comparison to the elastically scattered beam. The separation distance enables these energetic differences to spread the different helium atoms spatially. Due to this separation, the atoms arrive at the detector at different times and can be distinguished. The detector itself is mounted at a total angle of 90° with respect to the beam direction and at a total distance of 1.114 m from the sample surface. Helium atoms are ionized using a cross-beam ion source along a total ionization length of about 1 cm. While a short ionization length is beneficial for the energy resolution, it severely limits the measured intensity. The ionization length thus has to be chosen as a compromise between those two essential parameters.

3 Theoretical Background

3.1 Surface Description

Crystal structures as well as the structures of their respective surfaces have been fundamental knowledge for performing crystallographic experiments, so any attempt to be more precise in describing the fundamentals than the respective textbooks[50] would be futile. The following section summarizes the concepts needed for understanding surface scattering briefly, for a more thorough report on the concepts, the interested reader is refered to Ch. Kittel's *Introduction to Solid State Physics*[50].
A so-called *primitive* crystal is defined as a three dimensional periodic arrangement of atoms. A result of this basic periodicity is that two atoms at the positions $\mathbf{r}$ and $\mathbf{r}'$ are basically indistinguishable if $\mathbf{r}'$ can be described as

$$\mathbf{r}' = \mathbf{r} + k \cdot \mathbf{a}_1 + l \cdot \mathbf{a}_2 + m \cdot \mathbf{a}_3 \tag{3.1}$$

where (k, l, m) are integers and $(\mathbf{a}_1, \mathbf{a}_2, \mathbf{a}_3)$ the three *unit cell vectors*. The perfect crystal surface is defined as a two-dimensional cut through this perfect crystal. The specific direction the crystal is cut, produces a specific surface structure. The produced two-dimensional surface structure is usually periodic too, so the atomic positions can be described as a linear combination of *surface unit cell vectors*,

$$\mathbf{R}' = \mathbf{R} + n \cdot \mathbf{A}_1 + o \cdot \mathbf{A}_2 \tag{3.2}$$

with (n, o) integers and ($\mathbf{A}_1$,$\mathbf{A}_2$) the *surface unit cell vectors* of the two dimensional structure. Note that surface-specific quantities are usually depicted using capital letters, while lower-case names are kept for three-dimensional vectors.
The surface under investigation is usually specified using its shortest normal reciprocal lattice vector.

3.2 Reciprocal Lattice Diffraction

Out of mathematical necessity in scattering investigations, crystals are furthermore defined by their *unit cell vectors* in *reciprocal space*. These vectors are called *reciprocal*

unit cell vectors and can be calculated for any two-dimensional periodic structure using the following equations:

$$(\mathbf{B}_1, 0) \;=\; \mathbf{b}_1 \;=\; 2\pi \frac{\mathbf{A}_2 \times \mathbf{n}}{\mathbf{A}_1 \cdot (\mathbf{A}_2 \times \mathbf{n})} \tag{3.3}$$

$$(\mathbf{B}_2, 0) \;=\; \mathbf{b}_2 \;=\; 2\pi \frac{\mathbf{n} \times \mathbf{A}_1}{\mathbf{A}_1 \cdot (\mathbf{A}_2 \times \mathbf{n})} \tag{3.4}$$

with $\mathbf{n}$ being a normalized normal vector pointing outward the surface. This transformation leads to a periodic *reciprocal lattice*, where two of the *reciprocal lattice points* $\mathbf{G}$ are connected via

$$\mathbf{G}_{p,q} \;=\; \mathbf{G}_{0,0} \;+\; p \cdot \mathbf{B}_1 \;+\; q \cdot \mathbf{B}_2. \tag{3.5}$$

The three-dimensional indices of the shortest reciprocal lattice vector perpendicular to the original surface are called the surfaces *Miller indices* and are used to uniquely define the observed surface.

3.2.1 Diffraction from periodic surfaces

Diffraction occurs whenever a wave encounters a periodic structure with a lattice periodicity of comparable size as its own wavelength. The reflected (or transmitted) pattern is no longer homogeneous, but conglomerates at several specific angles. These scattering angles can be described by the *Laue-condition*, which states that the surface-parallel component of the incoming- and the outgoing beam only differ by a reciprocal lattice vector, while the total energy of the wave stays the same.

$$\mathbf{K}_i \;-\; \mathbf{K}_f \;=\; \mathbf{G}_{p,q} \tag{3.6}$$

$$E_f \;=\; E_i \tag{3.7}$$

Naturally, since every particle may be described as a traveling wave with a wavelength given by the *de Broglie* wavelength

$$\mathbf{p} \;=\; \hbar \cdot \mathbf{k}, \tag{3.8}$$

this diffraction criterion is also valid for all moving particles.

3.3 Lattice Vibrations

The straightforward model for the dynamics inside a crystal is to picture the atoms as being connected by Hookean springs. As simple as this model may be, a lot of basic physics can be derived by it.

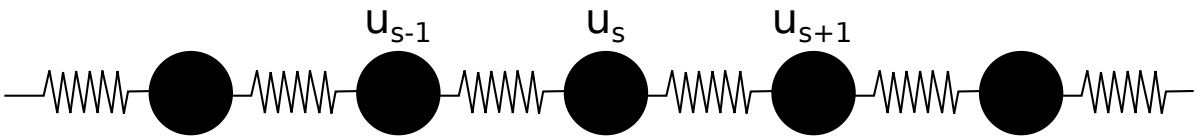

Figure 3.1: One dimensional monoatomic chain of atoms connected by Hookean springs.

3.3.1 The one-dimensional monoatomic chain

The simplest conceivable model of a dynamic crystal is the one dimensional Hookean chain, figure 3.1. We assume a linear chain of equal masses m at the lattice points connected by Hookean springs with a force constant of k and periodic boundary conditions. The lattice constant, meaning the equilibrium distance between particle u_s and u_{s+1} is a. The force on particle s due to the displacements u_s of the particles $s \pm 1$ leads to the differential equation

$$m\frac{d^2u_s}{dt^2} \;=\; k\,(u_{s+1} \;+\; u_{s-1} \;-\; 2u_s) \tag{3.9}$$

which can easily be solved by assuming a periodic time dependence $u_s(t) = e^{-i\omega t}$ and a travelling wave displacement $u_{s\pm1} = u \cdot e^{i(s\pm1)qa}$ which leads to the dispersion relation for the angular frequency

$$\omega(q) \;=\; \sqrt{\frac{4k}{m}}\left|\sin\frac{qa}{2}\right| \tag{3.10}$$

This dispersion initially starts linear at a momentum of 0, the so-called "Γ-point" and gradually flattens out to a slope of zero at the zone boundary at $q = \frac{\pi}{a}$. To describe phononic movements, Debye modeled the phonon dispersion as a straight line originating at the Γ-point and ending at the zone boundary at the *Debye-frequency* $\omega_{\mathbf{D}}$ and a phonon density of states

$$D(\omega) \;=\; \frac{3\omega^2}{\omega_{\mathbf{D}}^3}. \tag{3.11}$$

Using this Debye model, the *Debye-Temperature* $\Theta_{\mathbf{D}}$ can be defined. At the *Debye-Temperature* $\Theta_D = \frac{\hbar\omega_{\mathbf{D}}}{k_{\mathbf{B}}}$, all the possible phonon states in the Debye-dispersion are populated. This *Debye-Temperature* is a specific property of the material and generally lower in heavier materials.

3.3.2 The one-dimensional diatomic chain

The character of the phononic dispersion fundamentally changes when there are two distinguishable atoms u and v with the masses m_1 and m_2 in the unit cell, figure 3.2. In the one dimensional picture, every atom is surrounded by two atoms of the other kind at a respective distance of $a/2$, resulting in a system of coupled differential equations

$$m_1\frac{d^2u_s}{dt^2} \;=\; k\,(v_s \;+\; v_{s-1} \;-\; 2u_s) \tag{3.12}$$

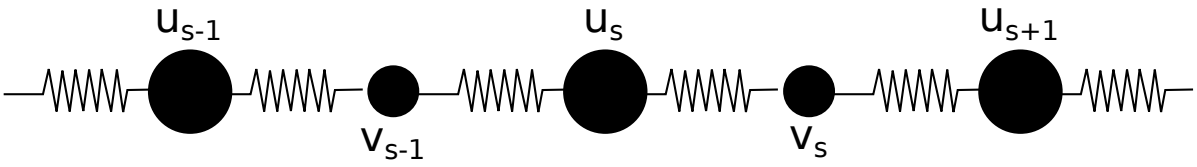

Figure 3.2: One dimensional diatomic chain of atoms connected by Hookean springs.

$$m_2 \frac{d^2 v_s}{dt^2} \;=\; k\,(u_{s+1} \;+\; u_s \;-\; 2v_s) \tag{3.13}$$

which leads to a somewhat more complicated dispersion

$$\omega_{\pm}^2 \;=\; k\left[\left(\frac{1}{m_1} \;+\; \frac{1}{m_2}\right) \;\pm\; \sqrt{\left(\frac{1}{m_1} \;+\; \frac{1}{m_2}\right)^2 \;-\; \frac{4}{m_1 m_2}\sin^2\left(\frac{qa}{2}\right)}\right]. \tag{3.14}$$

The dispersion given by equation 3.14 is now divided into two branches, as can be clearly seen in figure 3.3(a). The lower branch, the *acoustic phonon branch* resembles the mode obtained by calculating the dispersion of the monoatomic chain and exhibits clearly the initial *Debye*-behavior. The second mode, the *optical phonon branch* is separated from the acoustical mode by a bandgap. The magnitude of this gap is dependent on the mass-difference between the two distinguishable atoms. If the atoms possess the same mass, the bandgap vanishes - however, since the differing mass was the only difference between the two atoms in our model, the atoms are then indistinguishable and the corresponding lattice constant is reduced from a to $a/2$. This results in the shift of the effective zone boundary from π/a to $2\pi/a$. This way, as depicted in figure 3.3(b) and (c), the optical branch vanishes and is therefor a specific effect of distinguishable atoms inside a crystallographic unit cell.

3.3.3 The two-dimensional close-packed lattice

To extend the previous models to a complete approximative model for two- and three dimensional crystals, a slightly more sophisticated approach is imperative. We assume a crystal containing N crystal cells, each containing r ions with their respective masses M_α. The equilibrium position of each ion in this crystal lattice can thus be described as

$$\mathbf{R}_{n,\alpha} \;=\; \mathbf{R}_n \;+\; \mathbf{R}_\alpha \tag{3.15}$$

with n and α running from 1 to N and 1 to r, respectively. The distance of each ion with respect to its equilibrium position is denoted as $s_{n,\alpha}(t)$, its sub-component, the distance from the equilibrium position in k-direction, as $s_{n,\alpha,k}(t)$, with k running through the observed number of dimensions K. As usual in classical mechanics, the first things

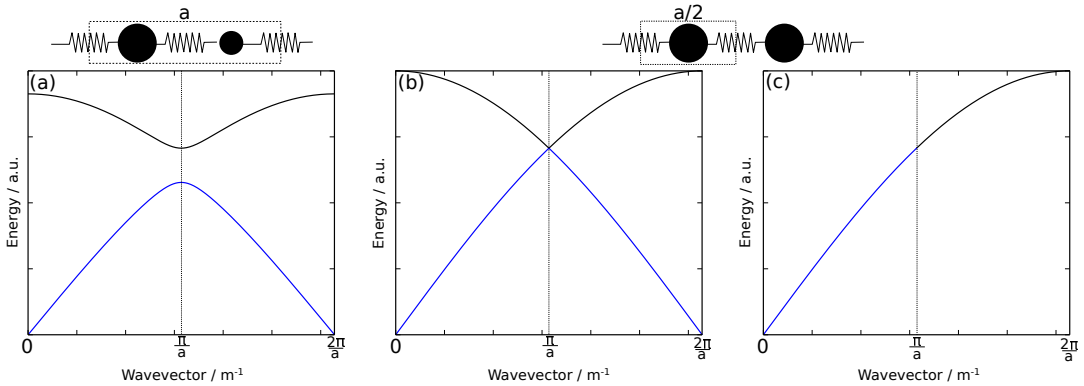

Figure 3.3: Schematic representation of the appearance of the optical phonon band. (a) The unit cell contains two distinguishable lattice atoms. The unit cells size is a - thus the reciprocal zone boundary lies at $\frac{\pi}{a}$. (b) Assume the two atoms in the large unit cell are equal in mass and force constants, but the observed unit cell is still a long. The bandgap vanishes and the former optical band can be observed as an uninterrupted continuation of the acoustic branch of the neighboring reciprocal lattice zone. (c) If the two particles are indistinguishable, the unit cell size is effectively $\frac{a}{2}$, the resulting reciprocal zone boundary shifts out to $\frac{2\pi}{a}$ - since there is only one nucleus left in the unit cell, only the acoustic branch remains.

to derive are the terms for the kinetic and the potential energy of the system. The straightforward term for the kinetic energy is

$$T(t) \;=\; \sum_{n,\alpha,k}^{N,r,K} \frac{M_\alpha}{2} \left(\frac{ds_{n,\alpha,k}}{dt} \right)^2 . \tag{3.16}$$

The potential term however is best reached through Taylor expansion up to the third term

$$W(t) \;=\; W_0(\mathbf{R_{n,\alpha}}) \;+\; \sum_{n,\alpha,k} \left(\frac{dW(x)}{ds_{n,\alpha,k}} \right)_{\mathbf{x}=\mathbf{R_{n,\alpha}}} s_{n,\alpha,k} \;+\; \ldots \tag{3.17}$$

$$\ldots \;+\; \frac{1}{2} \sum_{\substack{n,\alpha,k,\\ n',\alpha',k'}} \left(\frac{\partial^2 W(x)}{\partial s_{n,\alpha,k}\, \partial s_{n',\alpha',k'}} \right)_{\mathbf{x}=\mathbf{R_{n,\alpha}}} s_{n,\alpha,k}\; s_{n',\alpha',k'} \;+\; h.o. \tag{3.18}$$

The first term, $W_0(\mathbf{R_{n,\alpha}})$, corresponds to a static, unchanging crystal potential and is thus of no importance in this problem. The second term, $\sum_{n,\alpha,k} \left(\frac{dW(x)}{ds_{n,\alpha,k}} \right)_{\mathbf{x}=\mathbf{R_{n,\alpha}}}$ represents a force onto the lattice ions in their equilibrium positions, which by definition of the word equilibrium, is also zero. This leaves us with the third term, for which we introduce a

new variable

$$\Phi_{n,\alpha,k}^{n',\alpha',k'} = \frac{1}{2} \sum_{\substack{n,\alpha,k,\\ n',\alpha',k'}} \left(\frac{\partial^2 W(x)}{\partial s_{n,\alpha,k}\, \partial s_{n',\alpha',k'}} \right). \tag{3.19}$$

This matrix contains at each position $(n, \alpha, k, n', \alpha', k')$ the force acting on particle (n, α) in k-direction, when particle (n', α') is moved a unit length in k'-direction. Naturally, this matrix must be symmetric $\Phi_{n,\alpha,k}^{n',\alpha',k'} = \Phi_{n',\alpha',k'}^{n,\alpha,k}$. Assuming this is a conservative system, the equations of motion can be found using $\frac{d}{dt}\left[T(t) + W(t)\right] = 0$. This way, one reaches

$$M_\alpha \ddot{s}_{n,\alpha,k} = - \sum_{\substack{n,\alpha,k,\\ n',\alpha',k'}} \Phi_{n,\alpha,k}^{n',\alpha',k'} s_{n',\alpha',k'}. \tag{3.20}$$

To solve this system of differential equations, a set of assumptions is necessary. At first, we assume periodic solutions

$$s_{n,\alpha,k} = \frac{1}{\sqrt{M_\alpha}} u_{n,\alpha,k} e^{-i\omega t}, \tag{3.21}$$

furthermore, the periodicity of the crystal has so far not been taken into account. The force matrix $\Phi_{n,\alpha,k}^{n',\alpha',k'}$ can easily reflect the translational symmetry of the crystal cells if not the specific numbers n and n', but only their total distance $(n - n')$ enters the equations. Finally, the Ansatz for the translational movement should be of a *Bloch*-type

$$u_{n,\alpha,k} = c_{\alpha,k} e^{i\mathbf{q}\mathbf{R}_n}. \tag{3.22}$$

Considering all these simplifications, the final system of equations that has to be solved is

$$\omega^2 c_{\alpha,k} = \sum_{\alpha',k'} D_{\alpha,k}^{\alpha',k'}(\mathbf{q}) c_{\alpha',k'}, \tag{3.23}$$

with $D_{\alpha,k}^{\alpha',k'}(\mathbf{q})$ being the *dynamic matrix*

$$D_{\alpha,k}^{\alpha',k'}(\mathbf{q}) \equiv \sum_n \frac{\Phi_{\alpha,k}^{\alpha',k'}(n)}{\sqrt{M_\alpha, M_{\alpha'}}} e^{-i\mathbf{q}\mathbf{R}_n}. \tag{3.24}$$

The size of this dynamic matrix is $kr \times kr$ - in the three-dimensional case this gives rise to 3 acoustic and $3(r-1)$ optical phonon modes.

The simplest model to calculate the surface-specific phonon modes of pnictogen (111) surfaces (as described in Section 4) is to model a two-dimensional structure with the same geometry as the top layer of the observed material as seen in figure 3.4. In the model developed for the Bi(111) surface[90] only the interactions between nearest- and next-nearest neighbors have been taken into account. Figure 3.5 depicts a typical solution of

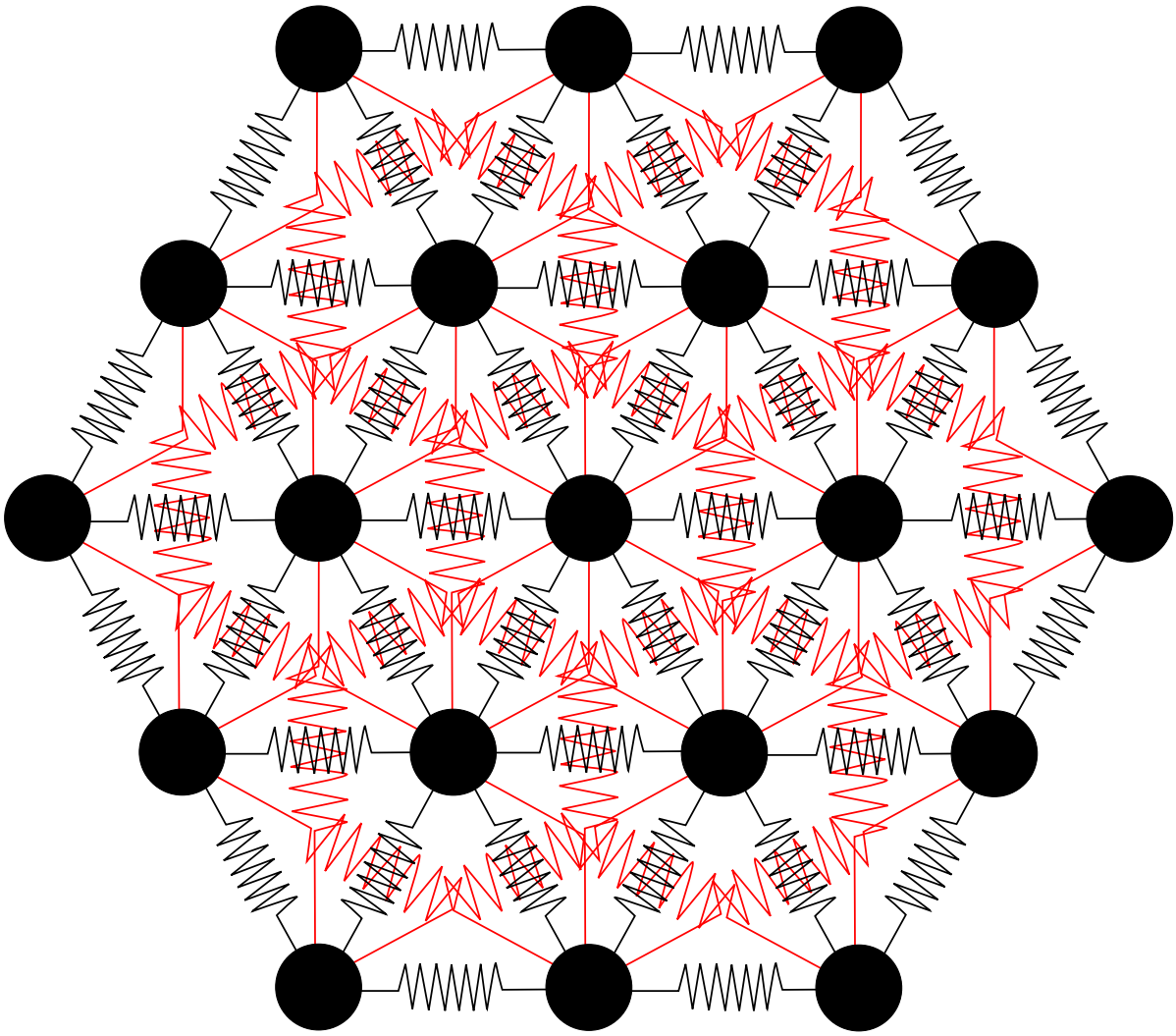

Figure 3.4: Two dimensional spring-model of the hexagonal Bi(111) and Sb(111) surface used for the subsequent phonon calculation. The black and the red springs model different force constants corresponding to nearest- and next-nearest neighbor interaction.

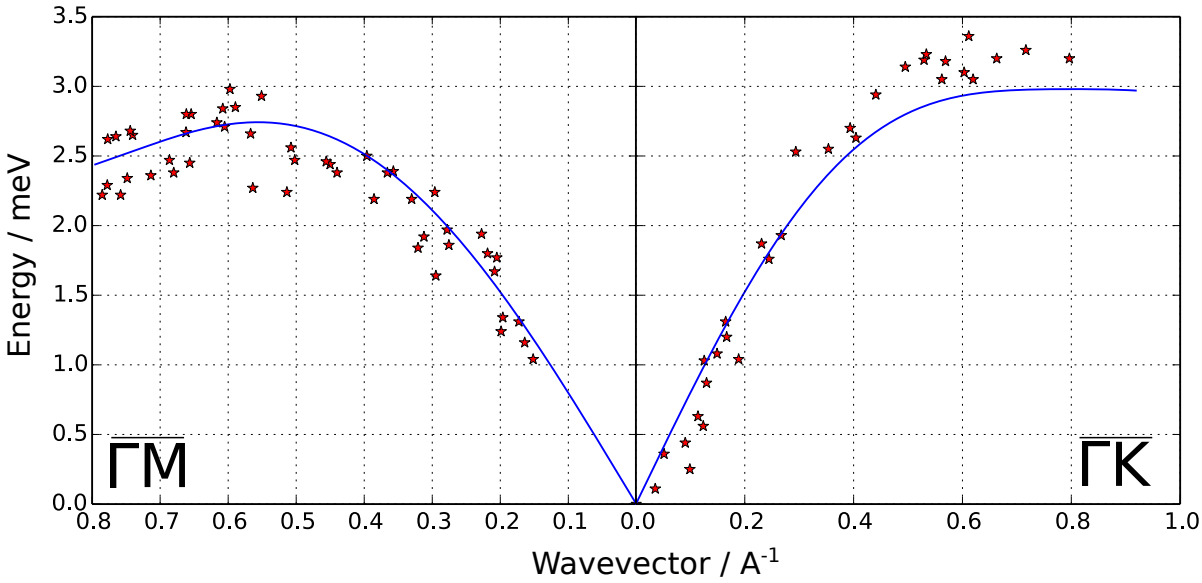

Figure 3.5: Two-dimensional simulation of the acoustic surface phonon dispersion on Bi(111) using the simple force-constant model.[90] The slope of this simulation has been used to confirm the bismuth surface phonon group velocity[91]. The axis in $\overline{\Gamma K}$-direction does not extend to the zone boundary since in this region no measurement points were available.

a two-dimensional force constant model applied to the HAS-TOF measurements on the Bi(111) surface[90,91]. In a simple two-dimensional model there should be two acoustic modes in each high symmetry direction. However, as can be seen in figure 3.4, the two possible in-plane *shear-horizontal* movements of the lattice ions are equivalent due to the mirror-symmetry of the first layer along both high symmetry directions.

3.3.4 Phonon instabilities due to electronic interactions

The simple models introduced up to now assume the forces between the crystal ions to be describable by a simple potential field. In reality those forces are communicated via the lattice electrons. The limited quantum mechanical states for electrons in the crystal as well as their special dynamics may influence the phononic lattice dynamics deeply.

1D-Metals - the Peierls transition

The simplest but most dramatic example of electronic interactions influencing the overall structure and thus the vibrational modes is the Peierls transition (PT). The simplest case of a PT occurs in a one-dimensional chain of atoms with the electronic states filled up to the critical wavevector k_F, ideally situated exactly in the middle between the Γ point and the zone boundary. In this case, a minimal vibrational distortion of the lattice

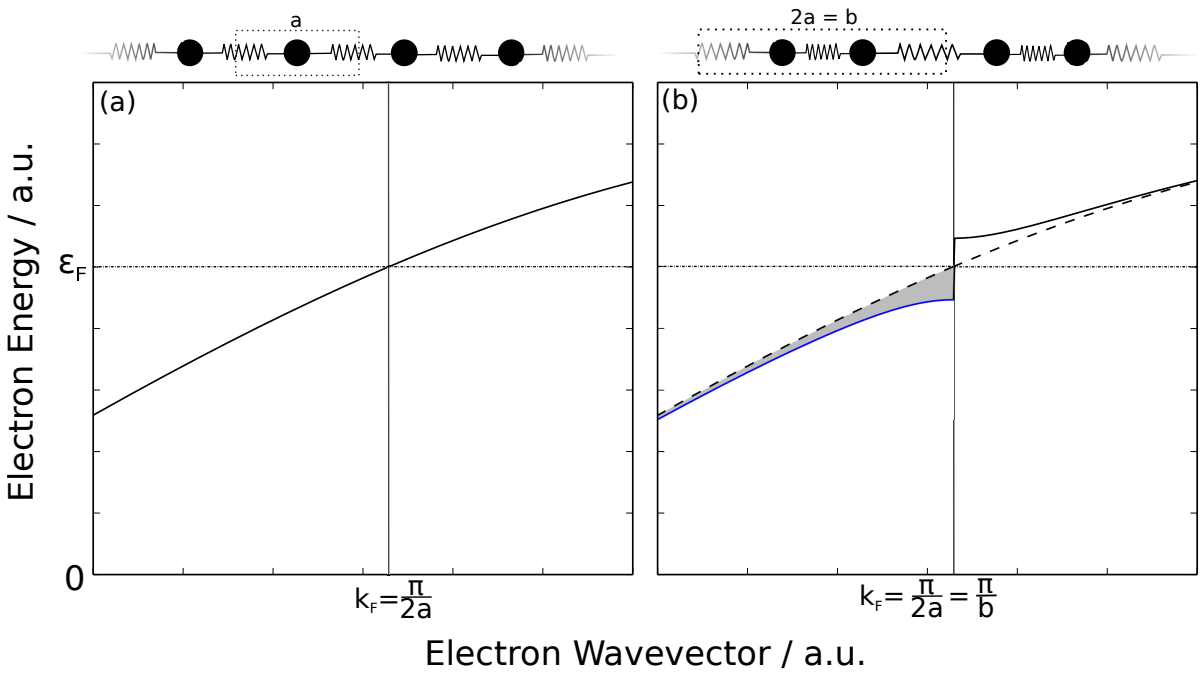

Figure 3.6: Illustration of the effect leading to a Peierls transition. In a one dimensional metal whose electron band is exactly half filled up to the Fermi energy ε_F (a), a periodic distortion leading to a periodicity change to a unit cell twice the size (b) lowers the total energy of the electronic system (filled electron band in blue, the gray area is the energy gained). If this gained energy exceeds the energy needed for the plastic deformation, the distorted state is stable and the material is an insulator.

leads to a different effective lattice constant and therefore an additional band-bending in both the electronic and the phononic dispersion relations. In the described case, a lattice distortion leading to a doubling of the effective lattice constant would result in the opening of an additional gap at k_F, see figure 3.6. The arising electronic band bending lowers the total electronic energy while the final electronic state transits from a conductor to an insulator. If the freed electronic energy is larger than the needed elastic energy for the lattice distortion, this special state is stable and the material will shift to this state at the slightest vibronic excitation.

Kohn anomalies

In 1959, W. Kohn[51] introduced a concept of phonon softening due to interactions with metallic electronic states. In principle, the theory assumes a circular cut through the Fermi surface with radius k_F, however this assumption only helps in simplifying the encountered equations. The basic statement is that as long as the phonon momentum is

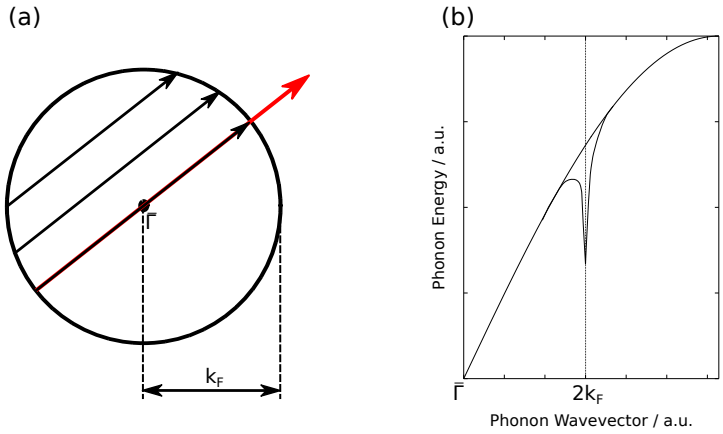

Figure 3.7: Illustration of the effect leading to a Kohn anomaly. (a) Circular cut through the Fermi surface. Phononic movements can be screened by virtual excitations from one side to the other - as long as the respective wavevector does not exceed the diameter of the electron pocket $2k_F$. (b) Consequence of the abrupt loss of screening is a renormalization of the phonon energies to develop a sharp dip in the dispersion.

smaller than $2k_\mathrm{F}$, the phonons are screened by virtual excitations of the electrons along this circular cut. As soon as the phonon momentum exceeds $2k_\mathrm{F}$, the electronic system is no longer able to screen the phononic movement, resulting in an abrupt change of the restoring forces between the lattice ions (see figure 3.7). Note that in this model there is no direct energy transfer between the phonons and the electrons present.

Electron-Hole Excitations

Equivalent to the Kohn anomaly for adiabatic interaction, the phonon-electron interaction may as well be non-adiabatic. In this case, the phonon is destroyed to produce an equivalent electron-hole pair. Due to the striking difference in group velocities in the electron and the phonon dispersions, electronic intra-band transitions with phonon-like momentum by far excel the phonon's supplied energy. Inter-band electronic transitions however may coincide with both momentum and energy of a phonon and produce measurable phonon softening cones. A prominent example for such an effect is observable by HAS on the W(110) and the Mo(110)[45] surface, when a certain amount of hydrogen is chemisorbed. This chemical alteration of the electronic states at the surface enables the electronic transition to be shifted to the appropriate energy/momentum values for a phononic interaction and is present as sharp dips in the recorded phonon dispersion modes.

3.4 Particle-Surface Interaction Potentials

The theoretical core of our measurements is certainly the interaction between the probe particle and the surface under investigation. Interaction potentials do not need to be simple, but in any sensible measurement approach, the interaction should at least be manageable. This chapter not only lists the interaction models used for HAS, but also mentions the other possible interaction phenomena that could arise when scattering different particles.

3.4.1 Attractive particle interaction

Single particles can attract each other by several causes of differing importance in surface science. The basic forces can easily be divided into Coulomb interaction, covalent bonding, dipole interactions (including the hydrogen bond) between intrinsic dipoles and London dispersion forces between induced dipoles. There naturally are several more possibilities for attractive interaction ranging from gravitation to entropic forces. The main objective of this short summary however is to mention the most important attractive interaction procedures for surface interactions measurable in a usual UHV chamber.

Coulomb interaction

Coulomb interaction depicts the electrostatic attraction (or repulsion) between charged ions. Electrostatic interactions are usually large in energy and mainly encountered in ionic crystals as the main bonding characteristic. In most cases, the electronegativity of one particle is much higher than the one of the second particle, as for example in alkali- and halogen interactions, one electron changes place. Both particles benefit from being closer to (if not reaching) a closed electron shell. The resulting electrostatic charge however induces a **strong, non-directional and long-ranged** force on other charged particles known as the *Coulomb interaction*. The total Potential between two charged particles due to Coulomb interaction can be determined by

$$U_E = \frac{1}{4\pi\epsilon_0}\frac{q_1 \cdot q_2}{r} \tag{3.25}$$

with ϵ_0 the electric permittivity of free space, q_i the respective charges and r the distance between the charges.

Covalent bonding

A main principle of molecular bonding relies on the energetic benefits of closed electron shells. While in ionic crystals an electron is completely exchanged, covalent bonding relies on the overlap of electron clouds which can be pictured as two atoms sharing one

electron to each close their respective shells. From these properties, forces involved in covalent bonding can easily be classified as **strong, directional and short-ranged**.

Dipole-Dipole interaction

Similar to ionic interactions, molecules forming a permanent electric dipole may arrange and attract each other depending on their respective dipole moments. The most famous example is water - due to the angular arrangement of the hydrogen at two sides of the oxygen, the total weight of all the negative charges and the positive charges do not occupy the same spot, forming an intrinsic dipole moment. Dipole-dipole interactions may change the behavior of the material significantly - in the case of water the special geometry of this dipole leads to the *anomaly of water*, the lower bulk density of the solid phase compared to the liquid phase. Dipole-dipole interactions are **strong, non-directional and mid-ranged**.

Dispersion forces

Generally known as *London dispersion* forces, two uncharged particles without an intrinsic electric dipole moment may influence each other to attractive interaction. London dispersion forces can be derived by second-order perturbation theory from the Coulomb forces between electrically neutral particles. Virtual excitations of electrons form virtual electric dipoles inducing the formation of electric dipoles due to a charge-carrier shift in the other particle. This procedure of mutual virtual dipole amplification finally leads to a **weak, non-directional and short-ranged** attractive interaction, usually dependent on the size and polarizability of the involved particle and follows a short range potential like

$$U_{LF} \approx -\frac{A}{r^6}. \tag{3.26}$$

3.4.2 Repulsive particle interaction

The most striking repulsive interaction encountered in basic scattering physics is repulsion due to the Pauli exclusion principle. It states that two identical fermions can not be in the same quantum mechanical state at the same time. Hence, when two particles approach each other, the advancing electron orbital overlap would at some point force two electrons into the same state. Before this happens, a very strong repulsive force inhibits the further overlap. The exact shape of the resulting repulsive potential is unknown but the extremely steep behavior is usually modeled by an exponential or a very high arithmetic exponent.

In helium atom scattering, the probe particle is a single atom of the noble gas helium (He). Being a noble gas, its electron orbital is completely filled so the chemical reactivity

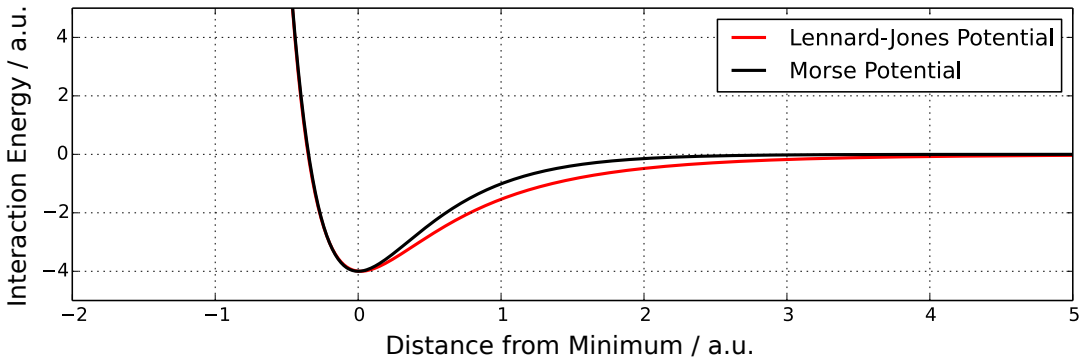

Figure 3.8: Comparative plot of the two most basic interaction shapes. The Lennard-Jones potential has been shifted so the minima coincide. The Lennard-Jones potential describes the attractive interaction shape correctly.

is practically zero. Being a single atom alone, He does not possess an intrinsic dipole moment. Hence, for simple scattering purposes the London dispersion force and the Pauli repulsion will suffice in describing the interaction potential.

3.4.3 Particle-Particle interaction potentials

Naturally, the interaction between two particles contains both modes, the attractive long-range part and the short range repulsive interaction. There are several ways to model and combine the two interactions - the two most common being the Lennard-Jones and the Morse potential.

Lennard-Jones Potentials

The Lennard-Jones potential uses a sum of arithmetic exponents to model the total interaction potential.

$$V_{LJ}(r) \;=\; 4\varepsilon\left[\left(\frac{\sigma}{r}\right)^{12} \;-\; \left(\frac{\sigma}{r}\right)^{6}\right] \tag{3.27}$$

with ε the depth of the potential well and σ the finite distance for which the potential between the particle vanishes. The position of the potential minimum is at $r_m = 2^{1/6}\sigma$. The Lennard-Jones potential is popular for keeping a simple-straightforward form, the attractive London dispersion force behavior is described correctly, while the repulsive r^{-12} term is steep enough to account for a realistic Pauli repulsion. The Lennard-Jones potential is depicted as the red line in figure 3.8.

Morse Potentials

The 1D Morse interaction potential is formed by a sum of suitable exponential functions.

$$V_{M-1D}(r) \;=\; \varepsilon\left(e^{-2\kappa r} - 2e^{-\kappa r}\right) \tag{3.28}$$

The choice of exponentials makes the Morse potential convenient for theoretical usage since simple derivatives or integrals may be calculated analytically and entered into the simulations again as simple functions of the potential itself. Furthermore the exponentials are quite advantageous when dealing with surface periodicities as can be seen in the Appendix section of Chapter 7. The exponential treatment of the repulsive part describes the sudden Pauli repulsion very well while the only but major downside is the description of the attractive interaction. The attractive exponential decays comparatively fast and is not perfectly suited to describe long-range attractive interaction such as in the London dispersion forces. The Morse potential is depicted as the black line in figure 3.8.

Hard Wall Model

Completely ignoring the attractive interaction or the finite ascension of the repulsive slope, the *Hard Wall Model* assumes the potential to be zero at all distances larger than the classical turning point, at which it instantaneously jumps to infinity. While completely suitable for high-energy collisions, this assumed potential shape naturally neglects all effects originating from the potential well. Nevertheless, the *Hard Wall Model* is commonly used in 3D surface potentials (*Hard Corrugated Wall Model*, HCW) for obtaining the surface corrugation height from approximative methods[26,28,41].

Potential Well Model

The *Potential Well Model* adopts the basic ideas from the *Hard Wall Model*, the potential jumps to infinity at the classical turning point and the potential is zero most of the rest of the distance. Shortly before the repulsive jump, however, the *Potential Well Model* assumes a rectangular potential well. The *Potential Well Model* is used when the exact shape of the potential is not of interest, while effects from the attractive interaction should still be considered. A common example is the inclusion of the *Beeby Correction* (see 3.9.6) in elastic scattering analysis.

3.4.4 Particle-Surface interaction potentials

The potential supplied by a surface is generally more complex than the potential of a single particle. For a complete understanding of the interaction process, the complete three dimensional architecture of the potential would be needed. For the basic analysis

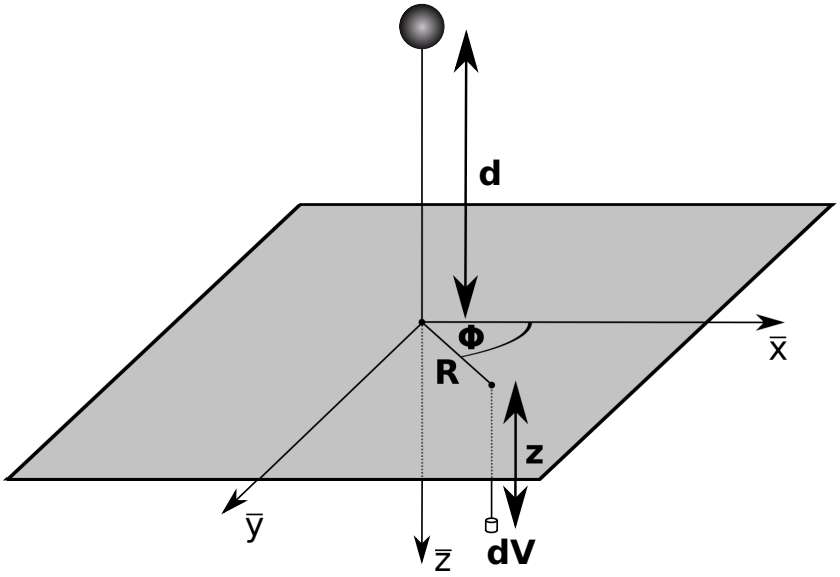

Figure 3.9: Schematic representation of the integrated structure to derive the 9-3 potential from the Lennard-Jones potential.

of scattering processes including elastic interaction and thus resonant effects (see 3.8), the surfaced-averaged interaction potential, only dependent on the total particle-surface distance, is needed. More complex analysis tools such as the Close-Coupling approach (see 3.9.4) require a full description of the interaction.

The 9-3 Potential

The most straightforward way to describe the surface averaged interaction between a probe particle and a surface is to just assume a particle-particle interaction potential and consider this interaction for each lattice atom of the whole crystal. The summation over each lattice site is in general too complicated and substituted by an integration over a homogeneous crystal-mass. If for example the Lennard-Jones potential is considered (see 3.4.3, figure 3.8), the final interaction potential can be calculated as follows[84]

$$V(d) \;=\; 4\varepsilon \int_0^{2\pi}\int_0^{\infty}\int_0^{\infty} R \cdot dR\; d\phi\; dz \left[\frac{\sigma^{12}}{(R^2+(d+z)^2)^6} \;-\; \frac{\sigma^{6}}{(R^2+(d+z)^2)^3}\right] \qquad (3.29)$$

using cylindrical coordinates with the particle at a height d above the surface along the polar axis. The depth of the volume element below the surface is depicted by z (see

figure 3.9).

$$V(d) \;=\; 8\pi\varepsilon \int_0^\infty\!\!\int_0^\infty dR\; dz \;\left[\frac{R\cdot\sigma^{12}}{(R^2+(d+z)^2)^6} \;-\; \frac{R\cdot\sigma^{6}}{(R^2+(d+z)^2)^3}\right] \tag{3.30}$$

after integration over R,

$$V(d) \;=\; 8\pi\varepsilon \int_0^\infty dz \left[-\frac{\sigma^{12}}{10\cdot(R^2+(d+z)^2)^5} \;+\; \frac{\sigma^{6}}{4\cdot(R^2+(d+z)^2)^2}\right]_0^\infty \tag{3.31}$$

$$V(d) \;=\; 8\pi\varepsilon \int_0^\infty dz \left[\frac{\sigma^{12}}{10\cdot(d+z)^{10}} \;-\; \frac{\sigma^{6}}{4\cdot(d+z)^4}\right] \tag{3.32}$$

By now, the integral over the surface layer is complete. The integrand in equation 3.32 thus also represents the correct surface averaged interaction potential for a two-dimensional material as graphene or silicene. Performing the last integral,

$$V(d) \;=\; 8\pi\varepsilon \left[-\frac{\sigma^{12}}{90\cdot(d+z)^9} \;+\; \frac{\sigma^{6}}{12\cdot(d+z)^3}\right]_0^\infty \tag{3.33}$$

$$V(d) \;=\; 8\pi\varepsilon\sigma^3 \left[\frac{1}{90}\left(\frac{\sigma}{d}\right)^9 \;-\; \frac{1}{12}\left(\frac{\sigma}{d}\right)^3\right], \tag{3.34}$$

or, after simplification

$$V_{9-3}(d) \;=\; \frac{2}{3}\pi\varepsilon\sigma^3 \left[\frac{2}{15}\left(\frac{\sigma}{d}\right)^9 \;-\; \left(\frac{\sigma}{d}\right)^3\right]. \tag{3.35}$$

Equation 3.35 now models the steep repulsive slope quite well while reproducing the expected attractive behavior of the surface London dispersion forces.

Corrugated Morse Potential

If three dimensional potential architectures are needed, a commonly used specimen is the *Corrugated Morse Potential*

$$V_{CMP}(\mathbf{R},z) \;=\; D\left[\frac{1}{\nu_0}e^{-2\kappa[z-\xi(\mathbf{R})]} - 2e^{-\kappa z}\right], \tag{3.36}$$

with $\xi(\mathbf{R})$ the corrugation function and ν_0 the surface average of the exponential of the corrugation function

$$\nu_0 \;=\; \frac{1}{\Sigma}\int_\Sigma e^{2\kappa\xi(\mathbf{R})}d\mathbf{R}. \tag{3.37}$$

The two-dimensional periodicity of the corrugation function contains the periodicity of the crystal under investigation as well as the general structure of the height distribution in a surface unit cell. The *Corrugated Morse Potential* is a popular choice because the exponentials involved account for easy differentiability - for a lot of important numerical cases sub-problems can be solved analytically (see Appendix of Chapter 7). The second advantage is that the surface averaged interaction potential of the *Corrugated Morse Potential* reduces to the standard Morse interaction potential, equation 3.28.

3.5 Helium Atom Scattering

Molecular scattering techniques, as for example helium, hydrogen or deuterium scattering methods complement the spectrum of conventional scattering methods. While Neutron scattering more or less uninhibitedly penetrates the bulk - and electron as well as X-ray scattering data always include at least a small amount of bulk contributions, molecular scattering adds the possibility to probe solely surface specific properties. Diatomic molecule scattering provides an additional channel for gathering information about surface dynamics in analyzing the change in rotation/vibration of the molecule. Since this technique is however not applied in the local machine, these methods are not described in this work. Monoatomic species, namely the noble gas atoms provide the advantageous peculiarity of being practically non-reactive, thus combined with the small particle energies given in atomic scattering ($10 - 200$ meV) the method can be thought of as completely nondestructive to the surface or surface structures. Due to the comparatively high mass of atoms or molecules their de Broglie wavelength is short enough for crystallographic analysis even at low incident energies. Helium, being the lightest noble gas is usually chosen in all applications where next to the structural properties of the surface the vibronic properties are of interest. Due to the lower mass, helium atoms have a larger cross section for single-phonon interactions - giving rise to clearly resolved phonon energies in simple time-of-flight (TOF) measurements. The following chapters give a short overview of the basic measurement techniques and the effects observed.

3.6 Surface Structure Analysis from Elastic HAS

As previously explained in Section 3.2.1, waves or particles with an appropriate wavelength can be elastically diffracted from periodically structured surfaces. In addition to the definite change in parallel momentum (equation 3.6) and the conservation of particle energy (equation 3.7) in elastic diffraction, the fixed-angle geometry of the machine adds more restrictions to the measurability of elastic diffraction peaks. The total angle θ_{SD} enclosed by the source- and the detection arm is fixed, thus for every measured particle the scattering process from $\mathbf{k}_i$ to $\mathbf{k}_f$, depicting incident- and final wavevector, must fulfill

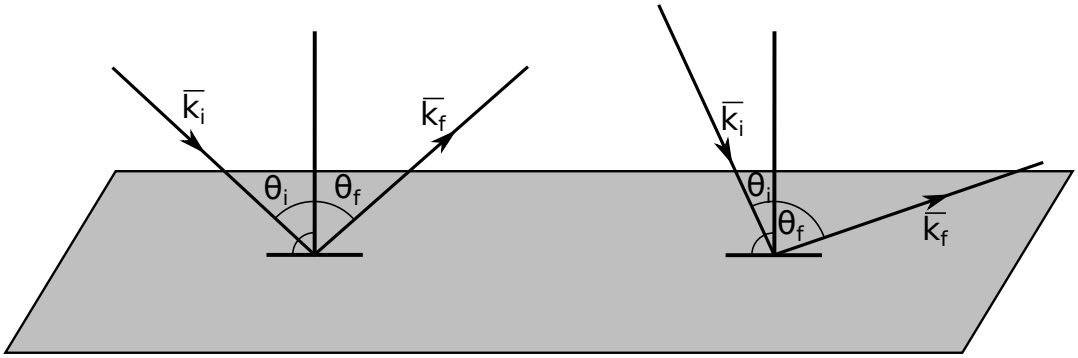

Figure 3.10: Illustration of the mutual dependence of θ_i and θ_f in a constant-angle scattering apparatus. If the angle of incidence is changed, the measurable outgoing angle is changed also, the total sum of both angles must be $\theta_i + \theta_f = \theta_{SD}$

the fixed-angle-condition

$$\theta_{SD} \;=\; \theta_i + \theta_f, \tag{3.38}$$

with θ_i and θ_f being the incident- and final scattering angle, measured from the surface normal (see figure 3.10). Due to this geometry, the wavevectors' respective components parallel to the surface can be easily calculated by

$$\begin{aligned} |\mathbf{K}_i| &= |\mathbf{k}_i| \cdot sin(\theta_i) \\ |\mathbf{K}_f| &= |\mathbf{k}_f| \cdot sin(\theta_f). \end{aligned} \tag{3.39}$$

Using equations 3.38 and 3.39 with equations 3.6 and 3.7, the scattering condition in fixed angle machines can be deduced:

$$\theta_i \;=\; \frac{\theta_{SD}}{2} \;-\; \arcsin\left[\frac{|\mathbf{G}_{h,k}|}{2|\mathbf{k}_i| cos(\frac{\theta_{SD}}{2})}\right] \tag{3.40}$$

Hence, the reciprocal lattice vector of the nearest in-plane reciprocal lattice point can be calculated from the measured diffraction angle if the incident temperature-dependent wavevector of the probe particle is known. Measuring the reciprocal lattice vectors of the high-symmetry directions as well as the respective polar angle in between them, the reciprocal lattice structure of the surface and thus the real space structure can be determined.

3.7 Surface Phonon Analysis from Inelastic HAS

In inelastic scattering processes, the probe particle, in addition to the surface diffraction, undergoes an additional interaction such as the interaction with a quasiparticle like i.e.

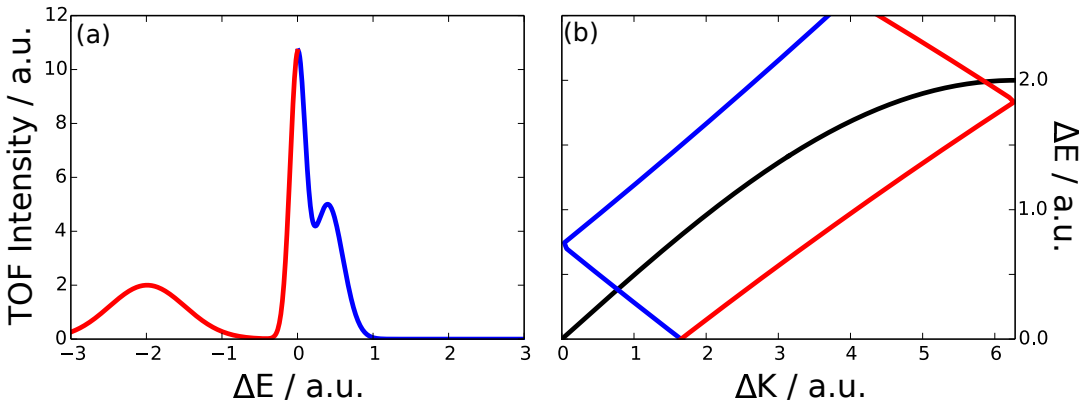

Figure 3.11: Explanatory set of TOF measurement with the corresponding scancurve. (a) Idealized simulation of a TOF measurement. Phonon creation and annihilation side are specified by red and blue color respectively. Besides the diffuse elastic peak at $\Delta E = 0$ two phonon interaction peaks are observed. (b) Corresponding scancurve of the idealized measurement depicted in (a). The complete scancurve was backfolded into the first positive-energy relevant region of the reciprocal space. Phonon creation and annihilation sides are labeled using red and blue color. The two peaks observable in (a) correspond to the two cuts of the scancurve with the underlying acoustic phonon mode in (b).

phonons or plasmons. As this quasiparticle usually carries momentum as well as energy, the scattering conditions are altered to

$$\begin{aligned} E_f &= E_i \pm \hbar\omega \\ \mathbf{K}_f &= \mathbf{K}_i \pm \mathbf{Q}(\omega). \end{aligned} \tag{3.41}$$

Using these additional scattering requirements in combination with the fixed-angle geometry, a special dependence of the interaction energy and the exchanged momentum is obtained:

$$\frac{\Delta E}{E_i} + 1 = \frac{\sin^2(\theta_i)}{\sin^2(\theta_{SD} - \theta_i)} \left(1 + \frac{\Delta K}{K_i}\right)^2 \tag{3.42}$$

The curve defined by equation 3.42 is called scancurve. Interpretation of the TOF signal using this scancurve is depicted in figure 3.11. If at a certain incident angle θ_i a particle is detected with a certain runtime difference from the specular contribution corresponding to an energy difference ΔE, the related momentum of the interacting quasiparticle is given by ΔK. The local machine measures the time-delay between the specular contribution and the inelastically scattered helium atom. The transformation

to an energy spectrum is straightforward

$$E_f = \frac{m}{2}\left(\frac{L}{t}\right)^2, \tag{3.43}$$

with L the traveled distance and t the measured time. Since the He atoms travel some distance from the chopper disc to the sample before the interaction and the energy exchange occurs, the corresponding formula is somewhat more complicated and has been featured in earlier literature[88]. The resulting signal is transfered to the energy scale but must still be rescaled due to the non-linearity of the energy scale

$$\left|\frac{\mathrm{d}t}{\mathrm{d}\Delta E}\right| = \frac{t^3}{m \cdot L}. \tag{3.44}$$

Due to this transformation, the particles taking very long to reach the detector (the particles which created quasiparticles on the surface) are weighted significantly larger and produce an extreme rise in intensity of the energy spectrum in the region where the energy of the detected particle approaches zero. Since this rescaling affects all the intensity measured in the TOF, significant care has to be taken to minimize the stochastic background noise. Its amplification renders the analysis of low-energy signals in the TOF impossible. A further important improvement on the TOF-data analysis can be made by introducing a variable binning method first suggested by Bracco[14]. For this purpose the signal is not averaged with a simple moving frame as usual, but the width of this frame is gradually widened as it approaches the $\Delta E = 0$ side. In the case of the present measurements the width was calculated so that the calculated averages are at equidistant energetic positions.

3.8 Resonant Behavior in HAS Measurements

Well resolved angular spectra bear a multitude of additional useful information if the origin of some of the involved effects is known. Figure 3.12 is a magnified version of an angular spectrum on Sb(111). Clearly, between the observed diffraction peaks additional features appear. These variations in the background intensity can usually be assigned to *Selective Adsorption Resonances* or *Kinematical Focussing* effects.

3.8.1 Selective Adsorption Resonances

Any realistic model of an attractive interaction between the surface and a probe atom will result in the appearance of possible eigenstates of the interaction potential. Atoms trapped in these *bound states* will stay at the surface, vibrating inside the interaction potential. While the direct scattering into a *bound state* is unlikely but still possible, usual HAS measurements are not able to identify a signal related to this phenomenon. The

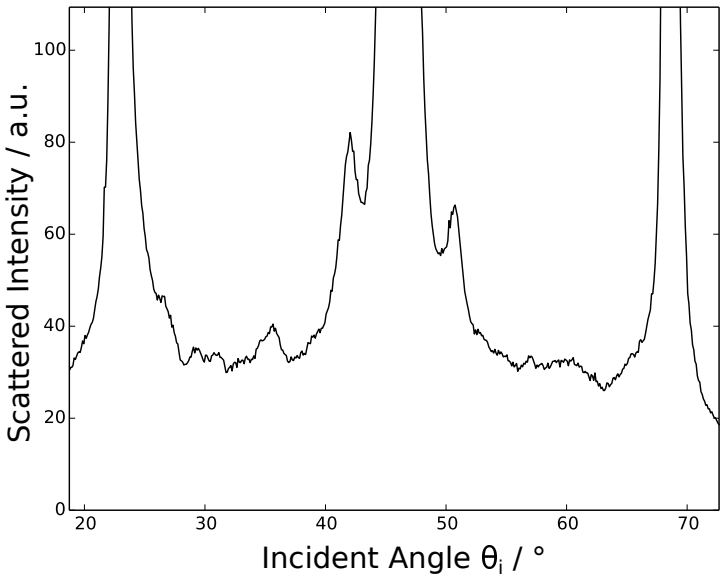

Figure 3.12: Magnified angular spectrum of Sb(111)-$\overline{\Gamma\mathrm{M}}$. In between the elastic scattering positions, small variations in the background intensity can be identified as resonant or kinematical effects.

usual effect of these *bound states* is the appearance of *Selective Adsorption Resonances* (SAR). The elementary mechanics are simple, due to the existence of *bound states* in the z-dependent surface averaged interaction potential, the scattered helium atom can leave the scattering process either inside the continuous spectrum $E_z \approx \mathbf{k}_z^2 > 0$, or inside one of the finite bound states $E_z \approx \mathbf{k}_z^2 < 0$. During the scattering process, energy and momentum must be conserved. With the possibility of negative, bound values in z-direction, the equation for energy conservation is altered to

$$\mathbf{k}_i^2 \;=\; (\mathbf{K}_i + \mathbf{G}_\parallel)^2 \;+\; \mathbf{G}_\perp^2 \;-\; \frac{2m}{\hbar^2}|\varepsilon_n|, \tag{3.45}$$

with $\mathbf{G}_\parallel$ and $\mathbf{G}_\perp$ being the components of the interacting reciprocal lattice vector parallel and perpendicular to the incident scattering direction respectively and $|\varepsilon_n|$ are the absolute values of the *bound state* energy. Thus, the helium atom enters a *bound state* by increasing its surface-parallel energy by diffraction up to the point where its surface perpendicular energy coincides with a *bound state* energy. Naturally, the He atom can leave the surface by the reverse process. From the viewpoint of the observer outside a directly scattered atom and an atom scattered through a transient *bound state* are indistinguishable, differing only in their quantum-mechanical phase. This phase-difference leads to an enhancement or a depression of the observed signal.
The explained process however would only lead to variations in the diffraction heights, since only purely elastic effects were taken into consideration. The signal in between the diffraction peaks in figure 3.12 however must have interacted with some quasiparticle or

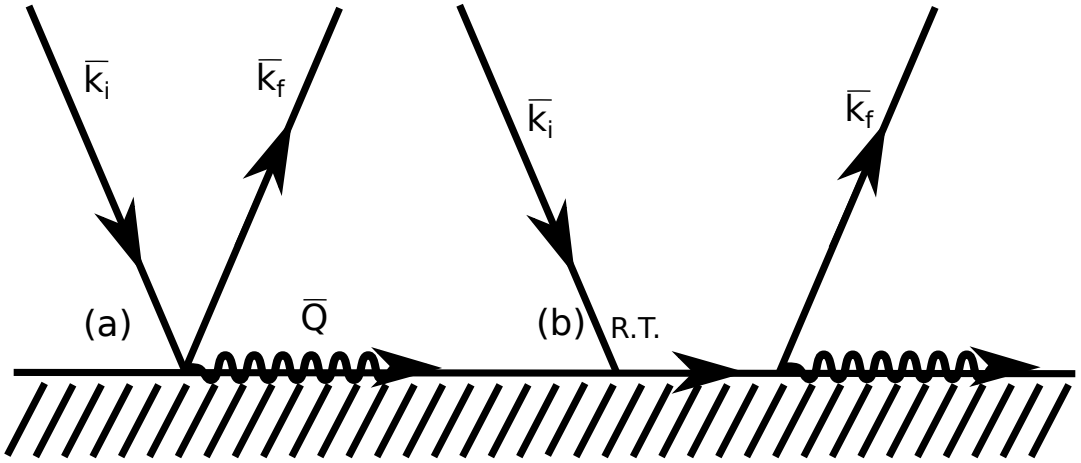

Figure 3.13: Schematic representation of the inelastic and the resonant inelastic scattering process. (a) Standard inelastic scattering. The transition from $\mathbf{k}_i$ to $\mathbf{k}_f$ produces an additional surface phonon $\mathbf{Q}$. (b) The incident conditions allow the scattering particle to undergo a resonant transition (R.T.) into the bound state. After some traveling time, the particle can scatter out of the bound state. In certain cases, the resulting outgoing state is indistinguishable from the standard inelastic scattered particle.

a surface impurity to arrive at its position. To account for inelastic resonant entry or exit, the equation for energy conservation can be adapted again,

$$\mathbf{k}_i^2 \;=\; (\mathbf{K}_i + \mathbf{G}_{\parallel} \;+\; \mathbf{Q}_{\parallel})^2 \;+\; \mathbf{G}_{\perp}^2 \;+\; \mathbf{Q}_{\perp}^2 \;\pm\; E(\mathbf{Q}) \;-\; \frac{2m}{\hbar^2}|\varepsilon_n|, \tag{3.46}$$

with $\mathbf{Q}_{\parallel}$ and $\mathbf{Q}_{\perp}$ the parallel and perpendicular projections of the interacting phonon momentum onto the incident scattering direction and $E(\mathbf{Q})$ the corresponding phonon energy. As any reader might imagine, the prediction of inelastic entry positions is complicated and requires detailed knowledge of not only the surface structure but also the inelastic crystal properties. However, if an elastic entry into the bound state is assumed, an inelastic exit could account for the position in between the diffraction peaks and the process would still be indistinguishable from a standard inelastic scattering process, as is depicted in figure 3.13. The elastic entry, as can be derived from equation 3.45, only depends on the total beam momentum $\mathbf{k}_i$ and its projection onto the surface $\mathbf{K}_i$ as experimental parameters. Due to the knowledge of the angle the resonance occurs at, as well as the beam momentum from the nozzle temperature, the finite possibilities of reciprocal lattice vectors enable the determination of the *bound state* energies of the surface averaged interaction potential.

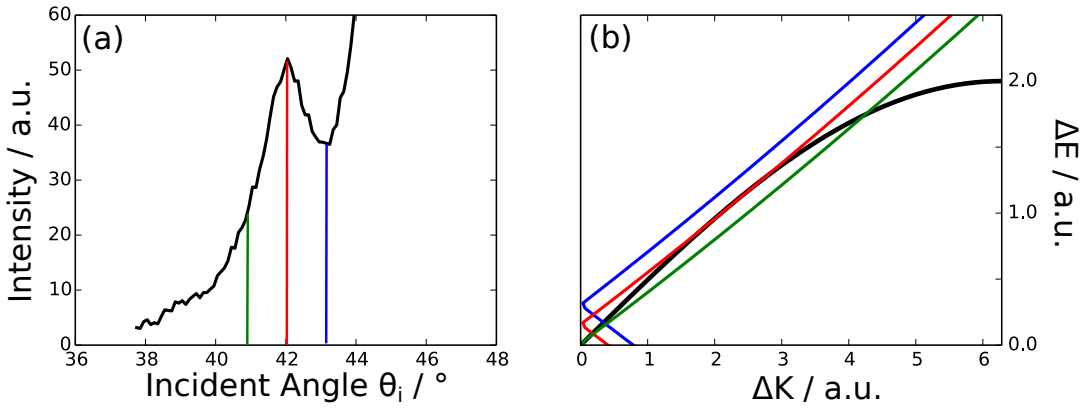

Figure 3.14: The Kinematical Focussing effect and its origins. (b) The scancurve shifts its position dependent on the angle of incidence of the incoming particles. Approaching the tangency condition, the energetic overlap between the phonon branch and the scancurve rises gradually, resulting in a gradual enhancement of the background signal in (a). At the tangency position, the intensity peaks and drops abruptly afterwards. (a) Magnified section of the angular spectrum also shown in 3.12. The selected peak can be identified to be of KF origin.

3.8.2 Kinematical Focussing

Significant features in between diffraction peaks may also originate from *Kinematical Focusing* (KF) effects. KF effects occur, when the slope of the scan curve (equation 3.42) is tangent to a phonon mode, producing a *van Hove singularity* in the atomic reflectivity[7,61]. The feature shape is very distinct in rising gradually to a maximum and dropping instantaneously afterwards, producing a wedge-like shape. The shape can be explained by probing increasingly more phonons as the scancurve approaches the tangency condition and losing interactability directly afterwards (see figure 3.14).

In machines where time-resolved measurements are hard to perform, the KF effect can be utilized to track down the position of the phonon dispersion from the angular spectra[9,66]. In order to do this, the machine should however be able to change incident- and final scattering angle independently to account for more adjustable KF positions.

3.9 Methods of Describing the Helium-Surface Interaction

Deducing the exact three-dimensional He-surface interaction potential from measurements is, as can be expected from an experiment probing so many different surface specific effects, a complicated business. In order to explain the measured effects, sev-

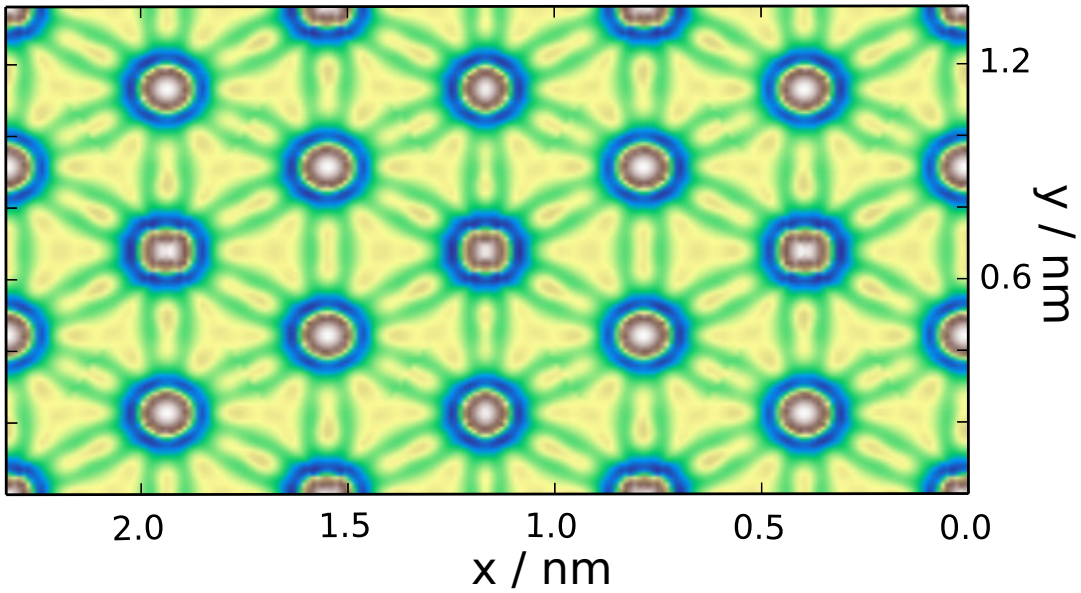

Figure 3.15: Calculated Bi(111) corrugation using the iterative formula derived from the Rayleigh approximation. The caps on the atom positions are given a finite value since the method diverges at their positions. A valid calculation of the peak-to-peak corrugation height is thus not possible using this method.

eral models have been developed. These models can be used to determine surface- and surface-interaction specific properties from the measurements.

3.9.1 Rayleigh Approximation

In the *Rayleigh Approximation*, the total wavefunction of the interacting particle beam is described as a set of plane waves for the incoming- as well as for the outgoing waves.

$$\Psi(\mathbf{R}, z) \;=\; \exp\left(\mathrm{i}[\mathbf{K}\cdot\mathbf{R} \;+\; \mathbf{k}_{iz}z]\right) \;+\; \sum_{\mathbf{G}} A_G \exp\left(\mathrm{i}[(\mathbf{K} \;+\; \mathbf{G})\cdot\mathbf{R} \;+\; k_{Gz}z]\right) \tag{3.47}$$

The helium-surface interaction in this case is assumed to be of a hard-corrugated-wall character, and the corrugation at all places where $\mathbf{G}\cdot\mathbf{R}$ is small, can be derived using a recursive formula

$$\begin{aligned}\xi^n(\mathbf{R}) \;=\; & \frac{1}{|\mathbf{k}_i|\cos\theta_i}\cdot\arccos\left[-\frac{1}{\sqrt{P_0}+1}\sum_{\mathbf{G}'}\sqrt{P_{\mathbf{G}'}\frac{\cos\theta_i}{\cos(\theta_{SD}-\theta_i)}}\cdots\right. \\ & \left.\cdots\cos(\mathbf{G}'\cdot\mathbf{R}+|\mathbf{k}_i|\cdot\cos(\theta_{SD}-\theta_i)\cdot\xi^{n-1}(\mathbf{R}))\right],\end{aligned} \tag{3.48}$$

with the $P_{\mathbf{G}}$ being the measured scattering intensities from the reciprocal lattice vector $\mathbf{G}'$. A derivation of this recursion formula is given in[52]. This recursive equation can be quite useful if the corrugation far away from the lattice sites is of special interest. At the

lattice site position, the resulting corrugation intensity diverges. Usually, the lattice sites are capped by a finite value so the structure in between can still be seen. The structure of Bi(111) was derived using this method and the result is depicted in figure 3.15. As can be seen, the lattice periodicity reproduces nicely by the capped (brown-white) peaks. In between those peaks the measurements, however, lead to elevated channels in between the lattice sites, possibly following a covalent-like surface bond[52]. Due to the divergence at the lattice sites, this method can not be used to derive valid peak-to-peak corrugation values.

3.9.2 GR Method

To obtain valid results from the Rayleigh approximation N. García[31,32] proposed to multiply equation 3.47 with $\exp(\mathrm{i}k_{iz} \cdot \xi(\mathbf{R}))$ to arrive at the matrix equation

$$\sum_{\mathbf{G}} \mathbf{A_G} \mathbf{M_{GR}} \;=\; -1, \tag{3.49}$$

with

$$\mathbf{M_{GR}} \;=\; \mathrm{e}^{\mathrm{i}[(k_{\mathbf{G}z} - k_{iz})\xi(\mathbf{R}) + \mathbf{G}\cdot\mathbf{R}]}. \tag{3.50}$$

For an equal number of $\mathbf{G}$ and $\mathbf{R}$ values the linear system of equations possesses a unique solution $\mathbf{A_G}$, as long as $|\mathbf{M_{GR}}| \neq 0$. This is usually achieved through choosing only $\mathbf{R}$ values within the first unit cell[31]. The vector $\mathbf{A_G}$ is related to the measured intensities $\mathbf{P_G}$ via

$$\mathbf{P_G} \;=\; \frac{|\mathbf{k}_{\mathbf{G}z}|}{|\mathbf{k}_{iz}|} \mathbf{A_G} \mathbf{A^*_G}. \tag{3.51}$$

The GR-method provides convergent solutions if the relative corrugation $\beta_0 = \frac{\xi_{p-p}}{a}$ stays below 18%[28].

3.9.3 Eikonal Approximation

Another method for using the Rayleigh approximation is achieved by multiplying equation 3.47 on both sides with $\exp(-\mathrm{i}[\mathbf{G'} \cdot \mathbf{R} \;+\; k_{\mathbf{G'}z} \cdot \xi(\mathbf{R})])$ and integrating over the unit cell (uc)

$$\begin{aligned}
\sum_{\mathbf{G}} \mathbf{M_{GG'}} &= \mathbf{A^0_{G'}} \\
\mathbf{M_{GG'}} &= \frac{1}{S} \int_{\mathrm{uc}} \mathrm{e}^{\mathrm{i}[(\mathbf{G}-\mathbf{G'})\mathbf{R} + (k_{\mathbf{G'}z} - k_{iz})\xi(\mathbf{R})]} d\mathbf{R} \\
\mathbf{A^0_{G'}} &= -\frac{1}{S} \int_{\mathrm{uc}} \mathrm{e}^{-\mathrm{i}[\mathbf{G'R} + (k_{\mathbf{G'}z} - k_{iz})\xi(\mathbf{R})]} d\mathbf{R}
\end{aligned} \tag{3.52}$$

If the relative corrugation $\beta_0 < 10\%$, the off-diagonal elements of $\mathbf{M_{GG'}}$ can be neglected and only the Integral for $\mathbf{A^0_{G'}}$ needs to be evaluated. For certain geometries this can even be achieved analytically.

3.9.4 Close-Coupling

Unlike the previously described interaction simulation methods, the Close-Coupling (CC) relies on a three-dimensional soft corrugated potential to calculate the scattered intensities. In contrast to the hard corrugated wall model the realistic interaction potential includes an attractive part giving rise to bound states of the helium-surface interaction potential. As described in section 3.8 these bound states can lead to sudden unexpected and dramatic changes in the measured intensity and must be included in any realistic description of scattering experiments. Out of simplicity, all equations in this chapter assume $\hbar^2/2m = 1$.
Starting with the time-independent Schrödinger equation,

$$\left[-\nabla^2 \; + \; V(\mathbf{r}) \; - \; \mathbf{k}_i^2\right] \Psi(\mathbf{r}) \; = \; 0, \tag{3.53}$$

the wavefunction can be Fourier expanded in terms of reciprocal lattice vectors

$$\Psi(\mathbf{r}) \; = \; \sum_{\mathbf{G}} \Psi_{\mathbf{G}}(z) \mathrm{e}^{\mathrm{i}(\mathbf{K}_i + \mathbf{G})\cdot\mathbf{R}} \tag{3.54}$$

as well as the total interaction potential

$$V(\mathbf{r}) \; = \; \sum_{\mathbf{G}} V_{\mathbf{G}}(z) \mathrm{e}^{\mathrm{i}\mathbf{G}\cdot\mathbf{R}}, \tag{3.55}$$

with the expansion terms

$$V_{\mathbf{G}}(z) \; = \; \frac{1}{S} \int_{\mathrm{uc}} V(\mathbf{r}) \mathrm{e}^{-\mathrm{i}\mathbf{G}\cdot\mathbf{R}}, \tag{3.56}$$

where S represents the surface area of the unit cell. A common choice for the three dimensional interaction potential between the impinging helium atom and the surface is the *Corrugated Morse Potential* (CMP), equation 3.36. Due to its simple exponential structure a lot of calculations can be done analytically and the calculational effort can be reduced. The expansion terms $V_{\mathbf{G}}(z)$ can be written as

$$V_{\mathbf{G}}(z) \; = \; D \frac{\mathcal{V}_{\mathbf{G}}}{\mathcal{V}_{\mathbf{0}}} \mathrm{e}^{-2\chi z} \tag{3.57}$$

with $\mathcal{V}_{\mathbf{G}}$ the so-called *coupling factors*, which can be calculated by

$$\mathcal{V}_{\mathbf{G}} \; = \; \frac{1}{S} \int_{uc} \mathrm{e}^{-\mathrm{i}\mathbf{G}\cdot\mathrm{R}} \mathrm{e}^{2\chi\xi(\mathbf{R})} d\mathbf{R}. \tag{3.58}$$

Especially this simple relationship makes the CMP an attractive candidate for close-coupling simulations. While the real coupling integral equation 3.58 is independent of z, the simple z-dependence of equation 3.57 allows the calculation of the real relevant Fourier terms to be done economically by multiplying the constant coupling factors only by an exponential. Furthermore, for most structures equation 3.58 can be evaluated analytically, as was shown in several publications[53,74] - the paper on Sb(111) being presented in Chapter 7 for the hexagonal structure of the pnictogen-(111) surfaces.
Aside from the CMP, the Fourier transformed potential and the wavefunction equation 3.54 and 3.55 are inserted into the Schrödinger equation which is multiplied on both sides by $\exp(-\mathrm{i}(\mathbf{K}_i + \mathbf{G}) \cdot \mathbf{R})$ and integrated over the unit cell area to arrive at the set of coupled equations

$$\left[\frac{\mathrm{d}^2}{\mathrm{d}z^2} + \mathbf{k}^2_{\mathbf{G},z} - V_{\mathbf{0}}(z)\right] \Psi_{\mathbf{G}}(z) \;=\; \sum_{\mathbf{G}' \neq \mathbf{G}} V_{\mathbf{G}-\mathbf{G}'}(z) \Psi_{\mathbf{G}'}(z) \tag{3.59}$$

for the perpendicular waves with $\mathbf{k}^2_{\mathbf{G},z}$ the z-component of the particle's kinetic energy after surface interaction

$$\mathbf{k}^2_{\mathbf{G},z} \;=\; \mathbf{k}^2_i - (\mathbf{K}_i + \mathbf{G})^2 \tag{3.60}$$

and $V_{\mathbf{0}}(z)$ the surface-averaged particle-surface interaction potential. Interpretation of equation 3.59 can be quite tricky but can be simplified by revoking the very last step of the conversion to arrive at

$$\mathbf{k}^2_{\mathbf{G},z} \Psi_{\mathbf{G}}(z) \;=\; -\frac{\mathrm{d}^2}{\mathrm{d}z^2} \Psi_{\mathbf{G}}(z) + \sum_{\mathbf{G}'} V_{\mathbf{G}-\mathbf{G}'}(z) \Psi_{\mathbf{G}'}(z). \tag{3.61}$$

Equation 3.61 clearly shows that the Schrödinger equation for each involved wavefunction $\Psi_{\mathbf{G}}(z)$ includes a potential term dependent on all other wavefunction intensities and their respective Fourier terms (*couplings*) at this z-position. This way, if all the intensity of the system is initially in one term (as can be assumed for the incident beam), the respective size of the Fourier terms $V_{\mathbf{G}-\mathbf{G}'}(z)$ decides which parts of the wavefunction will experience a significant change in their potentials and thus a change in their own intensity.
The system can in principle be solved easily but the boundary values of the involved wavefunctions must be known. Based on the low incident energies of the incident beam, no helium atom can penetrate the surface so the wavefunction has to vanish for $z \to -\infty$. Likewise, wavefunctions where the normal energy $\mathbf{k}^2_{\mathbf{G},z}$ is smaller than 0 can not possess real intensities at $z \to +\infty$ and will decay exponentially. Wavefunctions with $\mathbf{k}^2_{\mathbf{G},z} > 0$ on the other hand should be describable by a plane wave as soon as the asymptotic potential can be assumed as constant.

$$\Psi_{\mathbf{G}}(z \to -\infty) \;=\; 0 \tag{3.62}$$

$$\Psi_{\mathbf{G}}(z \to \infty) \;=\; \begin{cases} k_{\mathbf{G},z}^{-1/2} \mathrm{e}^{-\mathrm{i}k_{\mathbf{G},z}z}\delta_{\mathbf{G},\mathbf{0}} + k_{\mathbf{G},z}^{-1/2} S_{\mathbf{G}} \mathrm{e}^{\mathrm{i}k_{\mathbf{G},z}z}, & \text{if } \mathbf{k}_{\mathbf{G},z}^2 > 0 \\ \kappa_{\mathbf{G},z}^{-1/2} S_{\mathbf{G}} \mathrm{e}^{-\kappa_{\mathbf{G},z}z}, & \text{if } \mathbf{k}_{\mathbf{G},z}^2 < 0 \end{cases} \tag{3.63}$$

with $\kappa_{\mathbf{G},z} = \sqrt{-k_{\mathbf{G},z}^2}$. The measured scattering intensities are related to the amplitude of the wavefunctions via

$$I_{\mathbf{G}} \;=\; |S_{\mathbf{G}}|^2. \tag{3.64}$$

Equation 3.63 furthermore includes the incident wave with an amplitude of 1 for the channel $\mathbf{G} = \mathbf{0}$.

Systems of coupled equations can be solved in several ways, the present code however is using a method introduced by L. Fox[29]. At first, the close-coupling equations 3.59 have to be remodeled to

$$\frac{\mathrm{d}^2}{\mathrm{d}z^2}\Psi_{\mathbf{G}}(z) \;=\; \sum_{\mathbf{G}'} \left[-\delta_{\mathbf{G},\mathbf{G}'}\mathbf{k}_{\mathbf{G}',z}^2 + V_{\mathbf{G}-\mathbf{G}'}(z)\right] \Psi_{\mathbf{G}'}(z) \tag{3.65}$$

so they can be written as

$$\frac{\mathrm{d}^2}{\mathrm{d}z^2}\mathcal{F} \;=\; \mathcal{W}(z)\mathcal{F}(z) \tag{3.66}$$

with $\mathcal{F}(z) = \Psi_{\mathbf{G}}(z)$ and the propagator matrix

$$\mathcal{W}_{\mathbf{G},\mathbf{G}'} \;=\; -\delta_{\mathbf{G},\mathbf{G}'}\mathbf{k}_{\mathbf{G}',z}^2 + V_{\mathbf{G}-\mathbf{G}'}(z). \tag{3.67}$$

Analogous to Numerov's method, this equation can be discretized via

$$\left[\mathcal{I} - \frac{1}{12}h^2\mathcal{W}_{i+1}\right]\mathcal{F}_{i+1} + \left[\mathcal{I} - \frac{1}{12}h^2\mathcal{W}_{i-1}\right]\mathcal{F}_{i-1} - \left[\mathcal{I} + \frac{10}{12}h^2\mathcal{W}_{i}\right]\mathcal{F}_{i} \;=\; 0 \tag{3.68}$$

with h the step size between the discrete distance points z_i and $z_{i\pm1}$. The Fox-Goodwin algorithm now introduces a *propagator*-matrix $\mathcal{R}$ that changes the wavefunction to its progressive value

$$\begin{aligned} \mathcal{F}_{i-1} &= \mathcal{R}_{i-1}\mathcal{F}_i \\ \mathcal{F}_{i} &= \mathcal{R}_{i}\mathcal{F}_{i+1} \end{aligned} \tag{3.69}$$

From those equations, the propagator matrix can be determined to be

$$\mathcal{R}_i \;=\; \left[\left[2\mathcal{I} + \frac{10}{12}h^2\mathcal{W}_i\right] - \left[\mathcal{I} - \frac{1}{12}h^2\mathcal{W}_{i-1}\right]\mathcal{R}_{i-1}\right]^{-1} \cdot \left[\mathcal{I} - \frac{1}{12}h^2\mathcal{W}_{i+1}\right]. \tag{3.70}$$

Starting with all amplitudes being zero, repeated use of the propagator successively calculates the wavefunctions. As soon as the potentials reach the asymptotic region, the calculated wavefunctions can be extracted. Generally, the wavefunction-vector $\mathcal{F}$ can be written as

$$\mathcal{F}_N \;=\; \begin{pmatrix} \mathcal{S}in \\ 0 \end{pmatrix} + \begin{pmatrix} \mathcal{C}os & 0 \\ 0 & \mathcal{E}xp \end{pmatrix} \cdot \begin{pmatrix} \mathcal{K} \\ \mathcal{E} \end{pmatrix} \tag{3.71}$$

with $\mathcal{K}$ the amplitudes of the observable, *open*, channels ($\mathbf{k}^2_{\mathbf{G},z} > 0$) and $\mathcal{E}$ the amplitudes of the non-observable, *closed*, channels ($\mathbf{k}^2_{\mathbf{G},z} < 0$). The $\mathcal{S}in$ represents the impinging plane wave with normalized intensity. The attentive reader will wonder why all the open channels have an impinging wave attached, when the intention is to calculate the scattering from one channel into all the others. The formalism introduced here does not distinguish between different channels and calculates the scattering intensities from every channel into every other channel simultaneously. At the end of the calculation only the scattering probabilities are extracted that originate from an impinging wave at $\mathbf{G} = 0$. The matrices $\mathcal{S}in$, $\mathcal{C}os$ and $\mathcal{E}xp$ are filled according to the following rules

$$\begin{aligned}
[\mathcal{S}in]_{\mathbf{G},\mathbf{G}'} &= \frac{1}{\sqrt{|\mathbf{k}_{\mathbf{G},z}|}} \sin(|\mathbf{k}_{\mathbf{G}'z}|z)\delta_{\mathbf{G},\mathbf{G}'} \\
[\mathcal{C}os]_{\mathbf{G},\mathbf{G}'} &= \frac{1}{\sqrt{|\mathbf{k}_{\mathbf{G},z}|}} \cos(|\mathbf{k}_{\mathbf{G}'z}|z)\delta_{\mathbf{G},\mathbf{G}'} \\
[\mathcal{E}xp]_{\mathbf{G},\mathbf{G}'} &= \frac{1}{\sqrt{|\mathbf{k}_{\mathbf{G},z}|}} \exp(-|\mathbf{k}_{\mathbf{G}'z}|z)\delta_{\mathbf{G},\mathbf{G}'}.
\end{aligned} \tag{3.72}$$

To arrive at a useable expression to determine $\mathcal{K}$, equation 3.71 has to be combined with equation 3.69

$$\begin{pmatrix} \mathcal{S}in_{N-1} \\ 0 \end{pmatrix} + \begin{pmatrix} \mathcal{C}os_{N-1} & 0 \\ 0 & \mathcal{E}xp_{N-1} \end{pmatrix} \cdot \begin{pmatrix} \mathcal{K} \\ \mathcal{E} \end{pmatrix} = \mathcal{R}_{N-1} \cdot \left[\begin{pmatrix} \mathcal{S}in_N \\ 0 \end{pmatrix} + \begin{pmatrix} \mathcal{C}os_N & 0 \\ 0 & \mathcal{E}xp_N \end{pmatrix} \cdot \begin{pmatrix} \mathcal{K} \\ \mathcal{E} \end{pmatrix} \right]. \tag{3.73}$$

The exponential intensities of the forbidden wavefunctions $\mathcal{E}$ are of no interest and can, due to the numerical treatment, even diverge. From the wavefunction intensities $\mathcal{K}$ we arrive at the *reaction matrix* $\mathcal{S}_{\mathbf{G},\mathbf{G}'}$

$$\mathcal{S}_{\mathbf{G},\mathbf{G}'} = (1 - \mathrm{i}\mathcal{K})^{-1}(1 + \mathrm{i}\mathcal{K}). \tag{3.74}$$

Since only the $\mathbf{G} = 0$ is initially populated, only one line in $\mathcal{S}_{\mathbf{G},\mathbf{G}'}$ is of physical meaning to us

$$S_{\mathbf{G}'} = \mathcal{S}_{0,\mathbf{G}'} \tag{3.75}$$

Channel convergence and kinematical analysis

The close coupling algorithm derived in this chapter is in principle exact as long as only elastic scattering interactions are involved. However, for the solution to be exact an infinite number of reciprocal lattice vectors has to be taken into account. Usable software can only consider a finite number of reciprocal lattice vectors - thus the major question is *which* vectors are most important and *how many* vectors are really needed. The different possibilities for scattering differ mostly in their respective normal energies. These different possibilities are called *diffraction channels*. These diffraction channels,

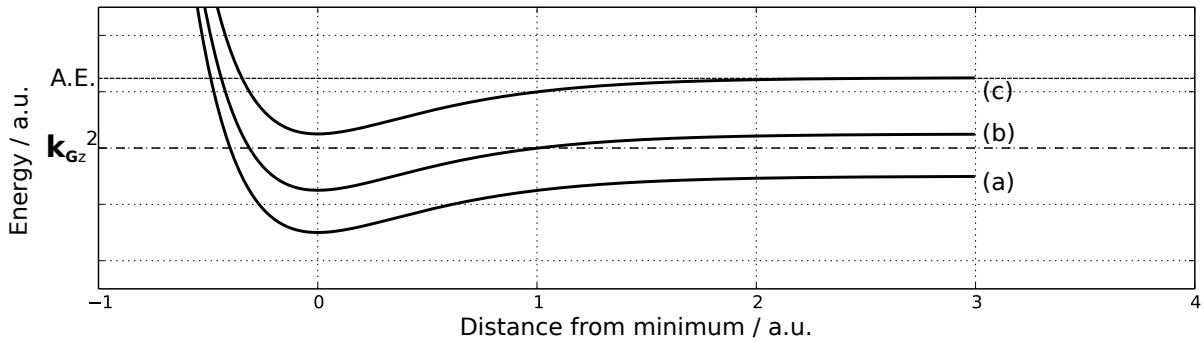

Figure 3.16: Schematic representation of the three different scattering channels in CC calculations. The dash-dotted line represents the total perpendicular energy of the particle after the scattering event, $\mathbf{k}_{\mathbf{G}z}^2$. The asymptotic energy $(\mathbf{K}_i + \mathbf{G})^2$ is only marked for channel (c) and labeled as *A.E.*. Channel (a) is generally refered to as *open*, while channels (b) and (c) are in principle *closed*.

due to their respective normal energies equation 3.60 encounter different, shifted central interaction potentials

$$V_{\mathbf{0}}(z) + (\mathbf{K}_i + \mathbf{G})^2 \tag{3.76}$$

where the term $(\mathbf{K}_i + \mathbf{G})^2$ is usually denoted as the *asymptotic energy* of the channel (see figure 3.16). Due to the relative positions of these potentials with respect to their normal channel energies, three different cases can be distinguished:

- $(\mathbf{K}_i + \mathbf{G})^2 < \mathbf{k}_{\mathbf{G}z}^2$,
  potential (a) in figure 3.16. The channel is called *open*. In principle a continuum of scattering channels is allowed in this regime which will carry scattering intensity. The states are denoted as $|\mathbf{K}_i + \mathbf{G}, \mathbf{k}_{\mathbf{G}z}^2\rangle$. Since there is only a finite number of reciprocal lattice vectors leading to open channels, all open channels can and should be included in the calculation.

- $(\mathbf{K}_i + \mathbf{G})^2 - D < \mathbf{k}_{\mathbf{G}z}^2 < (\mathbf{K}_i + \mathbf{G})^2$,
  potential (b) in figure 3.16. Generally, these channels are called *closed* since the respective normal energy $\mathbf{k}_{\mathbf{G}z}^2$ does not allow the scattered particle to leave the surface and carry scattering intensity. However, close to the surface, the normal energy may coincide with a bound state of the interaction potential, rendering real intensity in this wavefunction possible. Due to the discrete character of bound state energies the allowed scattering states are also discrete and labeled by $|\mathbf{K}_i + \mathbf{G}, \nu\rangle$, with ν being the integer number of the respective bound state. Possible resonant channels should be included in the calculation.

- $\mathbf{k}_{\mathbf{G}z}^2 < (\mathbf{K}_i + \mathbf{G})^2 - D$,
  potential (c) in figure 3.16. The channel is *closed* and so far off the normal energy that no resonant interactions are possible. Wavefunctions belonging to closed channels energetically close to open channels however may fluctuate in the scattering process and thus alter the experienced interaction potential of other channels (see equation 3.59). The amount of closed channels in the calculation can be severely limited and must be determined by a convergency test.

Furthermore, the integration region, namely starting and end value of the integration range can be limited. The integration should start inside the forbidden region of the interaction potential, where all wavefunction contributions can safely be assumed as unpopulated and should end in a region where the interaction potential is unchanging enough so the shape of the wavefunctions can be assumed to behave like the border values require (equation 3.63). Another convergence parameter is the number of z-steps that are performed. The developed code automatically calculates the wavelength of the highest-energy channel, thus the shortest wavelength encountered in the calculation. The parameter set in the function determines how many steps should be performed within this shortest length. Usually, a value around 100 is sufficient. These parameters should be optimized in order to produce a sufficiently exact solution, but also minimize the calculation time. Simulations that should be compared with experimental results usually are sufficiently converged if the solution is exact up to 1% of the absolute value. The calculation time scales linearly with the range parameters ($z_{max} - z_{min}, n_{step}$) but scales proportional to N^3 with N the number of included channels[63].

3.9.5 Debye-Waller Factor

Common theoretical treatments of the scattering processes presented so far assume the surface to be at complete rest and the crystal periodicity to be perfect. Introducing a finite surface temperature however alters the prerequisites of a realistic surface model. Due to thermal movements the crystal surface can neither be assumed as at rest or as perfectly periodic. Those thermal effects attenuate the observed peak intensity of the elastic scattering peaks and are usually described by

$$I(T_S) \;=\; I_0 \cdot \mathrm{e}^{-2W(T_S)} \tag{3.77}$$

with the *Debye-Waller factor* $W(T_S)$ in the exponent defined as

$$2W(T_s) \;=\; \left\langle (\mathbf{u} \cdot \Delta\mathbf{k})^2 \right\rangle_{T_S}, \tag{3.78}$$

$\mathbf{u}$ being the displacement vector of the lattice atom out of its equilibrium position and $\Delta\mathbf{k}$ the total change in momentum of the scattered particle. Regarding only the specular contribution, the surface parallel momentum does not change. This approximation yields

$$2W(T_s) \;=\; \left\langle u_z^2 \right\rangle \cdot (\Delta k_z)^2, \tag{3.79}$$

with $\langle u_z^2 \rangle$ the average squared atomic displacement perpendicular to the surface. Assuming the vibrational behavior to be like a harmonic oscillator, it can be described as

$$\langle u_z^2 \rangle = \frac{3k_B T}{M\omega^2} \tag{3.80}$$

with M the effective mass of the surface atoms. For the vibrational frequency ω, the Debye frequency can be used

$$\omega_D = \frac{k_B \Theta_D}{\hbar} \tag{3.81}$$

with Θ_D the *Debye temperature*. Combining all these statements, the Debye-Waller (DW) factor can be expressed as

$$W(T_S) = \frac{3\hbar^2 T_S}{2Mk_B\Theta_D^2}\Delta k_z^2. \tag{3.82}$$

3.9.6 Beeby Correction

In basic elastic scattering analysis, the *Hard Corrugated Wall* model (see Section 3.4.3), is usually used. Here, the scattering process is only influenced by the plain structural properties of the surface layer, not taking into account the attractive interaction due to dispersion forces. In a more realistic approach, the helium atoms are accelerated by the attractive interaction towards the surface and thus the change in perpendicular momentum during the scattering process is higher than assumed by a hard corrugated wall. This can easily be included into the Debye-Waller attenuation factor, equation 3.82 by assuming

$$\Delta k_z = 2k_i\sqrt{\cos^2(\theta_i) + \frac{D}{E_i}} \tag{3.83}$$

for the specular position $\theta_i = \theta_f$, with D the potential well depth and $E_i = \frac{\hbar^2 k_i^2}{2m}$ the incident particle energy. Thus, including the *Beeby correction*, equation 3.82 reads as

$$W(T_S) = \frac{12m\left[E_i\cos^2(\theta_i) + D\right]}{Mk_B\Theta_D^2}T_S. \tag{3.84}$$

3.9.7 Inelastic Close-Coupling

The simple exponential expression for the thermal attenuation introduced for the Debye-Waller factor in equation 3.77 can pose a severe problem for surfaces with a comparatively small surface Debye temperature, since in this case the DW-Factor equation 3.84 produces a very steep decline of the expected intensity with the surface temperature. Furthermore, the Debye-Waller factor may only be validly used for the attenuation of the specular intensity, though the behavior of the scattering peaks has also been described using an additional hypothetical Debye temperature[71].

Introducing inelastic scattering possibilities into an exact method such as the close coupling formalism opens the possibility to study the temperature-dependent attenuation with a solid theoretical base. In this case, the crystal is described by the rigid equilibrium grid that was already introduced in the elastic case and periodic deviations $\mathbf{u}(\mathbf{R},t)$ of the atoms from their equilibrium positions. Knowing the deviations are time-dependent, the time-dependent Schrödinger equation is used

$$\mathrm{i}\hbar\frac{\partial\Psi(\mathbf{r},t)}{\partial t} \;=\; \left[-\nabla^2+V(\mathbf{r},t)\right]\Psi(\mathbf{r},t). \tag{3.85}$$

The somewhat complicated dependence of the overall potential $V(\mathbf{r},t)$ from the atomic positions can be approximated by a Taylor expansion up to first order, assuming the periodic atomic deviations are small

$$V(\mathbf{r},t)\simeq V(\mathbf{r})+\mathbf{u}(\mathbf{R},t)\cdot\nabla V(\mathbf{r}) \tag{3.86}$$

with $V(\mathbf{r})$ the static potential of the rigid equilibrium grid which can be, equivalent to the elastic case, developed into a Fourier series

$$V(\mathbf{r})=\sum_{\mathbf{G}}V_{\mathbf{G}}(z)\mathrm{e}^{\mathrm{i}\mathbf{G}\cdot\mathbf{R}}. \tag{3.87}$$

The deviation from the equilibrium position $\mathbf{u}(\mathbf{R},t)$ is described by a term from the layer description of lattice dynamics[73]

$$\mathbf{u}(\mathbf{R},t)=\sum_{\mathbf{Q},\nu}\mathbf{A}(\mathbf{Q},\nu,T)\mathrm{e}^{\mathrm{i}\mathbf{Q}\cdot\mathbf{R}}\cos\left[\omega_\nu(\mathbf{Q})t\right]. \tag{3.88}$$

As has been done in the elastic case, the total wavefunction $\Psi(\mathbf{r},t)$ is also developed in terms of reciprocal lattice vectors and periodic time

$$\Psi(\mathbf{r},t) \;=\; \mathrm{e}^{-\mathrm{i}\mathbf{k}_i^2t/\hbar}\sum_{\mathbf{G},\mathbf{Q},\nu,n_{\mathbf{Q},\nu}}\Psi_{\mathbf{G}+\mathbf{Q},n_{\mathbf{Q},\nu}}(z)\cdot\mathrm{e}^{\mathrm{i}(\mathbf{K}_i+\mathbf{G}+\mathbf{Q})\cdot\mathbf{R}}\mathrm{e}^{\mathrm{i}n_{\mathbf{Q},\nu}\omega_\nu(\mathbf{Q})t}, \tag{3.89}$$

and can be introduced into the time-dependent Schrödinger equation 3.85. Here, only one possible phonon energy is included. To calculate the total intensity when interacting with all possible phonon energies, an integral of the single calculated intensities has to be performed. After multiplying both sides by $\exp(-\mathrm{i}(\mathbf{K}_i+\mathbf{G})\cdot\mathbf{R})$ and $\exp(-in\omega t)$ and integrating over time and the unit cell area, one obtains the system of coupled differential

equations

$$\left[\frac{\mathrm{d}^2}{\mathrm{d}z^2} + \mathbf{k}^2_{\mathrm{G},n,z} - V_{\mathbf{0}}(z)\right]\Psi_{\mathbf{G},n}(z) = \sum_{\mathbf{G}\neq\mathbf{G}'} V_{\mathbf{G}-\mathbf{G}'}(z)\Psi_{\mathbf{G}',n}(z)$$
$$+\frac{1}{2}\mathbf{A}\cdot\sum_{\mathbf{G}'}\left[\mathbf{F}_{\mathbf{G}-\mathbf{G}'}(z)+\mathbf{F}_{\mathbf{G}-\mathbf{G}'}(z)\right]\left[\Psi_{\mathbf{G}',n+1}(z)+\Psi_{\mathbf{G}',n-1}(z)\right],$$
$$\left[\frac{\mathrm{d}^2}{\mathrm{d}z^2} + \mathbf{k}^2_{\mathrm{G},n+1,z} - V_{\mathbf{0}}(z)\right]\Psi_{\mathbf{G},n+1}(z) = \sum_{\mathbf{G}\neq\mathbf{G}'} V_{\mathbf{G}-\mathbf{G}'}(z)\Psi_{\mathbf{G}',n}(z)$$
$$+\frac{1}{2}\mathbf{A}\cdot\sum_{\mathbf{G}'}\left[\mathbf{F}_{\mathbf{G}-\mathbf{G}'}(z)+\mathbf{F}_{\mathbf{G}-\mathbf{G}'}(z)\right]\left[\Psi_{\mathbf{G}',n+2}(z)+\Psi_{\mathbf{G}',n}(z)\right], \tag{3.90}$$

with

$$\mathbf{k}_{\mathbf{G},n,z} = \mathbf{k}_i^2 - (\mathbf{K}_i+\mathbf{G})^2 - n\hbar\omega \tag{3.91}$$

the surface perpendicular energy after the scattering process and

$$\mathbf{F}_{\mathbf{G}-\mathbf{G}'}(z) = \left[\mathrm{i}(\mathbf{G}-\mathbf{G}')V_{\mathbf{G}-\mathbf{G}'}(z), V'_{\mathbf{G}-\mathbf{G}'}(z)\right] \tag{3.92}$$

the parallel and perpendicular contributions of the gradient of the interaction potential. Following the same nomenclature as in the elastic case, a scattering channel is defined by its asymptotic energy

$$(\mathbf{K}_i+\mathbf{G})^2 + n\hbar\omega, \tag{3.93}$$

and the open and closed channels are denoted as $|\mathbf{K}_i+\mathbf{G},n,\nu\rangle$ and $\left|\mathbf{K}_i+\mathbf{G},n,\mathbf{k}^2_{\mathbf{G},n,z}\right\rangle$, following the rules in section 3.9.4. The additional parameter n accounts for the respective number of phonon interactions. The possible number of total interactions defines how many additional *inelastic* channels accompany the elastic channels on both sides. Those regions of inelastic possibilities are called *Floquet blocks* and their total number is an additional fitting parameter in inelastic close-coupling (iCC) calculations.
Next to the elastic coupling parameters developed for the elastic close coupling, also interaction of elastic channels with inelastic ones has to be taken into account for a full inelastic treatment. The scalar function

$$\mathbf{A}(T)\cdot\mathbf{F}_{\mathbf{G}-\mathbf{G}'}(z) \tag{3.94}$$

represents this inelastic *interblock* coupling. Usual inelastic coupling calculations are performed in the Debye model, including solely the linear Rayleigh dispersion. This Rayleigh branch is usually of a nearly shear-vertical character, yielding little to no horizontal displacement. Due to this fact, the first term in equation 3.92 can be assumed as zero and the total interaction to be assumed is

$$\mathbf{A}(T)\cdot\mathbf{F}_{\mathbf{G}-\mathbf{G}'}(z) \simeq \mathbf{A}(T)\cdot V'_{\mathbf{G}-\mathbf{G}'}(z), \tag{3.95}$$

with $V'_{\mathbf{G}-\mathbf{G}'}(z)$ the spacial derivative of the coupling function (i.e. equation 3.57). In the corrugated Morse case, this function is especially simple and can be evaluated analytically. The thermal displacement amplitude $\mathbf{A}(T)$ presents another fitting parameter but has been derived for various copper surfaces as[73]

$$\mathbf{A}(T) = \frac{1}{aQ_c}\sqrt{\frac{384\hbar^2\pi T}{Mk_{\mathrm{B}}\Theta_D^2}}, \tag{3.96}$$

with Q_c the Gaussian cut-off factor of the harmonic movement. The thus obtained system of equations can be solved in exactly the same way as in the elastic case described in section 3.9.4.

It is worthy to note that phonon modes included in this way still do not possess momentum, in a dispersion relation the phonon modes would all be present at the Γ-point. Inclusion of the phonon momentum presents a nontrivial challenge, since this momentum transport will certainly influence the coupling that has to be introduced. Furthermore this approach so far only includes the possibility of one single phonon mode. To extend the calculation to the influence of all the modes within one phonon (Rayleigh-) branch, the calculated intensities have to be integrated over all phonons[80]

$$\langle I_{\mathbf{G}+\mathbf{Q}}\rangle = \int_0^{\omega_D} I_{\mathbf{G}+\mathbf{Q},n_{\mathbf{Q},\nu}}\rho(\omega_\nu(\mathbf{Q}))d\omega_\nu(\mathbf{Q}) \tag{3.97}$$

with $\rho(\omega_\nu(\mathbf{Q}))$ being the phonon spectral density usually given in the Debye model via

$$\rho(\omega) = \frac{2\omega^2}{\omega_D^3}, \tag{3.98}$$

with ω_D being the Debye frequency of the underlying crystal.

4 Pnictogen Surfaces

Pnictogens, better known from semiconductor physics as *Group-V elements*, are the elements listed in the fifteenth column of the periodic table of elements. The pnictogen materials possess electrical properties on a very wide scale, from nitrogen (N) being a gaseous nonmetal over the two metalloids arsenic (As) and antimony (Sb) to the heaviest element denoted as *stable*, the semimetal bismuth (Bi). As typical for elements sharing the same column in the periodic table, the pnictogens exhibit similar chemical behavior with each having three unpaired electrons in the p-shell. Resulting from this similar behavior, also the crystal structure of the heavier pnictogens is very similar. Starting with gray arsenic, the heavier Group-V elements crystallize in a rhombohedral A7 structure with two atoms per unit cell. This structure can typically be described as an arrangement of puckered bilayers of atoms perpendicular to the [111] direction, as depicted in figure 4.2(a). Due to a very weak bonding in between those bilayer structures, the natural cleavage plane of the pnictogen crystals is perpendicular to the [111] direction. A top-down view on the resulting surface is given in figure 4.2(b). While the overall crystal surface is threefold symmetric, the uppermost layer is of a hexagonal shape and thus sixfold symmetric. It has been found that due to the low incident energy of the impinging helium atoms, the surface may be regarded as sixfold symmetric in helium atom scattering experiments[89,90]. This sixfold symmetric structure can mathematically be described by

$$\xi(x,y) = \xi_0 \cdot \left(\cos\left[\frac{2\pi}{a}\left(x - \frac{y}{\sqrt{3}}\right)\right] + \cos\left[\frac{2\pi}{a}\left(x + \frac{y}{\sqrt{3}}\right)\right]\right) + \xi_0 \cdot \cos\left[\frac{2\pi}{a} \cdot \frac{2y}{\sqrt{3}}\right]. \quad (4.1)$$

4.1 Properties of Bi(111)

Being the heaviest material regarded as *stable*, the extraordinarily high mass of bismuth of 208.98 a.u. gives rise to several atypical properties that might be useful in the new-developing fields of superconductivity, topological materials or spintronics[39,43,76,93,94,98,100,102]. The most challenging aspect of this high mass for theorists is the extremely high spin-orbit coupling it provokes and its implications on the electronic properties of the surface.

						He
	B	C	N	O	F	Ne
	Al	Si	P	S	Cl	Ar
...	Ga	Ge	As	Se	Br	Kr
...	In	Sn	Sb	Te	I	Xe
...	Tl	Pb	Bi	Po	At	Rn

Figure 4.1: Section of the periodic table of elements. The group V-elements, generally denoted as pnictogens contain the investigated elements bismuth and antimony

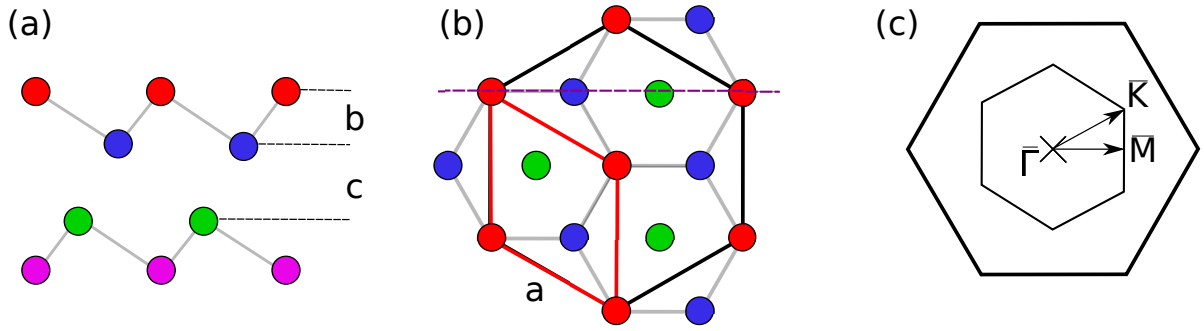

Figure 4.2: Surface structure of the heavy pnictogens.
(a) Side-view of the (111)-surface. The crystal is built up by puckered bilayers weakly bound to each other.
(b) Top-down view of the (111) surface. The upper layer possesses a sixfold symmetry while the whole structure is only three-fold symmetric. Figure (a) corresponds to the cut marked by the purple dashed line. (c) Reciprocal-space structure of the pnictogen(111) surface corresponding to the real-space picture in (b). For the sixfold structure there are two high-symmetry directions $\overline{\Gamma M}$ and $\overline{\Gamma K}$.

4.1.1 Bi(111) surface structure

The surface structure of bismuth is of the hexagonal character described above and corresponds to figure 4.2(b) with a lattice constant of $a = 4.538$ Å. The intra-bilayer distance b as well as the inter-bilayer distance c were determined to be 1.59 Å and 2.35 Å respectively, by Mönig et. al.[75].

4.1.2 Bi(111) electronic surface properties

While being a poor conductor in the bulk, the symmetry break introduced by the surface provokes the electron bands on the Bi(111) surface to cut the Fermi level, introducing localized conducting surface states. A specialty arising from the large spin-orbit coupling in Bi(111) is that the surface states are spin-polarized, resulting in the fact that opposite electron states (with respect to the Γ-point) possess opposing spin directions, see figure 4.3[39].

4.1.3 Bi(111) vibrational surface properties

The extremely high nuclear mass of bismuth not only affected theoretic calculations on the phononic dispersion of Bi(111), also the measurement of the surface phonons can be seen as a nontrivial task since due to the high mass the respective phonon energies are extremely low (see equation 3.10). The peak energy of roughly 3 meV of the acoustic Rayleigh branch borders the resolution of the available HAS apparatus (see Section 2). The surface acoustic lattice dynamics of Bi(111) were first described by Tamtögl et. al.[89,90] and further extended to the optical phonon dispersion by Kraus et. al.[55]. The latter article is featured in this thesis in Chapter 5.

4.2 Properties of Sb(111)

Antimony is the lighter brother of bismuth with an atomic mass of *'only'* 121.76 a.u.. While in comparison it is nearly half the weight of bismuth, antimony still displays effects inherited from the large spin-orbit interaction. Antimony was found to be a topological semimetal on its own, explaining the good surface conductivity in comparison to the relatively poor conducting bulk.

4.2.1 Sb(111) surface structure

As in bismuth, the surface structure of antimony is equivalent to the one shown in figure 4.2 with the lattice parameters a, b and c measured by James, Tunstall and Ogg[46,77] as a = 4.3084 Å, b = 1.50 Å and c = 2.24 Å.

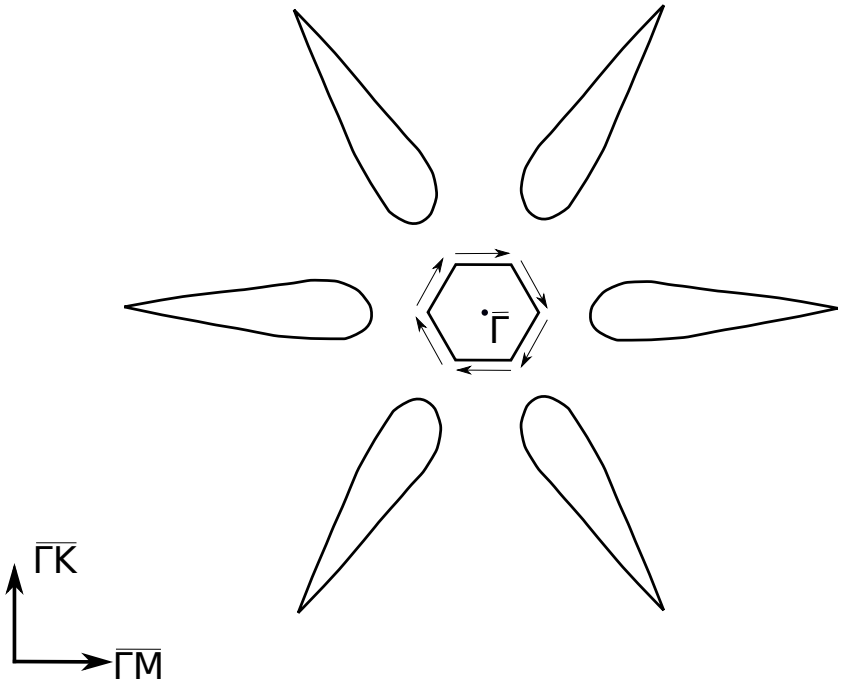

Figure 4.3: Shape of the central Fermi cut on the Bi(111) surface[39]. Close around the Γ-point, spin-helical electron states should forbid direct intraband-transitions[49]

4.2.2 Sb(111) electronic surface properties

The conducting surface bands in Sb(111) resemble the electronic structure encountered in Bi(111) (figure 4.3). Also the central cut through the Fermi surface is hexagonal, but the radius is slightly larger than in the case of Bi(111).

5 Resonance-enhanced inelastic He-atom scattering from sub-surface optical phonons of Bi(111)

The following corresponds to a publication by
Patrick Kraus, Anton Tamtögl, Michael Mayrhofer-Reinhartshuber, Giorgio Benedek, and Wolfgang E. Ernst in *Physical Review B*, **87**:245433-1-7, June 2013[55].

The author of this thesis was responsible for

- performing HAS time-of flight (TOF) measurements on Sb(111)
- implementation of the basic HAS analysis algorithms used for figures 5.1(a), 5.4, 5.6, 5.7 and 5.8
- calculation of bound-state levels from the positions of the resonance effects given in figure 5.4
- calculation of the best-fitting interaction potential given in figure 5.5
- analysis of the TOF data in the optical region on resonance effects.

The contributions of the co-authors are listed below:

- A. Tamtögl: HAS-measurements, angular and TOF,
- M. Mayrhofer-Reinhartshuber: HAS-measurements, angular and TOF,
- Giorgio Benedek: Resonance analysis in the angular scans, TOF analysis, authorship of the introduction 5.1, supporting authorship of sections 5.4, 5.5 and 5.6
- W.E. Ernst: supervision (experiment, theory, publication), laboratory, funding

Abstract

Helium-atom scattering angular distributions from Bi(111) show a number of selective-adsorption resonance features corresponding to three bound states of the He atom in the surface-averaged Bi(111) potential. They are well represented by a 3-9 potential with a potential depth of 8.3 meV. The bound-state resonance enhancement of inelastic scattering is shown to provide the mechanism for the observation of subsurface optical phonons and for their comparatively large intensity.

5.1 Introduction

It has been recently shown that inelastic helium-atom scattering (iHAS) from metal surfaces can detect subsurface phonons localized several layers beneath the surface, the depth being determined by the range of the electron-phonon (e-p) interaction[8,82]. This effect is particularly pronounced in ultra-thin metallic films where the e-p interaction receives the largest contribution from quantum-well (QW) electronic bands and QW-confined phonons.
A recent study by iHAS of the surface phonon dispersion curves in Bi(111)[71,89,90] revealed unexpected large intensities from the optical branches of shear vertical (SV) polarization confined in the first bilayer (SV1 branch) as well as in the second bilayer (SV3 branch).

This can be better appreciated from a direct comparison of two iHAS spectra from the (111) surface of bismuth[89,90] and, e.g., six monolayers of lead on a Cu(111) substrate[16] measured under comparable kinematic conditions (Fig. 5.1). The optical surface phonons of Bi(111), which are separated from the acoustic band by a gap ranging from 7.5 to 9.0 meV[89,90], are considerably stiffer than the corresponding modes in the Pb(111) film (ϵ_1, ϵ_2) and would therefore be expected to have a weaker iHAS intensity. On the contrary, the iHAS intensity of the optical breathing mode (OBM) in the first bilayer (SV1) of Bi(111) is the largest of the spectrum (Fig. 5.1(a)), unlike that for the OBM (ϵ_1) in the first bilayer of Pb(111) which is weaker than the acoustic mode intensities (α_1, α_2) (Fig. 5.1(b)). On the other hand, the OBM in the second bilayer of Bi(111) (SV3) is much weaker than SV1, whereas in Pb(111) both the surface mode ϵ_1 and the subsurface mode ϵ_2 (localized at the Pb/Cu interface!) have comparable iHAS intensities, but are considerably weaker than the iHAS intensity from the acoustic branches α_1 and α_2.
One should now consider that for a conducting surface iHAS intensities are proportional to the square of phonon-induced surface charge density oscillations (SCDOs) and therefore to the corresponding mode-selected e-p coupling strengths[82]. A calculation based on density-functional perturbation theory (DFPT) for Bi(111)[89,90] has shown that the SCDO induced by the breathing mode of the second bilayer (SV3) is about four times

smaller than that for the first bilayer breathing mode (SV1) which means a factor 16 smaller iHAS intensity.

This is consistent with the fact that the surface conductivity of the Bi(111) surface is substantially restricted to the first bilayer, and accounts for the ratio SV3/SV1 of the optical mode intensities as reported in Fig. 5.1(a). In our previous study[89,90] we found, however, that under certain kinematic conditions iHAS intensities from the optical SV3 modes were often comparable to those of SV1 optical modes, which allowed to determine both branches with sufficient confidence. In a further analysis, reported in this work, we singled out a mechanism for the enhancement of iHAS intensities from subsurface optical modes which is specific to semimetal surfaces.

Despite the fact that semimetal surfaces are normally conducting and therefore posess free surface electrons, they are found to be strongly corrugated, unlike the low-index surfaces of ordinary metals which are perfectly flat. This is due to the concentration of surface electrons and holes at the Fermi energy into comparatively narrow pockets around the symmetry points of the surface Brillouin zone (SBZ)[39]. The surface corrugation, besides providing the intensities of elastic diffraction peaks and information on the surface geometry and the associated surface electron density, also allows for the selective adsorption of incident He atoms into surface bound states via the exchange of a reciprocal surface lattice vector. The interference between the direct and bound-state-mediated scattering channels yields a modulation of the elastic intensities and, more importantly in the present work, a modulation of the iHAS amplitudes (inelastic bound-state resonance). Actually a strong resonance enhancement can be obtained through a suitable tuning of the He beam incident angle and energy. This effect has been exploited in the past to detect high-energy optical surface phonons in insulators[15,27].

In this paper we show that the comparatively strong iHAS amplitudes from the subsurface optical mode SV3 of Bi(111) are essentially due to a resonance enhancement involving the strongest bound-state resonance, $(1,0)_2$ with the $n = 2$ bound state and reciprocal lattice vector $\mathbf{G} = (1,0)$. The possibility of tuning the curve representing the $(1,0)_2$ inelastic resonance condition in the energy-momentum space so as to make it nearly tangent to the optical SV3 dispersion curve allows to measure it over a large portion of the SBZ. In this special kinematic situation, recently investigated and known as *surfing*[10], the atom enters the bound-state channel inelastically by creating an optical SV3 phonon and rides for a while the running charge-density wave associated with the SV3 mode, since both the trapped atom and the SV3 phonon travel at the same group velocity along the surface. This exotic form of atomic polaron allows for a strong coupling to the otherwise weak subsurface phonons.

The comparatively large diffraction amplitudes observed in both symmetry directions of Bi(111) reveal a fairly strong corrugation of the surface electron density, which reflects however the peculiar surface band structure better than the actual crystallography of the Bi atoms in the first bilayer. This is recognized from the equal depth of the two hollow

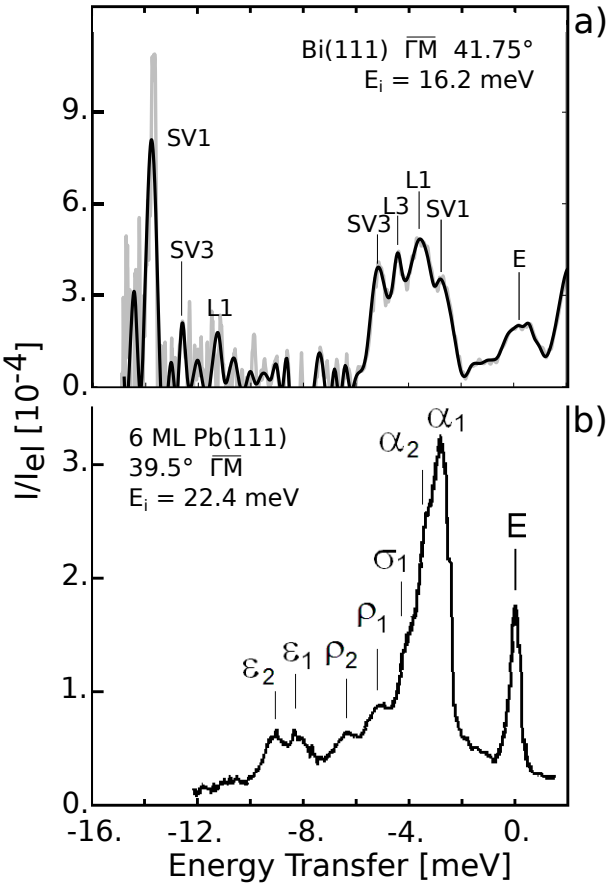

Figure 5.1: Inelastic He atom scattering (iHAS) spectra from the (111) surface of (a) bismuth[89,90] and (b) six monolayers of lead on a Cu(111) substrate[16] measured under comparable kinematic conditions. The optical surface phonons of Bi(111) are separated from the acoustic band by a gap (7.5 to 9.0 meV)[89,90] and are stiffer than the corresponding modes of the Pb(111) film (ϵ_1, ϵ_2). While in Bi(111) the iHAS intensity of the optical breathing mode (OBM) in the first bilayer (SV1) is much larger than that of the OBM in the second bilayer (SV3), in Pb(111) both surface (ϵ_1) and subsurface (ϵ_2 at the Pb/Cu interface) modes have comparable iHAS intensities, but are considerably weaker than the iHAS intensity from the acoustic branches α_1 and α_2. The grey line in (a) shows the actually measured signal while the black line is the result of averaging the original signal to constant energy bins.

sites of the surface unit cell, which would be inequivalent from the crystallographic point of view[89,90]. The bound-state energies derived from the selective adsorption angles have been obtained with sufficient precision to allow for a reliable prediction of the inelastic resonance conditions for the lowest bound states and the smallest G-vectors.
Bismuth, besides being a semimetal, exhibits important differences in the electronic structure of the surface with respect to that of the bulk[1,6,37]. While only high-pressure phases of bismuth are known to become superconducting[101], superconductivity has been reported in Bi clusters, nanowires and bi-crystals, as well as in polycrystalline forms[4,93,98,100]. Moreover spin-orbit coupling in bismuth, besides being more effective than in lead thus making it interesting for future applications in spintronics[39], provides an appreciable contribution to the electron-phonon coupling[20,44]. All that considered, a detailed understanding of He bound-state energies and resonances appears to be a necessary step for a complete HAS spectroscopy of surface phonons in Bi(111).

5.2 The Bi(111) Surface Structure

The (111) surface is the most important one of rhombohedral bismuth, since it is its natural cleavage plane, thus cheap and easily available. The top layer of Bi(111) displays a hexagonal structure with an atomic spacing of $a = 4.54$ Å, Fig. 5.2.
The electronic properties of the Bi(111) surface have been thoroughly investigated[2,37,39]. The most interesting results, reported by Ast et. al.[1], concern the electron and hole pockets of surface states around certain points of the SBZ. Especially the electron pockets at the six $\bar{\text{M}}$-points are expected to contribute to the surface corrugation of the electron density. It should be remembered that the presence of Fermi surface electronic states in all directions yields a flat surface density, as observed, e.g., in Cu(111). Recently Mayrhofer et. al.[71] have indeed reported, by means of HAS measurements, an unexpectedly large electron density corrugation of the Bi(111) surface, in good agreement with ab-initio calculations.

5.3 The Atom-Surface Interaction Potential

The potential between a He atom and a solid surface essentially consists of a short-range repulsive part originating from the Pauli repulsion between the helium closed shell and the electrons of the surface, and of a longer range attractive part due to dispersion (van der Waals) forces. A good description of the atom-surface potential including only dipole-dipole dispersion forces in the attractive part is the 3-9 potential[22]

$$V(z) = \frac{\sqrt{27}}{2} D \left[\left(\frac{\sigma}{z}\right)^9 - \left(\frac{\sigma}{z}\right)^3 \right] \tag{5.1}$$

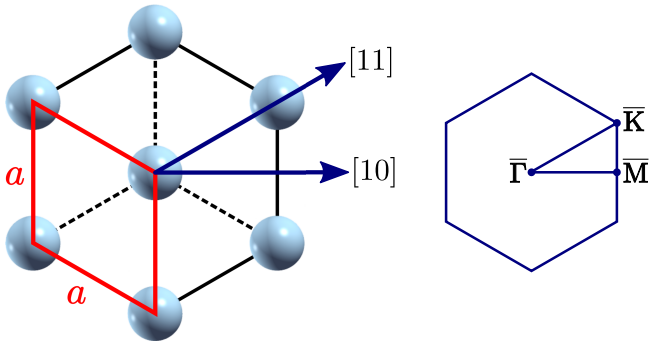

Figure 5.2: Structure of the Bi(111) top surface layer with the two distinguishable directions marked. The lattice spacing parameter is $a = 4.54$ Å[39].

where D denotes the well depth, σ the distance at which the potential vanishes and $z = 3^{1/6}\sigma$ is the position of the potential minimum. The 3-9 potential, Eq.5.1, is readily obtained by summing over the entire semi-infinite lattice of the individual He-solid atomic 12-6 (Lennard-Jones) potentials[22]. The eigenvalue spectrum of this potential for the motion component normal to the surface can be calculated using the distorted wave Born approximation[22], and is found to be

$$E_n = -D\left[1 - \frac{\pi\hbar}{3.07}\frac{n + \frac{1}{2}}{\sigma\sqrt{2mD}}\right]^6 \tag{5.2}$$

with m the He atom mass and E_n the n-th bound-state energy. As seen in the next section, this expression for the bound states works well also in the analysis of the bound-state resonances of a semimetal surface such as Bi(111).

5.4 Selective Adsorption Resonances

The kinematics of a selective adsorption resonance, where a He atom enters elastically a bound state of energy $-|E_n|$ before being scattered inelastically into the final state, is defined by the simultaneous conservation of energy and parallel momentum. The two conservation laws yield the selective-adsorption condition, expressed by the equation[41]

$$\mathbf{k_i}^2 = \left(\mathbf{k_i} sin\theta_i + G_\parallel\right)^2 + G_\perp^2 - \frac{2m}{\hbar^2}\left|E_n\right| \tag{5.3}$$

where k_i is the atom incident wavevector, θ_i the incident angle and $\mathbf{G} = (G_\parallel, G_\perp)$ the surface reciprocal lattice vector mediating the adsorption process. Here $\mathbf{G}$ is split into the components $G_\parallel$ and $G_\perp$ parallel and normal to the incidence plane, respectively.

The resonance condition, Eq.5.3, can be matched either by varying the incident angle θ_i at fixed incident momentum $\mathbf{k_i}$ or by varying the incident momentum at fixed incident

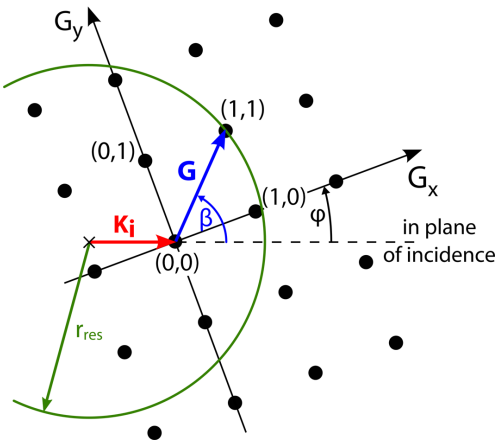

Figure 5.3: Geometrical representation of the resonance condition in equation 5.3 in the reciprocal space (for a cubic lattice). The resultant vector $\mathbf{K_i} + \mathbf{G}$ that leads to a resonant transition lies on a circle with the radius $r_{res}^2 = \mathbf{k_i}^2 + \frac{2m}{\hbar^2}|E_n|$.

angle. (Fig.5.3)
The intensity of a bound-state resonance supported by the exchange of a reciprocal lattice vector $\mathbf{G}$ is proportional to the squared $\mathbf{G}$-th Fourier component of the surface potential at the scattering turning point. Thus bound-state resonances are only observed on a corrugated surface, as it is the case for Bi(111).

For all the observable resonance features in-between elastic peaks a phonon must be involved. In this process, two differing channels can be distinguished, namely 'incident-state' or 'final-state' resonances, depending on when the helium atom is in resonance with the involved bound state level. In the first case the helium atom enters the bound state elastically, while leaving the surface interacting with a phonon. This process yields observable changes in the elastic spectrum in-between the elastic scattering peaks as observed in the elastic spectra in Bi(111). In the case of 'final-state' inelastic resonances, the helium atom enters the bound state channel using the interaction with a phonon. When this helium atom leaves the surface elastically, its energy differs from the beam by the energy of the involved phonon - producing an observable feature in time-of-flight (TOF) measurements[18]. The resonance condition for the latter can be expressed by

$$\mathbf{k_i}^2 - \frac{2m}{\hbar}\omega_{\mathbf{Q}v} = \left(\mathbf{k_i} sin\theta_i + G_{\parallel} + \mathbf{Q}\right)^2 + G_{\perp}^2 - \frac{2m}{\hbar^2}|E_n| \tag{5.4}$$

with $\mathbf{Q}$ and $\hbar\omega_{\mathbf{Q}v}$ the wavevector and the energy of the involved phonon.

5.4.1 Bound-state energies and He-Bi(111) potential

In the absence of corrugation the total energy of an atom trapped into the n-th bound state would be that of an atom freely moving along the surface with momentum $\hbar\mathbf{K}$ shifted by the bound-state energy $-|E_n|$, i.e.

$$E_{\mathrm{kin}}(\mathbf{K}, n) = \frac{\hbar^2 K^2}{2m} - |E_n| \tag{5.5}$$

Corrugation introduces periodic components in the surface potential. The atom wavefunctions are Bloch states, with the appearance of gaps in the bound-state dispersion relations and mass renormalization − the latter effects being more pronounced for more deeply bound states, i.e., for atoms moving closer to the surface[19].
In general these effects are sufficiently small and hard to detect with the present data and the available angular and energy resolution. Thus no mass renormalization is applied in the following analysis, and only the $\mathbf{G} = 0$ component of the surface potential (the laterally-averaged potential) is extracted from the fitting of bound state energies[40].

The present measurements were performed on a HAS apparatus with a 91.5° source-target-detector geometry. The apparatus has been described in greater detail in a previous paper[91]. The time-dependent measurements in the figures 5.1, 5.7 and 5.8 are plotted in two seperate lines. In order to compensate for the non-linearity of the energy scale the intensity of the measured spectrum must be multiplied by the corresponding Jacobian determinant. However, this scaling also increases the height of experimental noise on the creation side, making it difficult to distinguish peaks from noise in the creation region with large energy loss. Therefore, the energy axis of the signal was divided in equally sized energy bins. All the data points falling into one bin have been averaged in order to smooth the signal, resulting in the black line. The Bi(111) single crystal used in this study was a disc with a diameter of 15 mm which has been cleaned by Ar^+ sputtering (1.5 kV, 2 μA) and annealed in three intervals at 423 K for six hours each prior to the measurements. The sample temperature was measured using a chromel-alumel thermocouple. First indications for surface resonance features were observed in HAS angular distributions on Bi(111) whereas the angle of incidence θ_i was changed at constant incident beam energy E_i of 15.1 meV. This allows to extract, in a single angular distribution, information on both the surface structure (via diffraction amplitudes) and bound-state energies (via selective adsorption features, which can be either peaks or dips, depending on the phase shift between direct and resonant channels).

Figure 5.4a displays the enlarged signal of an angular distribution from Bi(111) as a function of the incident angle θ_i along a $\overline{\Gamma\mathrm{K}}$ direction, for the crystal held at room temperature. The features observed at $\theta_i = 32°$, 37°, 42° and 51° in the regions between the specular (0,0) and the first diffraction peaks (1,1) and (-1,-1) at $\theta_i = 45.75°$, 68.75° and 24.75° respectively, are attributed to selective adsorption. The analysis based on Eq. 5.3 allows

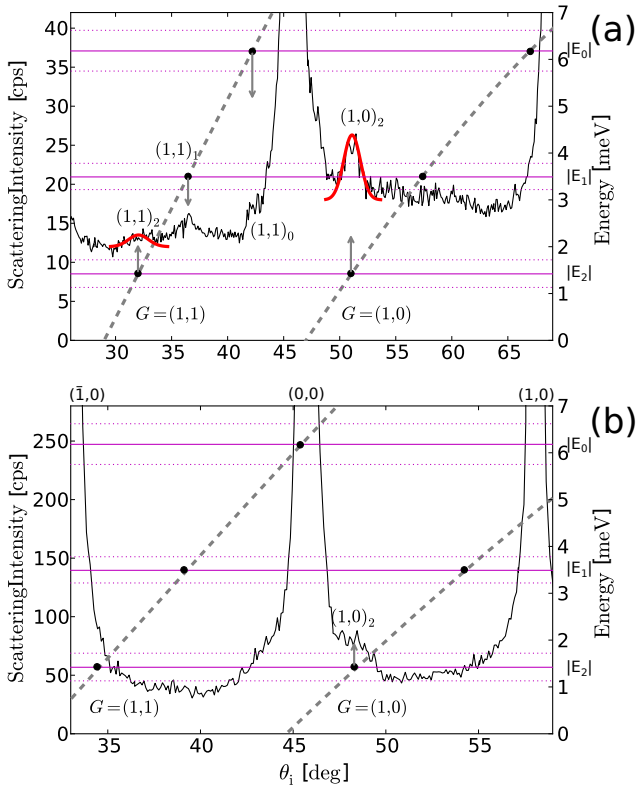

Figure 5.4: (a): Angular distribution of He atom scattering intensity (left-hand ordinate scale) from Bi(111) along a $\overline{\Gamma K}$ surface direction for a 91.5° scattering geometry at a beam energy of 15.1 meV. Besides the specular (0,0) and the two closest diffraction peaks (1,1) and (-1,-1), the angular distribution shows additional features corresponding to selective adsorption processes. The bound state energies which would give a feature in the angular distribution are plotted (broken lines) as functions of the incident angle for the two smallest **G**-vectors indexed by (1,1) and (1,0), respectively allowing for in-plane and out-of-plane resonances (corresponding energy scale on the right-hand side). The vertical arrows associate the resonant features with the energies of three bound states. (b): Same as (a) for the $\overline{\Gamma M}$ direction.

to assign these four resonances to bound states. This is easily done by superimposing to the angular distribution of Fig. 5.4a the curves representing the bound state energy given by Eq. 5.3 as a function of θ_i for different **G**-vectors, the actual values of the latter (in $\mathrm{\AA}^{-1}$) being known from the positions of the diffraction peaks. The two broken lines plotted in Fig. 5.4a correspond to the smallest **G**-vectors indexed by (1,1) and (1,0). The three resonances below the specular peak are clearly associated with the (1,1) channel (in-plane resonances) and three bound states, whereas the large resonance at 51° can be associated with the (1,0) channel (out-of-plane resonance) and the same bound state as the 32° resonance. The (1,0)-channel features associated with the other two deeper bound states are expected at 58° and 66°, and observed to correspond to a broad bump and a small peak, respectively, both hardly detectable above the background noise (no extra position mark in Fig. 5.4). The binding energies derived from these resonances are:

$$\begin{aligned} E_0 &= (6.18 \pm 0.55)\ \text{meV} \\ E_1 &= (3.49 \pm 0.28)\ \text{meV} \\ E_2 &= (1.42 \pm 0.30)\ \text{meV} \end{aligned} \tag{5.6}$$

Once these energy values are derived from the most prominent resonances, other weaker features can eventually be assigned to other combinations $(\mathbf{G})_n$, as for example $(1,1)_2$ and $(1,0)_1$ along the $\overline{\Gamma\mathrm{M}}$ direction (Fig. 5.4b).

In this measurement only one strong resonance feature appears right next to the specular peak. This peak can be identified as the $(1,0)_2$ resonance.

With the experimentally determined bound-state energies the interaction potential parameters can be derived by a least-squares fit of the eigenvalue spectrum of a 3-9 potential (Eq. 5.2). The resulting parameters are:

$$\begin{aligned} D &= (8.32 \pm 0.73)\ \text{meV} \\ \sigma &= (0.297 \pm 0.012)\ \text{nm} \end{aligned} \tag{5.7}$$

Figure 5.5 displays the 3-9-potential according to the best fit parameters, together with its three bound states and the respective confidence intervals. The calculated potential well depth D is consistent with known values for noble metal vicinal (corrugated) surfaces such as Cu(117) ($D = 7.41$ meV)[57] and Ag(111) ($D = 9.3$ meV)[42].

5.4.2 Resonance Effects in the Specular Intensity

After the determination of the bound-state energies, it is interesting to analyze the resonant features which are expected to occur in the specular intensity when measured as

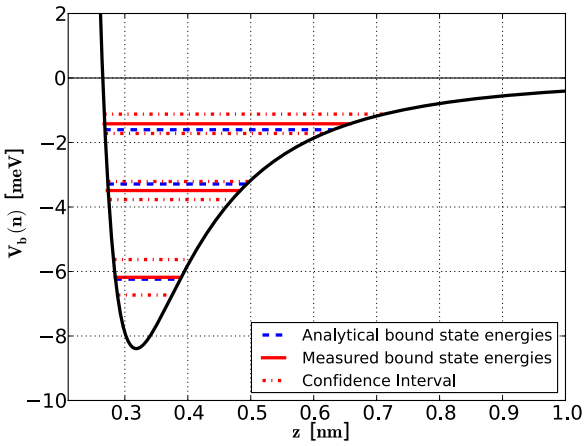

Figure 5.5: Best fit 3-9-potential (Eq. 5.1) for the He-Bi(111) atom-surface interaction with $D = 8.32$ meV and $\sigma = 0.297$ nm. The red (full) lines indicate the experimentally determined bound state energies and their uncertainties (dash-dotted), the blue lines (dashed) correspond to the analytical bound state values from Eq. 5.2 (color online)

Table 5.1: Expected source temperatures T_N and corresponding incident energy E_i at which bound-state resonances are expected to produce a dip in the specular peak intensity with the sample rotated to the $\overline{\Gamma M}$ direction. Resonances are labelled by $(\mathbf{G})_n$.

Resonance	T_N[K]	E_i[meV]
$(0,2)_0$	33	7.7
$(1,1)_0$	70	15.7
$(0,2)_1$	83	18.5
$(0,2)_2$	114	24.6
$(1,1)_1$	127	28.2
$(1,1)_2$	163	35.3

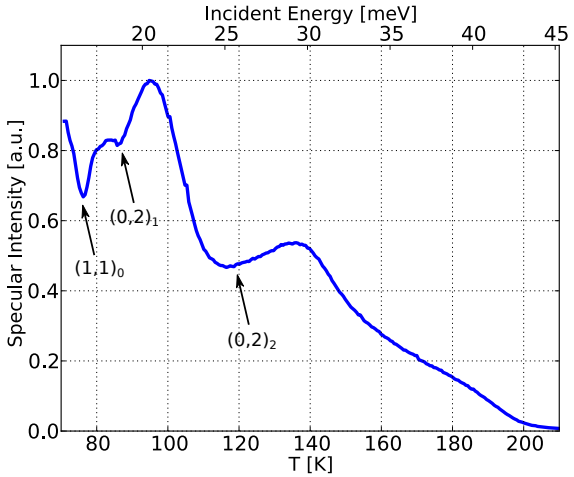

Figure 5.6: Peak height of the specularly reflected helium beam vs. the nozzle temperature in the $\overline{\Gamma M}$ scattering plane. The dips at 76 K, 86 K and the broad feature at 116 K can be explained with the aid of bound state resonances.

a function of the incident momentum. By solving Eq. 5.3 with respect to k_i for the specular θ_i and for given $\mathbf{G}$ and $|\epsilon_n|$, one obtains the values of k_i at which resonances are expected to occur. In principle this experiment can be made at any given incident θ_i, but fixing the incident angle at the specular peak provides the best signal-to- noise ratio.

The peak height of the specular peak was recorded while the nozzle temperature was varied between 60 K and 200 K ($4.5 < k_i < 9$ Å^{-1}) (Fig. 5.6). Since the intensity of the incident helium beam depends on the nozzle temperature as $T_N^{-\frac{1}{2}}$ when resonance effects are not considered[72] and the sample is held at a constant temperature, the specular intensity should show a similar behavior. On the contrary, besides the expected continuous decrease of the intensity, some clear and intense dips at 76, 86 and a broad feature at 116 K are recognizable in the experimental specular intensity plotted in Fig. 5.6. According to the predictions of Table 5.1, the observed dips can be associated to the $(1,1)_0$, the $(0,2)_1$ and the $(0,2)_2$ resonances.

5.5 Resonance-enhanced inelastic scattering

Once the bound state energies have been determined with sufficient precision the positions of inelastic resonances for each bound state and each G-vector involved can be calculated from Eq. 5.4 on the energy-transfer scale for each TOF spectrum, the phonon energy $\hbar\omega_{\mathbf{Q}\nu}$ and wave-vector $\mathbf{Q}$ being related by the energy and parallel momentum conservation laws (*scan curves*). Fig. 5.7 shows an example of a TOF spectrum represented on the energy transfer scale taken along the $\overline{\Gamma K}$ direction for $\theta_i = 44.75°$, a scattering

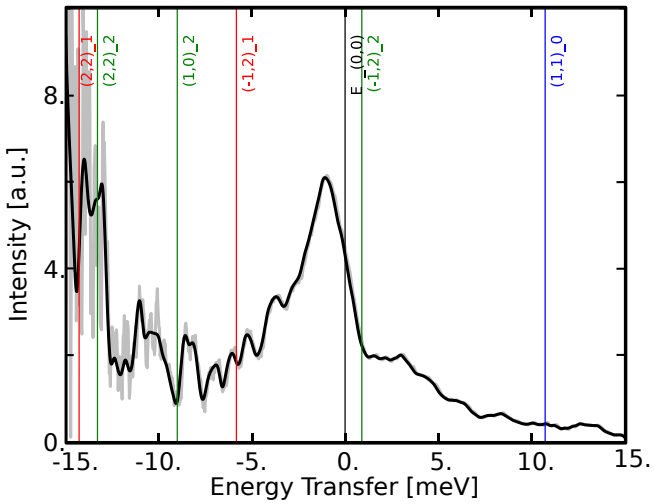

Figure 5.7: Time-of-flight (TOF) measurement of the Bi(111) surface in $\overline{\Gamma K}$ direction for $\theta_i = 44.75°$ and an incident energy of 17.79 meV. Both resonant enhancements associated with the strong $(1,0)_2$ resonance of the one-phonon peak associated with the SV3 optical mode at about -13 meV and of the multiphonon background in the one-phonon gap at about -8 meV are distinctly observed.

angle of 91.5°, an incident energy of 17.79 meV and a surface temperature of 104 K. Besides the diffused elastic peak at $\Delta E = 0$, the positions of the expected inelastic resonances are indicated on both the positive and negative energy transfer sides. The region where the phonon gap is expected (7.5 to 9.0 meV[89,90]) is actually filled by a multiphonon background, as expected for the surface temperature of this experiment. This background is however strongly enhanced around 8 meV by a peak which can be assigned to the strong $(1,0)_2$ inelastic resonance whereupon the small difference between the peak and resonance positions with an adjacent dip pointing to a possible Fano-like character of this resonance. The effect of the other resonances are more difficult to assess as they fall into regions where important and comparatively sharp one-phonon features are expected. This can only be done through a sequence of small changes of either the incident angle or energy so as to detect a rapid intensity increase (or decrease) of a given phonon peak. Nevertheless the sharp peak at ≈ 13 meV, corresponding to an optical SV3 mode, is to be considered as resonance enhanced, since no such intensity would be expected for a second bilayer (third layer) optical mode.

An analysis of the resonance enhancement effect based on a sequence of slightly different incident angles and a fixed incident energy is shown in Fig. 5.8 for the optical phonon region. Ten spectra for θ_i varying from 51.35° to 55.85° along the $\overline{\Gamma M}$ direction are shown in Fig. 5.8(a) with indication of the main surface phonon peaks and of the

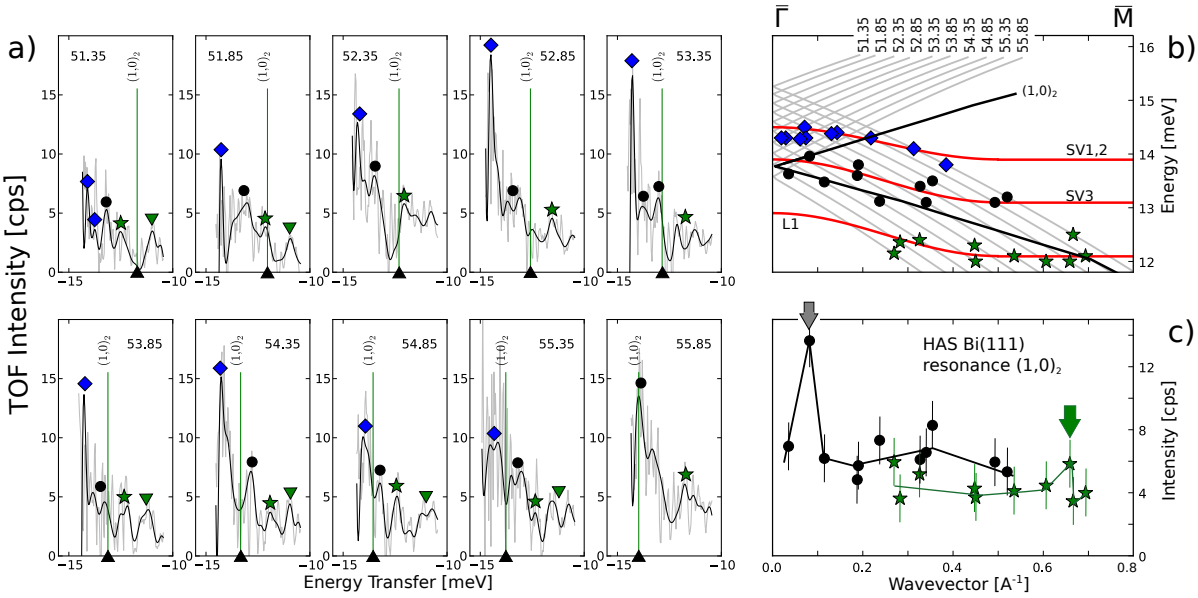

Figure 5.8: Resonant enhancement of the optical SV3 and L1 modes. (a): Ten slices from the time-of-flight measurements indicated by the dotted scan curves in (b). Diamond, circle, star and inverted triangles indicate the measured positions of possible phonons. The black triangle indicates the position of the $(1,0)_2$ final-state inelastic resonance. The downward triangle modes correspond to the flat optical L3 branch at 11.3 meV[90]. (b) Measured phonon positions with the respective scan curves and the position of the $(1,0)_2$ resonance for the given experimental conditions. (c) Total intensities of all the measured points that were considered to correspond to the SV3 or the L1 mode, plotted as functions of the corresponding parallel wavevectors. The largest $(1,0)_2$ resonance enhancements are marked by arrows.

position of the $(1,0)_2$ resonance for the $n = 2$ bound state and $\mathbf{G} = (1,0)$. The resonance condition, Eq. 5.4, is represented by a broken line in Fig. 5.8(b), superimposed to the set of scan curves for the ten incident angles. Note that the curves have all been folded into the first SBZ, so that the significant intersections are only those where the resonance and scan curves have concordant slopes. The positions of the phonons labelled in Fig. 5.8(a) are indicated on the corresponding scan curves with the same symbols. The comparison with the dispersion curves of the SV1, SV3 and L1 branches calculated with DFPT without spin-orbit coupling (SOC)[89,90] shows that the theoretical branches should be somewhat softer at small wave-vectors for a better agreement with experiment. This softening is expected when SOC is included; actually a larger softening is found for DFPT calculations with SOC included[20,44] for free-standing slabs up to 5 bilayers thick. It is however difficult to infer from ultrathin free-standing slab calculations the precise phonon energies for the semi-infinite crystal. Considering the non-trivial aspects of ab-initio calculations for the 6sp metals and the neglecting of van der Waals interaction, both the above calculations are to be considered in satisfactory agreement with experiment, while confirming the softening effect of SOC.
By considering now the resonance condition curve, it appears that the experimental points which fall atop or close to it have the largest intensity as appears from the plots of Fig. 5.8(c). In practice the theoretical SV3 branch, once it is slightly softened so as to best fit the corresponding set of experimental points, would run very close to the resonance curve along a good portion of the SBZ and would therefore benefit from the resonance enhancement. As anticipated in the introduction, the situation of tangency between a phonon dispersion curve and a resonance curve corresponds to the surfing condition, in which the atom trapped in the bound states and the phonon created in the phonon-assisted selective adsorption process run together with the same group velocity[10], which ensures a strong enhancement of the iHAS intensity.
In principle, the surfing conditions can be met by tuning the energy and angle of the incident He beam, provided one has a preliminary qualitative knowledge on the expected position of the phonon dispersion curves.

5.6 Conclusion

The growing interest in the surface properties of semimetals, especially those which exhibit a topological insulator behavior, and the recent demonstration that inelastic He atom scattering from conducting surfaces can provide direct information on mode-selected electron-phonon coupling have motivated the present investigation on the He-Bi(111) interaction potential by means of helium atom scattering. The surface corrugation of the Bi(111) surface, not expected for metal surfaces but well justified for

semimetals due to the existence of surface electron pocket states at the Fermi level, allowed for the observation of bound state resonances and the corresponding surface potential profile. Three bound state levels have been identified with binding energies of 6.18, 3.49 and 1.42 meV. For a corrugated surface the knowledge of bound state energies is a necessary ingredient for a detailed study of the surface phonon dispersion curves and the corresponding electron-phonon coupling strengths (mode-lambdas). On one side the inelastic HAS amplitudes providing the mode-lambdas should not be altered by undesired bound-state resonances. On the other side bound-state resonances can be tuned in order to enhance the inelastic HAS intensities from the optical surface modes, which are normally weak. The optical surface phonon modes in a related topological insulator like Bi_2Se_3 have been recently investigated by HAS and shown to have conspicuous anomalies attributed to the electron-phonon interaction with the Dirac-cone fermions[103,104]. A quantitative interpretation of these data requires however a careful assessment of the He-surface potential along the lines indicated in the present HAS study of the Bi(111) surface.

The profile of the atom-surface potential in the direction normal to the surface as determined from the energies of bound states, and specifically the potential depth D, together with the knowledge of the surface corrugation provide a complete picture of the interaction potential[40], which is a useful information in a variety of other applications. We note, for example, that corrugated conducting surfaces like those of semimetals allow for the selective adsorption, either elastic or inelastic, also of chemical species more interesting than the inert He atoms. In general, the selective adsorption of gas species into a surface bound state can provide a precursor state for surface reactions and may have a paramount importance in the characterization of heterogeneous catalysis.

6 The Helium-Surface Interaction Potential of Sb(111) from Scattering Experiments and Close-Coupling Calculations

The present chapter serves as a summary of a publication by M. Mayrhofer-Reinhartshuber, Patrick Kraus, Anton Tamtögl, Salvador Miret-Artés and Wolfgang E. Ernst in *Physical Review B* under the same title[69]. The summary of this publication is included in this thesis since it represents the first application of the CC-formalism on the present structures. It therefore contains several figures and tables previously published in[69].

During the course of this work selective adsorption resonance feature positions in angular He-Sb(111) diffraction spectra are analyzed to obtain fitted potential parameters for the surface averaged interaction potential. The same procedure has been applied in investigations of the He-Bi(111) interaction featured in this thesis in Chapter 5. The angular spectrum used is depicted in Figure 6.1. The analysis of these resonance positions and the subsequent fit to a 9-3 potential (see equation. 3.35) yields the bound state energy values listed in Table 6.1. The found bound state energies were furthermore used to determine fit parameters for a surface averaged corrugated Morse (CMP) and a hybrid Morse potential (HMP) (see equations 3.36, 7.10, 7.12) Those parameters are

Table 6.1: Bound-state energies experimentally determined from HAS measurements and analytically calculated for the fitted 9-3 He-Sb(111) interaction potential with $D = (4.41 \pm 0.09)$ meV and $\sigma = (6.3 \pm 0.3)$ Å.

Bound State	Experiment Energy (meV)	9-3 Potential Energy (meV)
E_0	-3.7 ± 0.2	-3.7 ± 0.1
E_1	-2.6 ± 0.2	-2.6 ± 0.2
E_2	-1.86 ± 0.02	-1.8 ± 0.2
E_3	-1.17 ± 0.02	-1.2 ± 0.1
E_4	-0.70 ± 0.02	-0.8 ± 0.1

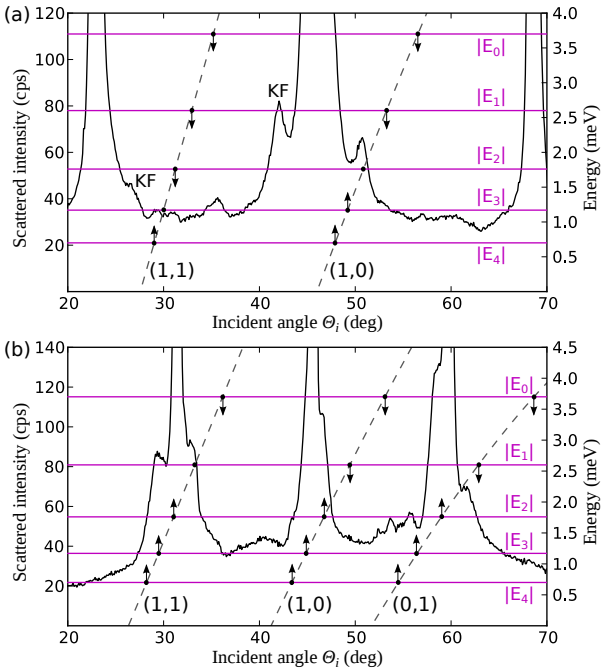

Figure 6.1: (a): Angular distribution of the HAS intensity (left-hand ordinate scale) from Sb(111) along the $\overline{\Gamma K}$ surface direction at a beam energy of 15 meV. In addition to the specular peak (45.75°) and the two closest Bragg peaks, further features corresponding to selective adsorption processes are identifiable. The five bound-state energies, that were found with our measurements, are depicted as horizontal lines (right-hand ordinate scale). The two dashed lines correspond to the resonance conditions for two **G** vectors [(1,0), (1,1)] in our experimental geometry and are labeled accordingly. Two additional peaks are attributed to kinematic focusing (KF) effects[69]
(b): Same as (a) for an angular scan along the $\overline{\Gamma M}$ direction with resonance conditions for three **G** vectors [(1,0), (0,1), (1,1)].

Table 6.2: Fitted potential parameters (well depth D, stiffness parameter χ, and inflection point z_p) for the Morse- as well as the Hybrid (Morse/9-3) He-Sb(111) interaction potential.

Type	D (meV)	χ (Å^{-1})	z_p (Å)
CMP	4.196	0.380	–
HMP	4.252	0.395	3.0

Table 6.3: Bound-state energies experimentally determined from HAS measurements and calculated analytically for the CMP and numerically for the HMP.

Bound State	Experiment Energy (meV)	CMP Energy (meV)	HMP Energy (meV)
E_0	−3.7	−3.7	−3.7
E_1	−2.6	−2.7	−2.7
E_2	−1.86	−1.82	−1.82
E_3	−1.17	−1.13	−1.17
E_4	−0.70	−0.60	−0.72
σ_E	–	0.03	0.02

listed in table 6.2, the corresponding calculated bound state energies in table 6.3, while the listed σ-value states the mean quadratic deviation of the calculated bound state energies from the measured values as defined by

$$\sigma_\mathrm{E} \;=\; \frac{1}{N}\sqrt{\sum_{i=1}^{N}\left|\epsilon_i^{\mathrm{exp}}-\epsilon_i^{\mathrm{pot}}\right|^2}, \tag{6.1}$$

with $\epsilon_i^{\mathrm{exp}}$ and $\epsilon_i^{\mathrm{pot}}$ being the experimental and the calculated bound state energies respectively, and N the number of bound states included.

The corresponding σ_E value for the fitted 9-3 potential is 0.024, so perfectly in-between the CMP and the HMP. While these two potentials thus provide no benefit compared to the 9-3-potential, the close-coupling formalism has been derived for the CMP and consequences of a severe alteration of the central interaction potential shape were unknown and first investigated in subsequent publications[53] that are included in this thesis in chapter 7. The thus obtained interaction potentials were utilized in fitting the surface corrugation height ξ_0 (see equation 4.1) for two different incident beam energies using the close-coupling formalism. The coupling function used was derived and published in the publication featured in chapter 7 to be

$$v_{h,k} = \frac{\sqrt{3}}{2}\frac{a^2}{\pi}\frac{1}{2}\sum_{i=-\infty}^{\infty} I_i(\alpha)[I_{i+h}(\alpha)I_{i-k}(\alpha)+I_{i-h}(\alpha)I_{i+k}(\alpha)]. \tag{6.2}$$

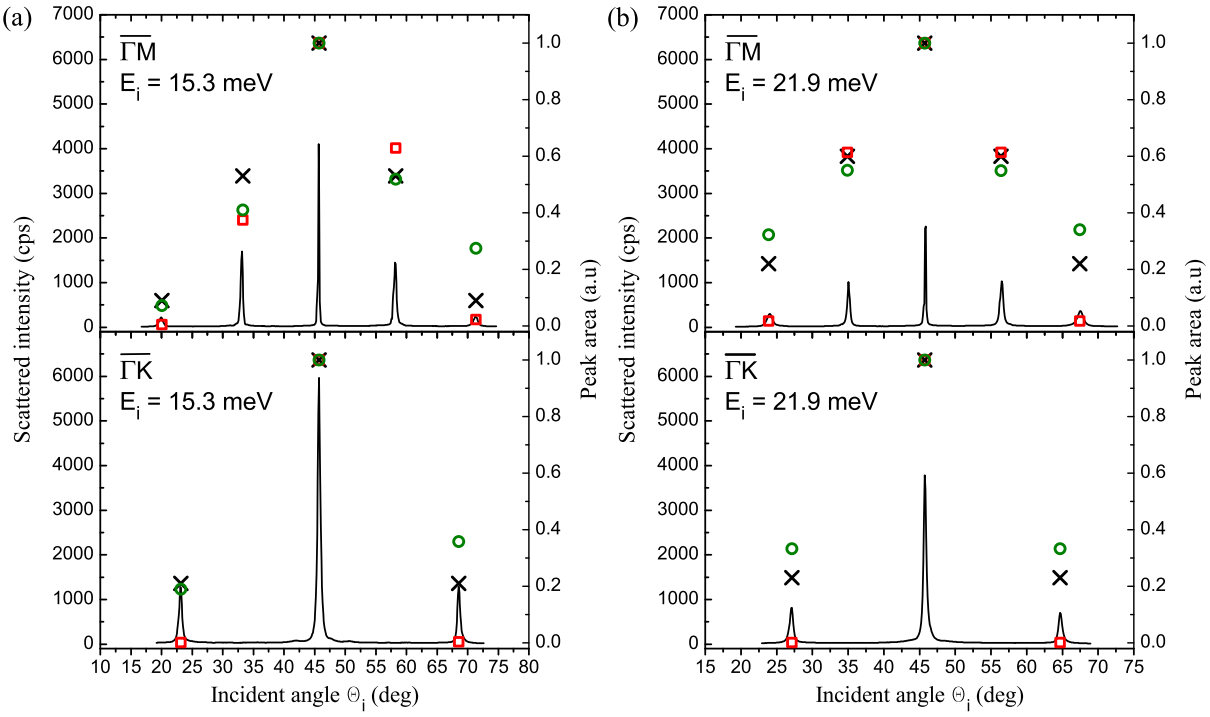

Figure 6.2: (a): Angular distributions of HAS intensity along the $\overline{\Gamma M}$ and $\overline{\Gamma K}$ surface directions at a beam energy of 15.3 meV. The peak areas (black crosses), determined from measurements (black line) are in good agreement with the best-fit results from CC calculations including the HMP [(green) circles]. Best-fit diffraction probabilities calculated with the CMP [(red) squares] show a larger deviation from the measured values. Especially when modeling the diffraction in $\overline{\Gamma K}$, the HMP is superior to the CMP.
(b): Same as (a) with a beam energy of 21.9 meV. Again, the CC results for the HMP are, in contrast to the CMP, in very good agreement with the measured values.

Table 6.4: Results of the CC calculations for the CMP and HMP at different incident energies E_i. Peak-to-peak values ξ_pp are given for the obtained corrugation function, equation (4.1), as well as the effective corrugation function, (6.3), relative to the lattice constant a. The R-value quanifies the deviation of the calculated intensities from the experimental ones and is defined by equation 7.29 in section 7.

Type	E_i (meV)	ξ_pp (Å)	R (%)	ξ_pp/a (%)	$\xi_{\mathrm{E_i,pp}}/a$ (%)
CMP	15.3	0.59	6.1	13.7	9.5
CMP	21.9	0.63	7.2	14.6	9.8
HMP	15.3	0.76	4.5	17.7	12.4
HMP	21.9	0.74	3.8	17.1	11.5

Due to the fixed-angle geometry, the measured intensities correspond to different incident angles. These angular variations cause each helium atom to encounter a different potential when traveling through the three-dimensional electronic density. When defining the classical turning points as the *effective corrugation function*[74], it can be derived via

$$\xi_{E_\mathrm{i}}(\mathbf{R}) = \frac{1}{\chi}\ln\left[-\frac{D}{E_\mathrm{i}} + \sqrt{\frac{D^2}{E_\mathrm{i}^2} + \frac{D}{E_\mathrm{i}}\left(1 + \sum_{\mathbf{G}\neq 0}\frac{\nu_\mathbf{G}}{\nu_0}e^{i\mathbf{G}\cdot\mathbf{R}}\right)}\right]. \tag{6.3}$$

The resulting peak-to-peak corrugation values as well as the effective corrugation values are listed in Table 6.4. The corresponding predicted scattering intensities are depicted in Figure 6.2. Despite slight asymmetries in the lower-energy calculation, both interaction potentials seem to reproduce the observed first-order diffraction peaks in $\overline{\Gamma\mathrm{M}}$ direction. The corresponding second order intensities as well as the scattering intensities in $\overline{\Gamma\mathrm{K}}$ direction however, are not described by the CMP. Since the only mentionable change in the potential shape is the modified attractive behavior, the researchers conclude that those intensities are especially sensitive to the attractive particle-surface interaction. The HMP in both cases describes the observed scattering intensities well. The identified corrugation parameters were furthermore used to locate resonance effects in the temperature-dependent specular HAS intensity. Using the fitted values, a simulated spectrum was calculated and convoluted with a Gaussian distribution to account for the energetic width of the incident beam. Both signals can be viewed in Figure 6.3(b). Using the calculated signal and furthermore including the helium beam temperature dependence due to the nozzle mechanism, terrace resonant scattering and a Debye-Waller-attenuation with a surface Debye temperature of 155 K, the green line in Figure 6.3(a) was determined which is in good agreement with the black-dashed experimental result.

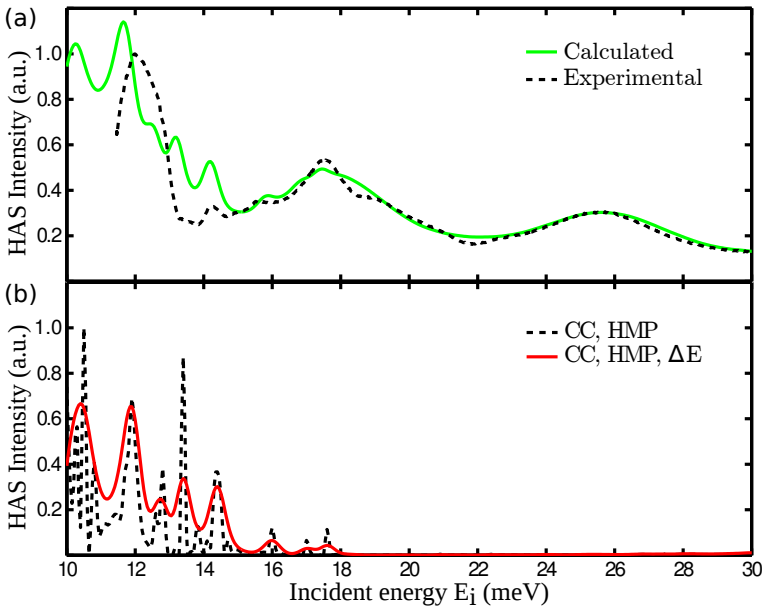

Figure 6.3: (a): Drift spectrum of the specular (0,0) peak with the sample orientated in the $\overline{\Gamma M}$-direction. The measured intensity [dashed (black) line] is plotted versus the incident energy E_i of the He beam. The simulated intensity [solid (green) line] is in good agreement with the experiment.
(b): Results from CC calculations [dashed (black) line] were convoluted with a Gaussian peak to account for the energy spread ΔE of the He beam. The signal obtained [solid (red) line] was used as the SAR contribution for the calculated intensity in (a).

7 A Comparative Study of the He-Sb(111) Interaction Potential from Close-Coupling Calculations and Helium Atom Scattering Experiments

The following corresponds to a publication by
Patrick Kraus, Michael Mayrhofer-Reinhartshuber, Christian Gösweiner, Florian Apolloner, Salvador Miret-Artés and Wolfgang E. Ernst *submitted to Surface Science*[53].

The author of this thesis was responsible for

- performing HAS measurements
- refined SAR and bound-state analysis
- implementation of the fit algorithms for the potential analysis listed in tables 7.1 and 7.2
- remodeling and rewriting of S. Miret-Artés' original CC code
- derivation of the analytical coupling parameters
- analyzing CC calculations
- implementation of the basic HAS analysis algorithms used for figures 7.2 and 7.4,

The contributions of the co-authors are listed below:

- M. Mayrhofer-Reinhartshuber: surface preparation, HAS measurements, authorship of section 7.2

- Ch. Gösweiner: performing CC calculations on the calculated potentials using the supplied code, preparation of figure 7.3.
- F. Apolloner: kinematical analysis of the supplied measurements
- S. Miret-Artés: original CC code, assisted authorship on sections 7.3 and 7.5
- W.E. Ernst: supervision (experiment, theory, publication), laboratory, funding

Abstract

The exact elastic close-coupling formalism is used to compare the performance of several interaction potentials suggested in literature for describing the measured elastic diffraction peak intensities in helium scattering experiments. The coupling parameters have been analytically calculated for the corrugated Morse potential on a hexagonal surface structure and adapted for usage with similar interaction potentials. The potentials used have been fitted to previously known bound state energies complemented by two additional levels which are found by improving energy resolution. It is established that the shifted Morse potential reproduces the experimental He-Sb(111) bound state more closely than the other considered potential shapes. The performance of several interaction potentials in describing the elastic scattering intensities is presented and discussed. Morse and Morse-related potentials provide the best compromise for the description of elastic scattering intensities. The different effects of the potential shape were determined by comparing the calculated scattering intensities.

7.1 Introduction

Recently, the surfaces of the semimetal antimony (Sb) have raised much interest. Aside from being one of the two major ingredients in the newly found class of materials of topological insulators[43,102], antimony has been observed to exhibit a large electronic surface corrugation despite the existence of free surface electronic charge carriers[70]. Since the electronic and spintronic properties of Sb(111) nanofilms have shown to be easily tunable[12,13] their surfaces prove to be excellent playgrounds for examining related effects. Helium Atom Scattering (HAS) experiments are perfectly suited for investigating surface properties. The low-energy helium atoms are already repelled from the electron density above the first layer, so HAS measurements are especially sensitive to strictly surface specific properties. The interaction potential between the helium atom and the surface plays a major role in the analysis of HAS experiments and several surface effects. Resonance features can also alter the measured scattering intensities[40] and be used to selectively enhance the signal for low-intensity phonon modes in inelastic HAS measurements, as recently reported for Bi(111)[55].

Typically, the interaction potential is assumed to have corrugated Morse shape[30] since it fundamentally simplifies the processing of data as well as fitting procedures. However, a Morse potential does not describe the correct long-range interaction behavior since it assumes the attractive part to be of an exponential shape, while theory suggests it should be proportional to $1/z^3$, with z being the distance to the surface normal. This basic discrepancy leads to the repeatedly observed inability of the corrugated Morse potential to describe second order $\overline{\Gamma M}$ or first order $\overline{\Gamma K}$ scattering on hexagonal surfaces[53,69]. To describe the complete interaction correctly, a broader scope on the overall potential shape

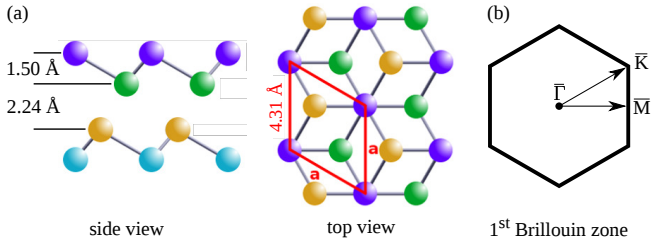

Figure 7.1: (a) Structure of the Sb(111) surface in side and top view with lattice constants as determined by Bengió et al.[11]. (b) The first Brillouin zone of the topmost layer with the two high symmetry directions.

must be given. To keep the number of potential parameters manageable and the variety of potential shapes as high as possible, a collection of previously suggested analytical potentials was applied and compared with our elastic scattering data. From the observed selective adsorption resonances, a fitting procedure of the bound states supported by the suggested potentials has been carried out. Once the potential parameters were settled for each model, close-coupling calculations[63,64,80] were performed to obtain the corresponding scattering intensities to be compared with the observed ones. In order to take into account the inelastic features of the scattering due to the surface temperature, a Debye-Waller attenuation factor is applied for the calculation of theoretical values. The main free parameters in the scattering intensities are the corrugation amplitude of the surface and the stiffness of the repulsive potential. We find that among the different sets of parameters assigned to each interaction potential analyzed and issued from the two different fitting procedures, those coming from Morse-like potentials provide us with a reliable and plausible description of the helium-surface scattering.

7.2 Antimony Surface Structure

Bulk antimony crystallizes in the rhombohedral A7 (space group R$\bar{3}$m) crystal structure[5,81]. Every atom in this structure is surrounded by three nearest and three next nearest neighbors. The main characteristic of this for pnictogens typical structure is the occurrence of puckered bilayers of atoms perpendicular to the ⟨111⟩-direction of the crystal. The bonding between the atoms within such a bilayer is of a covalent type, whereas the inter-layer bonding is weaker and of van der Waals character. Therefore, the (111) surface of Sb is easily obtained by cleaving the crystal between these bilayers.

As can be seen in figure 7.1, the atoms in the topmost layer of this surface are arranged in a hexagonal structure with a distance of $a = (4.3084 \pm 0.0002)$ Å between the atoms[11,85]. In recent studies using STM[85] and photoelectron diffraction[11], no significant relaxations with respect to the bulk structure were found. An analysis of the step height and terrace distribution with HAS revealed a quite flat shape of the clean Sb(111) sur-

face[70]. If the atoms from the second atomic layer are included, the sixfold symmetry of the first layer is reduced to a threefold symmetry. Nevertheless, within the present study, the Sb(111) surface is considered as sixfold symmetric, since the energy of the He beam during the experiments of this study was small enough to neglect the influences from lower layers with clear conscience[89,90]. Thus, with $\overline{\Gamma M}$ and $\overline{\Gamma K}$ there exist two high symmetry directions for this lattice type. Angular resolved photoemission spectroscopy was used to determine the electronic structure of Sb(111)[38,86]. Whereas bulk Sb has semimetallic character, the Fermi surface for Sb(111) shows metallic properties. At the center of the Brillouin zone an electron pocket with a hexagonal-like shape was found. This electron pocket is surrounded by six hole pockets with ellipsoidal shape[87].

7.3 The Close-Coupling Method

The Close-Coupling (CC) formalism can be used as an exact method for calculating the quantum diffraction intensities in atom-surface scattering problems. All formulas in this section are given in natural units $\frac{\hbar^2}{2m} = 1$. The impinging particle is assumed to be structureless and nonpenetrating, the surface to be statically corrugated and periodic. The time-independent Schrödinger equation for purely elastic scattering of such a particle with a wavevector of $\mathbf{k}_i$ is

$$\left[-\nabla^2 + V(\mathbf{r}) - \mathbf{k}_i^2\right] \Psi(\mathbf{r}) \;=\; 0. \tag{7.1}$$

We follow the standard notation where lower case letters are used for 3D vectors and capital letters for 2D (parallel to the surface) vectors. The z direction is perpendicular to the surface plane. Since the wavefunction and the interaction potential can be assumed to be periodic, both can be Fourier expanded. Following the integration procedure outlined in the review by Sanz et. al[80] one finally reaches a set of coupled equations which reads as

$$\left[\frac{d^2}{dz^2} + \mathbf{k}_{\mathbf{G},z}^2 - V_{00}(z)\right] \Psi_{\mathbf{G}}(z) \;=\; \sum_{\mathbf{G}\neq\mathbf{G}'} V_{\mathbf{G}-\mathbf{G}'}(z)\Psi_{\mathbf{G}'}(z) \tag{7.2}$$

with $V_{00}(z)$ the surface-averaged interaction potential and $\mathbf{k}_{\mathbf{G},z}^2$ being the z-component of the scattered particles' kinetic energy. This energy can be calculated easily by conservation of energy

$$\mathbf{k}_{\mathbf{G},z}^2 \;=\; \mathbf{k}_i^2 - (\mathbf{K}_i + \mathbf{G})^2 \,. \tag{7.3}$$

Actually, for every $\mathbf{G}$, an effective potential $V_{00}(z) + (\mathbf{K}_i + \mathbf{G})^2$ is included in Eq.(7.2), the second term being the so-called asymptotic energy (AE). This AE depends on the reciprocal lattice vector involved in this specific scattering process as well as on the incident scattering conditions (energy as well as polar and azimuthal angles). While

studying scattering processes with the CC-formalism, the term *channel* usually denotes such an effective potential and is thus labeled with the respective $\mathbf{G}(h,k)$-vector. Two types of channels have to be distinguished. Channels with a positive normal kinetic energy ($\mathbf{k}^2_{\mathbf{G},z} > 0$) are called *open*, while channels with a negative normal kinetic energy ($\mathbf{k}^2_{\mathbf{G},z} < 0$) are called *closed*. While only open scattering channels can be accessed directly, the closed channels are of essential importance in achieving numerical convergence.

The coupling parameters issued from the CC-equations are easily obtained when considering a corrugated Morse potential (CMP)[30], leading very often to simple analytical expressions. The CMP model can be written as

$$V(\mathbf{R},z) \;=\; D\left[\frac{1}{\nu_{0,0}}e^{-2\kappa[z-\xi(\mathbf{R})]} - 2e^{-\kappa z}\right] \tag{7.4}$$

where κ is the stiffness parameter, D the depth of the attractive well, $\xi(\mathbf{R})$ is the so-called corrugation function and $\nu_{0,0}$ being the surface average of the exponential of the corrugation function coming from

$$\nu_{\mathbf{G}}(z) \;=\; \frac{1}{\Sigma}\int_{\Sigma} e^{-i\mathbf{G}\cdot\mathbf{R}}e^{2\kappa\xi(\mathbf{R})}d\mathbf{R} \tag{7.5}$$

with Σ being the area of the first unit cell. From the Fourier transform of the interaction potential, one determines the zero-term of the Fourier series to be the regular Morse potential

$$V_{00}(z) \;=\; D\left[e^{-2\kappa z} - 2e^{-\kappa z}\right] \tag{7.6}$$

while the other terms, the coupling terms $V_{\mathbf{G}-\mathbf{G}'}(z)$, are expressed as

$$V_{\mathbf{G}-\mathbf{G}'}(z) \;=\; D\frac{\nu_{h,k}}{\nu_{0,0}}e^{-2\kappa z} \tag{7.7}$$

It is clear that by increasing the corrugation amplitude of the surface, the coupling factors $V_{\mathbf{G}-\mathbf{G}'}(z)$ in Eq.(7.7) will be larger and more channels have to be included to reach numerical convergence. In this model, the corrugation amplitudes are energy dependent since when the incident energy is increased, the penetration of the scattering particle into the surface is higher and higher. The computation time is known to be scaled with N^3, N being the number of total scattering channels considered[63]. The wavefunctions $\Psi_{\mathbf{G}}$ is integrated by considering the simple boundary conditions of vanishing it far in the forbidden region behind the repulsive slope and to remain mostly unchanging sinusoidal shape in the region where the attractive slope approaches zero[80]. The integration is performed using a Fox-Goodwin integrator as has been used in earlier close-coupling treatments[29,74], going from -7 Å to 25 Å with a step size corresponding to 100 steps per minimum wavelength considered, and resulting in 3285 steps. The number of channels

considered was chosen to fulfill the condition $\nu_{h,k}/\nu_{0,0} > 1 \cdot 10^{-7}$. In total, ≈ 100 open scattering channels and ≈ 150 closed ones were finally used. In our case, the surface corrugation function adapted to the geometry of the corresponding surface unit cell can be considered to be a summation of cosine functions from a Fourier expansion such as

$$\begin{aligned} \xi(x,y) &= \xi_0 \left(\cos\left[\frac{2\pi}{a}\left(x - \frac{y}{\sqrt{3}}\right)\right] \right. \\ &\left. + \cos\left[\frac{2\pi}{a}\left(x + \frac{y}{\sqrt{3}}\right)\right]\right) + \xi_0 \cos\left[\frac{2\pi}{a}\frac{2y}{\sqrt{3}}\right] + h.o., \end{aligned} \tag{7.8}$$

where ξ_0 is the corrugation amplitude and higher-order terms are omitted. After some straightforward manipulations (see Appendix), the coupling terms are reduced to a simple analytic expression to be

$$\nu_{h,k} = \frac{\sqrt{3}}{2}\frac{a^2}{\pi}\frac{1}{2}\sum_{i=-\infty}^{\infty} I_i(\alpha)\left[I_{i+h}(\alpha)I_{i-k}(\alpha) + I_{i-h}(\alpha)I_{i+k}(\alpha)\right], \tag{7.9}$$

with $I_i(\alpha)$ the modified Bessel functions and $\alpha = 2\kappa\xi_0$.

The code developed for this research is published under the BSD 3-Clause license and available under *http://iep.tugraz.at/closecoupling*

7.4 He-surface interaction potentials

To accurately describe scattering experiments, a three-dimensional interaction potential between the surface and the probe particle is needed. In spite of the fact that the true interaction potential is unknown, certain interaction models capture the main physical properties which justifies their applicability in theoretical studies. One of the main requirements is periodicity so it may be written in terms of a Fourier series. The problem can then be translated to the corresponding Fourier coefficients. An example has been discussed in the previous section. In principle, the first Fourier coefficient leading to the lateral surface averaged potential, $V_{00}(z)$ can now be discussed separately from the rest of the coupling terms. In this section, we are going to analyze several zero order coefficients in order to extract new information of the total interaction potential from the experimental results.

In the following paragraphs several model potentials are discussed based on the summary reported by Hoinkes[40]. For fitting purposes, most of the ones presented here are chosen to have analytical energy levels. Thus, the corresponding energy eigenvalues ϵ_j ($j = 0, 1, 2, ...$), $\epsilon_j < 0$ are listed if they exist. Eigenenergies without an existing analytical expression were calculated numerically following a Numerov scheme. Except for individual parameters for particular potentials, the following notation is used throughout all listed potentials: D denotes the well depth of the potential, the position of the

minimum, if different from zero, is given by z_e and the reciprocal range parameter by κ. The particle mass m refers to the helium atom mass. The z_e parameter is generally chosen such as to position the potential's minimum to $z = 0$. Naturally, these values may differ depending on the type of the used potential. The shift to zero is necessary since the coupling parameters in Equation 7.7 are calculated for the corrugated Morse potential. Any shift between the surface averaged potential and its Fourier components would lead to a severe alteration of the potential character.

The usage of potential shapes originating from summation over two-body potentials can be regarded as inaccurate for surfaces with mobile charge carriers such as semimetals at finite temperatures. However, the deviations produced by these effects mostly affect the attractive interaction since the repulsive Pauli interaction mainly originates from the core electrons. Due to the difficulties encountered when including van der Waals interactions into DFPT calculations, reasonable alterations of practical interaction potentials such as the Morse potential still seem a viable alternative to a full pertubative approach.

Morse Potential (MP)[24,58]

$$V_{00}^{\mathrm{M}}(z) = D\left[e^{-2\kappa z} - 2e^{-\kappa z}\right]. \tag{7.10}$$

$$\epsilon_j = -\left[\sqrt{D} - \frac{\hbar\kappa}{\sqrt{2m}}\left(j + \frac{1}{2}\right)\right]^2 \tag{7.11}$$

Hybrid Morse Potential (HMP)[80]

$$\begin{aligned} V_{00}^{\mathrm{HM}}(z) &= V_{00}^{\mathrm{M}}(z) \text{ for } z < z_{\mathrm{p}} \\ V_{00}^{\mathrm{HM}}(z) &= -C_3 z^{-3} \text{ for } z \geq z_{\mathrm{p}} \end{aligned} \tag{7.12}$$

where C_3 is chosen for continuity at the inflection point z_{p}. This potential improves the Morse potential since it displays the right asymptotic behavior.

Shifted Morse Potential (SMP)[23]

$$V_{00}^{\mathrm{SM}}(z) = D\left[e^{-2\kappa z} - 2e^{-\kappa z} - \Delta\right] \tag{7.13}$$

with Δ the shift parameter and a total well-depth of $D(1 + \Delta)$.

$$\epsilon_j = -D(1+\Delta) + \hbar\kappa\sqrt{\frac{2D}{m}}\left(j + \frac{1}{2}\right) - \left(\frac{\hbar^2\kappa^2}{2m}\right)\left(j + \frac{1}{2}\right)^2 \tag{7.14}$$

Shifted Morse Hybrid Potential (SMHP)[23]

$$V_{00}^{\mathrm{SMH}}(z) = V_{00}^{\mathrm{SM}}(z) \text{ for } z < z_{\mathrm{p}} \qquad (7.15)$$
$$V_{00}^{\mathrm{SMH}}(z) = -C_3 z^{-3} \text{ for } z \geq z_{\mathrm{p}}$$

where C_3 is chosen for continuity at the inflection point z_{p}.

(9-3) Potential[22]

$$V_{00}^{9-3}(z) = \frac{\sqrt{27}}{2} D \left[\left(\frac{\sigma}{(z - z_{\mathrm{e}})} \right)^9 - \left(\frac{\sigma}{(z - z_{\mathrm{e}})} \right)^3 \right] \qquad (7.16)$$

$$\epsilon_j \simeq -D \left[1 - \frac{\pi\hbar \left(j + \frac{1}{2} \right)}{3.07\sigma\sqrt{2mD}} \right]^6 \qquad (7.17)$$

(12-3) Potential[95]

$$V_{00}^{12-3}(z) = \frac{D}{3} \left[\left(\frac{\sigma}{(z - z_{\mathrm{e}})} \right)^{12} - 4 \left(\frac{\sigma}{(z - z_{\mathrm{e}})} \right)^3 \right] \qquad (7.18)$$

Exponential-3 Potential (Exp3)[21]

$$V_{00}^{\exp-3}(z) = \frac{\kappa z_0}{\kappa z_0 - 3} D \left[\frac{3}{\kappa z_0} e^{-\kappa(z - z_0 + z_{\mathrm{e}})} - \left(\frac{z_0}{z + z_{\mathrm{e}}} \right)^3 \right] \qquad (7.19)$$

Variable Exponent Potential (Var-Ex)[67]

$$V_{00}^{\mathrm{VE}}(z) = D \left[\left(1 + \frac{\kappa z}{p} \right)^{-2p} - 2 \left(1 + \frac{\kappa z}{p} \right)^{-p} \right] \qquad (7.20)$$

with the variable exponent p as a fit parameter.

$$\epsilon_j = -D \left[(1 - \frac{\delta}{A^2})^{-\frac{1}{s}} - \frac{j + \frac{1}{2}}{As} \right]^s \qquad (7.21)$$

with $\delta = \frac{1+1/p}{32p}$, $A = \frac{\sqrt{2mD}}{2\hbar\kappa}$ and $\frac{1}{s} = \frac{1}{2} - \frac{1}{4p} \cdot (3 + \frac{1}{p})$.

Typically, between three or four parameters are used in the fitting procedure to the seven experimental bound states assigned and characterized for this system. For simplicity in the CC calculations, we are going to assume that the same coupling terms are valid for all the potentials listed above. Strictly speaking, and in spite of being used previously in the literature, this procedure shows some inconsistencies, which are not expected to be dramatic for the following reason. The coupling terms are mainly describing the repulsive part originating from the repulsion of the He atom electrons and the electron density of the surface. The simplest model is a repulsive exponential function of the corrugation function which also has to be a periodic function. The CMP for example evaluates the coupling terms in exactly this way. Thus, for potentials describing the repulsive behavior as an exponential, the inconsistency is really a minor one.

7.5 Inelastic resonances. Fitting procedure

The next step in our fitting procedure is to see how the experimental bound energies are extracted. In atom-surface scattering, these values come from a careful analysis of the so-called selective adsorption resonances (SARs). An SAR feature is observed when the probe particle is scattered into a bound state of the particle-surface potential. When due to a subsequent scattering process this particle leaves the surface, only a phasefactor distinguishes it from an otherwise non-resonantly scattered particle. Since the wavefunctions are otherwise indistinguishable, they interfere and produce pronounced peaks and dips in the measured intensity. An SAR can be viewed as a temporary elastic or inelastic trapping of the impinging particle along a transient bound state of the particle-surface interaction potential. The initial scattering conditions of energy and angles determine essentially where and how the SAR feature is detected. While purely elastic interaction results in variations of the elastic scattering peak heights, inelastic contributions may vary the background intensity in between those peaks[70]. Additionally, inelastic SAR features can show up as variations in the time-of-flight (TOF) intensity leading to, in some cases deliberately, enhanced phonon modes[55]. For a detailed description of SAR features see Ref.[40,55,70,80]. Within the last few years, SARs have been used to determine the bound state energies of the He-Bi(111)[55] as well as the He-Sb(111)[70] surface-averaged interaction potential. In a previous work, angular HAS measurements have been used to determine the lowest five bound state energies (BSE) of the He-Sb(111) surface-averaged interaction potential[69]. A more careful analysis of recent angular scans and time-of-flight (TOF) measurements consistently revealed additional features which led to the finding of two additional BSEs. Figure 7.2 displays exemplary angular spectra. The careful evaluation leads to a substantial improvement of the energetic uncertainty of all the observed levels.

In angular scattering spectra or angular distributions as presented in figure 7.2, the observed resonance positions can be related to the respective bound state energy via the simple energy conservation rule

$$\mathbf{k}_i \;=\; (\mathbf{k}_i \cdot sin(\theta_i) \;+\; \mathbf{G}_{\parallel})^2 \;+\; \mathbf{G}_{\perp}^2 \;-\; |\epsilon_n|, \tag{7.22}$$

with θ_i the angle of the incoming He beam with respect to the surface normal and $\mathbf{G}_{\parallel}$ and $\mathbf{G}_{\perp}$ the projections of the interacting reciprocal lattice vector parallel and perpendicular to the respective plane of incidence. By choosing scattering conditions such that the slope of the $\epsilon = f(\theta_i, \phi_i)$ function with respect to θ_i is small, high accuracy can be achieved in measuring the bound state energies.

The observed features, as depicted in Figure 7.2, have been fitted using a simple Gaussian function, since the original Lorentzian shape of the resonance feature is distorted during the measurement by the apparative broadening of the beam. The measured features are furthermore the convolution of the resonance feature with the energetic profile of the He beam as well as with the apparative broadening. Since the latter is unfortunately unknown for this apparatus, only the former is considered. The energetic width of the He beam has been mentioned in previous publications[91] as $\Delta E/E \approx 2\%$. As can be easily determined by analytical convolution of two Gaussian functions f and g, the width of the convoluted signal can be calculated as

$$\sigma_{f \otimes g} \;=\; \sqrt{\sigma_f^2 \;+\; \sigma_g^2}, \tag{7.23}$$

or- in the other direction, the width of the resonance feature σ_r can be deconvoluted from the signal width σ_s via the energetic width of the incoming He beam σ_B:

$$\sigma_r \;=\; \sqrt{\sigma_s^2 \;-\; \sigma_B^2} \tag{7.24}$$

The values for the widths of the Gaussians produced by this method are listed in the second column of Tab. 7.1. The angular position of the resonance effects in measurements at finite temperatures experiences a slight shift compared to the straightforward elastic calculation. This effect occurs due to the fundamental difference between scattering from an idealized surface averaged interaction potential (equation 7.22) and scattering on a dynamic periodic surface, where inelastic interactions may shift the otherwise elastic interaction channels[80].

Due to the additional information, the fitted potential parameters given in previous work[69] have been revised. The considered interaction potentials did not seem to be able to describe the energetic separations in between the bound states satisfactorily. Furthermore, the fitting of the potential parameters relied on a relative distance between the calculated and the measured bound state energy values that did not depend on the relative uncertainty of the measured values. Extending our considerations onto a wider

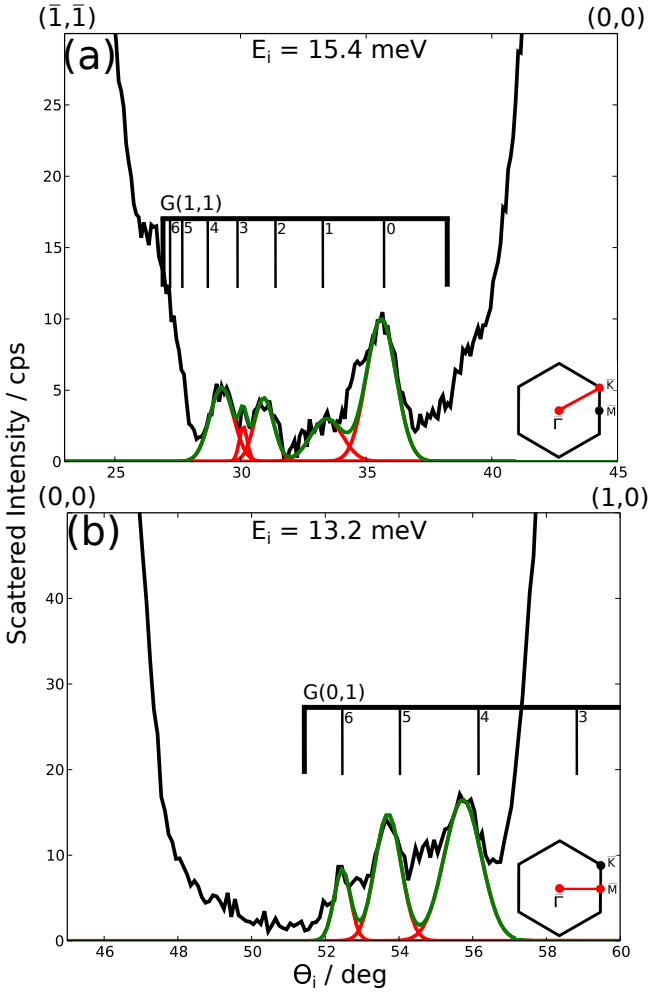

Figure 7.2: Selection of two measurements with visible SAR line shapes from all bound state levels. (a) Slice of an angular spectrum in $\overline{\Gamma K}$ direction. Bound state interactions with $(1,1)_0$ to $(1,1)_4$ lead to a significant increase in the background intensity between the specular and the first order diffraction peak. (b) Slice of an angular spectrum in $\overline{\Gamma M}$ direction. Bound state interactions with $(0,1)_4$ to $(0,1)_6$ are clearly resolved around the first order diffraction peak. The large angle between the scan direction and the interacting **G**-vector leads to a large angular spread despite a small energetic distance between the levels. The predicted resonance positions indicated by the black lines were calculated using only the surface averaged interaction potential and serve only as an indication of the approximate resonance position. Hence, coupling to additional elastic and inelastic channels will shift the observed resonance position[80].

variety of interaction potentials, which are listed in Section 7.4, allows a more detailed view on the applicability for each interaction potential. Table 7.1 lists the fitted bound state energy values for each considered potential as well as the measured BSEs already known[69] complemented with the two newly found values. The last line in Table 7.1 denotes the quality of the fitted energy values in comparison to the measured ones and is defined by

$$\sigma_{\mathrm{E}} \;=\; \frac{1}{7}\sum_{n=0}^{6} e^{1-p(E,E_n,\sigma_n)}. \tag{7.25}$$

with $p(E, E_n, \sigma_n)$ the commonly known Gaussian distribution with maximum value 1,

$$p(E, E_n, \sigma_n) \;=\; e^{-\frac{(E-E_n)^2}{2\sigma_n^2}}. \tag{7.26}$$

Here, E, E_n and σ_n signify the calculated and the measured bound state energy value and the corresponding width, respectively. Using the expression in Eq. 7.25 the deviation of the calculated energy values from the measured values is weighed by the experimental uncertainty for each level separately. The so obtained value σ_E represents the quality of the respective potential to reproduce the measured values. Smaller values of σ_E correspond to better agreement, with $\sigma_E = 1$ indicating perfect correspondence. The parameter fit was performed using a least-squares algorithm changing the potential parameters and minimizing the quality parameter σ_E. Finally, table 7.2 lists the obtained parameters for each potential. The bound states of potentials were calculated using the analytical expression where available. Figure 7.3 furthermore depicts the fitted shapes of the interaction potentials.

According to Table I, with the exceptions of the 9-3 and 12-3 potentials, which do not seem to reproduce the measured values, the rest of the model potentials provide quite reasonable values of bound states. Moreover, the shifted-Morse potential performs better than the other Morse-like potentials. These potentials were subsequently used in an extensive close-coupling analysis of the Sb(111) surface.

7.6 Close coupling results

As mentioned in Section 7.3, the coupling parameters in Eq.(7.9) have been derived for a corrugated Morse potential. However, the only potential dependent parameter entering the equation is the potential stiffness κ. Since the coupling parameters are mainly dominated by the repulsive interaction with the surface[34,48,74], the repulsive part of each suggested interaction potential was fitted with a simple Morse function to obtain an equivalent stiffness parameter κ_r. The so obtained respective κ_r value is listed in the last column of Table 7.2. This parameter, while being of no special interest to the potential itself, provides the CC calculation with coupling factors that would be produced

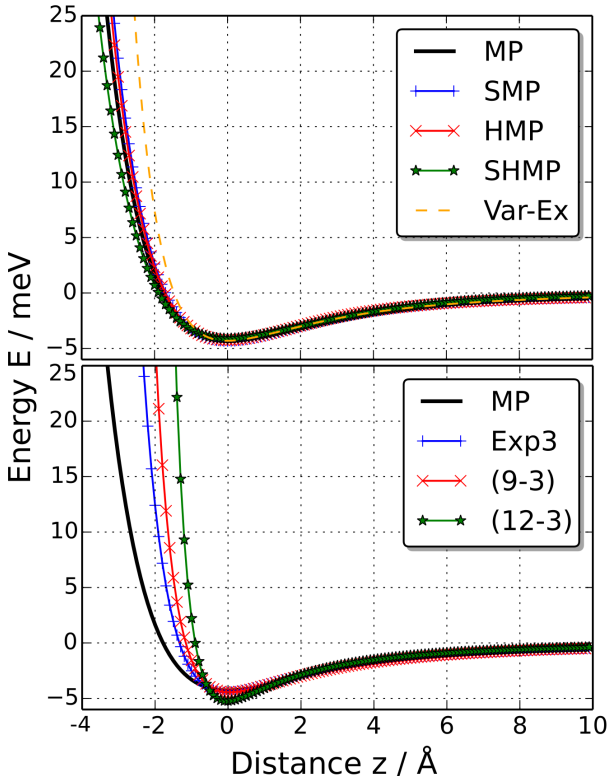

Figure 7.3: Plot of the interaction potential shapes resulting from the fitting procedure described in section 7.5 and listed in table 7.2. The upper panel depicts the Morse-like interaction potentials, while the lower panel contains the fundamentally different shapes compared to the Morse potential. Both panels contain the plain Morse interaction potential (solid black line) for comparison.

by a Morse potential with an equal repulsive slope. The potential shape itself enters the CC calculation as $V_{00}(z)$ in Eq.(7.2). This way the scattering intensities using interaction potentials different from the Morse potential may be approximated and evaluated. Naturally, the closer the original shape of the observed potential is to a simple Morse behavior, the more accurate this procedure will reproduce the scattering intensities in close-coupling calculations. As can be deducted from the Table 7.2 alone, the scattering behavior calculated for the (9-3) and (12-3) potentials should differ significantly from the others since their calculated κ_r value differs significantly from both the original κ parameter of the Morse potential and the other fitted κ_r values.

Table 7.1: Bound-state energies experimentally determined from HAS measurements and calculated analytically for the considered potential shapes. All energy values are given in meV.

Bound State	Experiment[69]	σ_r / meV	MP eq.(7.10)	HMP eq.(7.12)	SMP eq.(7.13)	SMHP eq.(7.15)	(9-3) eq.(7.16)	(12-3) eq.(7.18)	Exp3 eq.(7.19)	Var-Ex eq.(7.20)
E_0	-3.7	0.1276	-3.71	-3.68	-3.74	-3.59	-3.72	-4.16	-3.73	-3.68
E_1	-2.6	0.1503	-2.71	-2.65	-2.71	-2.65	-2.56	-2.60	-2.57	-2.62
E_2	-1.863	0.0072	-1.86	-1.79	-1.86	-1.86	-1.71	-1.58	-1.71	-1.79
E_3	-1.171	0.0067	-1.17	-1.15	-1.19	-1.21	-1.11	-0.93	-1.10	-1.16
E_4	-0.700	0.0062	-0.64	-0.70	-0.69	-0.70	-0.69	-0.52	-0.69	-0.71
E_5	-0.395	0.0086	-0.27	-0.40	-0.39	-0.37	-0.42	-0.27	-0.40	-0.39
E_6	-0.150	0.0006	-0.06	-0.22	-0.27	-0.19	-0.24	-0.05	-0.15	-0.18
σ_{E}	–	–	1.773	1.759	1.533	1.769	1.988	2.472	1.674	1.625

Table 7.2: Fitted potential parameters for the potentials listed in Section 7.4.

Potential	D / meV	κ / Å^{-1}	z_p / Å	Δ	σ / Å	z_0 / Å	p	κ_r / Å^{-1}
MP eq.(7.10)	4.275	0.389	-	-	-	-	-	-
HMP eq.(7.12)	4.263	0.404	2.899	-	-	-	-	-
SMP eq.(7.13)	4.336	0.418	-	0.066	-	-	-	0.409
SMHP eq.(7.15)	4.358	0.367	6.625	0.061	-	-	-	0.367
(9-3) eq.(7.16)	4.454	-	-	-	5.941	-	-	0.624
(12-3) eq.(7.18)	5.225	-	-	-	6.065	-	-	0.848
Exp3 eq.(7.19)	4.445	1.376	-	-	-	7.168	-	0.539
Var-Ex eq.(7.20)	4.313	0.438	-	-	-	-	4.495	0.493

Table 7.3: Best peak-to-peak corrugation values ξ_0 with respect to the interatomic distance found for each potential for a scattering energy of $E_i = 21.9$ meV using a modified elastic CC-calculation.

Potential	ξ_{pp} / %	R / %
MP eq.(7.10)	13.65	5.23
HMP eq.(7.12)	14.69	7.27
SMP eq.(7.13)	14.69	6.45
SMHP eq.(7.15)	15.15	4.86
(9-3) eq.(7.16)	16.79	2.24
(12-3) eq.(7.18)	18.45	10.9
Exp3 eq.(7.19)	16.35	4.74
Var-Ex eq.(7.20)	19.05	7.84

To account for inelastic effects at a surface temperature of $T_S = 298$ K, the calculated intensities were attenuated using

$$I_G^{calc}(T_S) = e^{-2W(T_S)} P_G^{calc}, \tag{7.27}$$

where $2W$ denotes the corresponding Debye-Waller factor,

$$2W = \frac{3\hbar^2 T_S (k_{iz} + k_{fz})^2}{M k_B \Theta_D^2}. \tag{7.28}$$

Here, M denotes the mass of the surface atom, $\hbar$ the reduced Planck constant, k_B the Boltzmann constant, k_{iz} and k_{fz} surface perpendicular components of the incident and final (outgoing) wavevectors and $\Theta_D = 155$ K is the surface Debye Temperature determined by Tamtögl et. al.[92].

Table 7.3 lists the best peak-to-peak corrugation values found for the several potential types as % of the interatomic distance. The R value for each corrugation is defined as a mean-square deviation from the measured intensities

$$R = \frac{1}{N} \sqrt{\sum_G (P_G^{exp} - I_G^{calc})^2}. \tag{7.29}$$

Figure 7.4 presents calculated elastic scattering intensities for selected interaction potentials in comparison to the integrated experimental peak areas. The associated deviations for all the potentials are also listed in Table 7.3.

As already observed in earlier CC-studies, the plain Morse potential (red circles) fails in describing the first-order $\overline{\Gamma K}$ as well as the second order $\overline{\Gamma M}$ peaks[69]. This fact seems to be to some degree dependent on the incorrect exponential shape of the attractive part of the interaction, since all the other potentials at least expect some intensity at those positions. Another mentionable point is the very small but nearly uniform distribution of scattering intensities in the $\overline{\Gamma M}$ direction for the 12-3 potential. While describing the character of the attractive slope correctly, the repulsive interaction is assumed much steeper (see Tab. 7.2), producing numerically higher coupling constants between the channels (see Eq. 7.9). This necessarily leads to a more uniform distribution of scattering intensities among the considered scattering channels. Only the SHMP seems to combine the accurate description of the repulsive interaction with the correct character of the attractive slope, thus producing dominant $\overline{\Gamma M}$ first-order peaks, while also generating comparable $\overline{\Gamma M}$ second-order and $\overline{\Gamma K}$ first-order peaks.

The applied interaction model does not consider the penetration depth differences for helium atoms impinging at different incident angles or incident energies. A previous analysis of the Sb(111) corrugation[69] concluded that higher incident beam energies lead to higher measured effective corrugations since the helium atom can penetrate deeper into the surface electron density, where the high electron density around the lattice

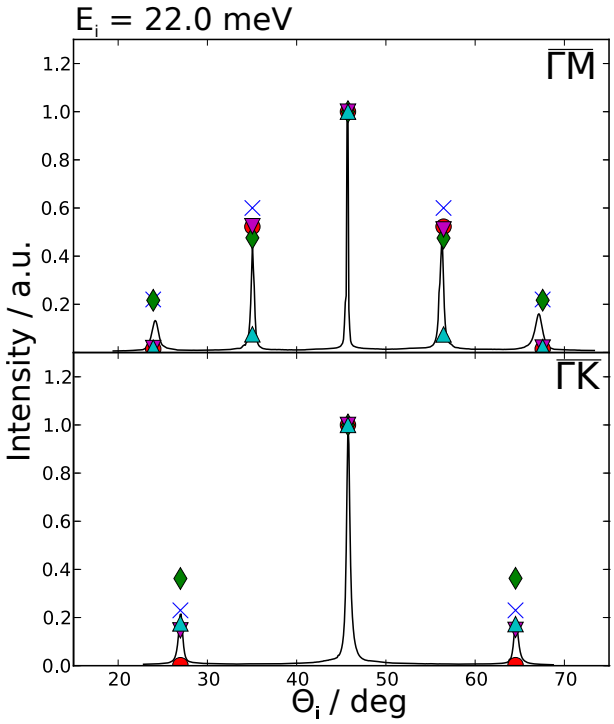

Figure 7.4: Comparison between measured and calculated scattering intensities using various interaction potentials at a surface temperature of 300 K. Blue crosses signify integrated measured peak areas, red circles, green diamonds, magenta downward triangles and cyan upward triangles signify the Morse, Shifted Hybrid Morse, 9-3 and 12-3 potentials, respectively. The potentials were chosen for reasons explained in section 7.6 and were normalized to the respective specular contributions. The calculated intensities have been attenuated using a Debye-Waller Factor and a surface Debye Temperature of $\Theta_D = 155$ K.

atoms is more dominant. Including higher corrugations enlarges the number of necessary scattering channels to reach convergence. For the analysis of the effect of varying interaction potentials, only one incident energy was chosen since the additional effect of different beam energies has been determined before and was beyond the scope of this work.

7.7 Conclusion

The comparison between calculated and measured diffraction intensities reveals a wide range of possible peak-to-peak corrugation heights, dependent on the interaction potential used. The intensities calculated with the Morse-like potentials display a mostly constant performance and converge at corrugation heights of 14-17%. This corresponds very well with the earlier obtained values of 14% and 17% for the Morse and the Hybrid Morse potential[69]. Regarding figure 7.3 and table 7.3 a general correspondence between unusually high corrugation values and high repulsive slopes of the interaction potential is found. This correlation might originate from the slope-dependent range of the coupling terms Eq. 7.7. As discussed in earlier publications on the subject[34,48,74], the dependence of the diffraction intensities is dominated by the potential stiffness parameter. Steeper repulsive potentials can be correlated with faster decreasing elastic coupling terms. The spacial range where scattering interaction might occur is therefor shortened and the calculation needs higher corrugations to explain the respectively high intensity transition to the scattering channels.
More details about the 'best' interaction potential can only be uniquely determined from a fit involving a larger parameter space for the involved potential shape, omitting the limitation of using analytical interaction potential functions. Extending the view onto interaction potentials determined from density-functional theory, as has been done by Martínez-Casado for the He-MgO(100) interaction potential[62,65], bears the potential of reaching a full description of the scattering process and thus a complete understanding of the dynamic scattering interaction. Nevertheless, we believe that our result of the Shifted-Hybrid-Morse-potential being the best compromise will help in the corrugation analysis of future scattering experiments. Given the fact that interaction potentials lacking the correct long-range interaction shape are not able to describe higher-order scattering intensities at all should emphasize the importance of the attractive interaction between the scattered particle and the substrate. Regarding the challenges theorists are facing in describing the van der Waals interaction correctly in density-functional theory calculations, CC calculations of experimental scattering spectra provide a sensitive tool for determining the quality of the attractive interaction range.

Appendix: Calculation of the coupling parameters

From Eqs. (7.5) and (7.8), the $\nu_{n,m}$ coefficients read as follows

$$\nu_{n,m} = \frac{1}{A}\int_{-\frac{a}{2}}^{\frac{a}{2}} dx \int_{-\frac{\sqrt{3}}{2}a}^{\frac{\sqrt{3}}{2}a} dy\, e^{-i\omega_0(n+m)x} e^{-i\frac{\omega_0}{\sqrt{3}}(n-m)y} e^{\alpha\cos\left(\frac{2\omega_0}{\sqrt{3}}y\right)} e^{\alpha\cos\left(\omega_0\left(x+\frac{y}{\sqrt{3}}\right)\right)} e^{\alpha\cos\left(\omega_0\left(x-\frac{y}{\sqrt{3}}\right)\right)} \tag{7.30}$$

with $\omega_0 = \frac{2\pi}{a}$, $\alpha = 2\kappa\xi_0$ and $\mathbf{G} = n\cdot\mathbf{G_1} + m\cdot\mathbf{G_2}$. The value A is the area of the surface the integration is performed on, in this case the surface unit cell. This area is the same for all the integrals calculated and cancels in Eq.(7.7). Thus it will be ignored for the rest of the calculation. The primitive reciprocal lattice vectors $\mathbf{G_1}$ and $\mathbf{G_2}$ are chosen to enclose an angle of 60° symmetric with respect to the x-axis. Next, the dependencies are split

$$\nu_{n,m} = \int_{-\frac{a}{2}}^{\frac{a}{2}} dx\; e^{-i\omega_0(n+m)x} \int_{-\frac{\sqrt{3}}{2}a}^{\frac{\sqrt{3}}{2}a} dy\; e^{-i\frac{\omega_0}{\sqrt{3}}(n-m)y} e^{\alpha\cos\left(\frac{2\omega_0}{\sqrt{3}}y\right)} e^{2\alpha\cos(\omega_0 x)\cos\left(\frac{\omega_0}{\sqrt{3}}y\right)} \tag{7.31}$$

and expand the trigonometric-exponentials into a sum of modified Bessel functions

$$\begin{aligned}\nu_{n,m} = &\int_{-\frac{a}{2}}^{\frac{a}{2}} dx\; e^{-i\omega_0(n+m)x} \int_{-\frac{\sqrt{3}}{2}a}^{\frac{\sqrt{3}}{2}a} dy\; e^{-i\frac{\omega_0}{\sqrt{3}}(n-m)y} \cdot \ldots \\ &\ldots \cdot \sum_{k=-\infty}^{\infty} I_k(\alpha)\cos\left(\frac{2\omega_0}{\sqrt{3}}ky\right) \sum_{l=-\infty}^{\infty} I_l\left(2\alpha\cos\left(\omega_0 x\right)\right)\cos\left(\frac{\omega_0}{\sqrt{3}}ly\right).\end{aligned} \tag{7.32}$$

For the next step, this equation can be further separated into

$$\begin{aligned}\nu_{n,m} = &\sum_{k=-\infty}^{\infty}\sum_{l=-\infty}^{\infty} I_k(\alpha) \int_{-\frac{a}{2}}^{\frac{a}{2}} dx\; e^{-i\omega_0(n+m)x} I_l\left(2\alpha\cos\left(\omega_0 x\right)\right)\cdot\ldots \\ &\ldots\cdot \int_{-\frac{\sqrt{3}}{2}a}^{\frac{\sqrt{3}}{2}a} dy\; e^{-i\frac{\omega_0}{\sqrt{3}}(n-m)y} \cos\left(\frac{2\omega_0}{\sqrt{3}}ky\right)\cos\left(\frac{\omega_0}{\sqrt{3}}ly\right).\end{aligned} \tag{7.33}$$

For the integral in y one easily obtains

$$\frac{\sqrt{3}}{2}\frac{a}{\pi}\frac{1}{4}\left[\delta\left(l,-2k-(m-n)\right)+\delta\left(l,2k-(m-n)\right)+\delta\left(l,2k+(m-n)\right)+\delta\left(l,-2k+(m-n)\right)\right], \tag{7.34}$$

which leads us to a new term for the total equation

$$\begin{aligned}\nu_{n,m} = &\frac{\sqrt{3}}{2}\frac{a}{\pi}\frac{1}{2}\sum_{k=-\infty}^{\infty} I_k(\alpha)\int_{-\frac{a}{2}}^{\frac{a}{2}} dx\; e^{-i\omega_0(n+m)x}\cdot\ldots \\ &\ldots\cdot\left[I_{2k+(m-n)}\cos\left(2\alpha\cos\left(\omega_0 x\right)\right)+I_{2k-(m-n)}\cos\left(2\alpha\cos\left(\omega_0 x\right)\right)\right].\end{aligned} \tag{7.35}$$

After substituting $h = \frac{2\pi}{a}x$ and expanding the exponential into trigonometric functions, the function can be split into four additive terms

$$\int_{-\pi}^{\pi} dh \;\cos\left((n+m)h\right) I_{2k\pm(m-n)}\left(2\alpha\cos(h)\right) \tag{7.36}$$

$$-\int_{-\pi}^{\pi} dh \; i\cdot\sin\left((n+m)h\right) I_{2k\pm(m-n)}\left(2\alpha\cos(h)\right) \tag{7.37}$$

The sine integrals cancel out due to asymmetry, the cosine integrals by symmetry can be reduced to

$$4\int_{0}^{\frac{\pi}{2}} dh \;\cos\left((n+m)h\right) I_{2k\pm(m-n)}\left(2\alpha\cos(h)\right). \tag{7.38}$$

For this integral a solution can be found in Reference[35], integral Nr. 6.681-11. The solution is

$$\nu_{n,m} \;=\; \frac{\sqrt{3}}{2}\frac{a^2}{\pi}\frac{1}{2}\sum_{k=-\infty}^{\infty} I_k(\alpha)\left(I_{k+n}(\alpha)I_{k-m}(\alpha) + I_{k-n}(\alpha)I_{k+m}(\alpha)\right). \tag{7.39}$$

8 The surface structure of Bi(111) calculated from Helium Atom Scattering measurements using the inelastic Close Coupling formalism

The following corresponds to a publication by
Patrick Kraus, Anton Tamtögl, Michael Mayrhofer-Reinhartshuber, Florian Apolloner, Christian Gösweiner, Salvador Miret-Artés and Wolfgang E. Ernst *submitted to Phys. Rev. B*[54].

The author of this thesis was responsible for

- extension of previous elastic close-coupling (eCC) code to inelastic contributions
- refined SAR and bound-state analysis
- operating eCC and inelastic close-coupling (iCC) simulations and result analysis

The contributions of the co-authors are listed below:

- A. Tamtögl: surface preparation, HAS measurements
- M. Mayrhofer-Reinhartshuber: surface preparation, HAS measurements
- F. Apolloner: assisted authorship on section 8.4
- Ch. Gösweiner: kinematic analysis, definition of the interaction potential, assisted authorship on section 8.3
- S. Miret-Artés: original eCC code, assisted authorship on section 8.5
- W.E. Ernst: supervision (experiment, theory, publication), laboratory, funding

Abstract

Elastic and inelastic Close-Coupling (CC) calculations were used to fit the interaction potential's corrugation height to reproduce angular helium atom scattering spectra of the Bi(111) surface. Earlier investigations of the scattering intensities on Bi(111) relied on two different surface Debye temperatures to explain the varying temperature dependence of the attenuation in specular or elastic scattering contributions. Based on a refined Morse interaction potential and the assumption of only one valid surface Debye temperature, two different approaches are used for the simulation of the surface temperature dependent system. On the one hand, an elastic CC (eCC) calculation is used and the calculated intensities are attenuated by a single Debye-Waller(DW)-factor, on the other hand the eCC code is modified to include inelastic contributions (iCC) which should make the inclusion of a DW-factor unnecessary. The thus obtained corrugation values for Bi(111) correspond more closely with the semimetallic behavior of the surface and cast doubt on the traditional use of the DW approximation for materials with a low surface Debye-Temperature.

8.1 Introduction

The electronic density structure of a surface determines its chemical behavior. While on surfaces like platinum, which is widely used as a catalyst, the effects of crystal face, surface steps and kinks are well-known, more complicated electronic surface structures still lack a detailed treatment. Recently the (111) surfaces of the semimetals bismuth (Bi) and antimony (Sb) have raised a lot of interest. Not only do they represent the two main ingredients of topological insulators[43,102], but they also both present a fairly strong electronic surface density corrugation despite exhibiting conducting surface states[69,71]. The temperature dependence of these peculiar electronic structures may change the binding character of adsorbed species remarkably[83], thus it is essential to determine a complete picture of an electronic surface structure before conducting adsorbate experiments on them. Helium atom scattering (HAS) experiments provide a low-energetic, completely nondestructive means of investigation to measure the pure surface properties of materials. The inert neutral helium atoms are already repelled from the electronic density corrugation above the surface, probing only surface effects. Close-Coupling (CC) calculations[80] provide a significant improvement over simple approximate methods. While the essential accurate knowledge of the interaction potential requires numerous measurements and a careful analysis, the effort may be worthwhile because the quantum mechanical treatment of the scattering procedure provides by far better insights into the scattering processes. Earlier CC investigations included the Debye-Waller (DW) factor to account for the thermal attenuation of scattering intensities. Heavy materials like bismuth however exhibit very low surface Debye temperatures, indicating an extremely

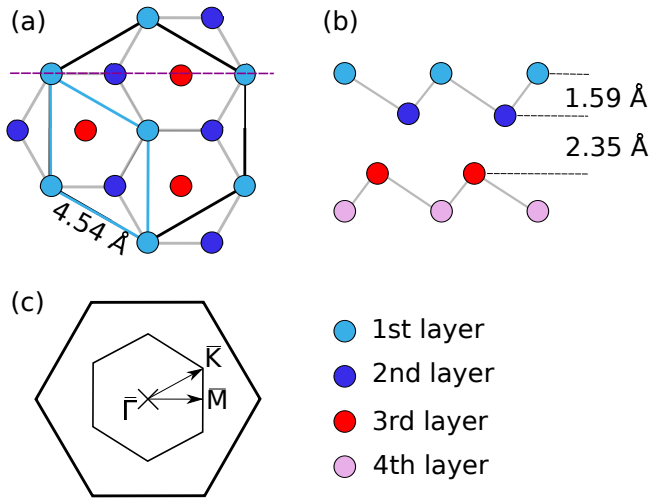

Figure 8.1: (a) Top-view of the Bi(111) surface as determined by Mönig et al.[75]. (b) Side view of the (111) surface along the dashed magenta line in (a). (c) The first Brillouin zone of the topmost layer with the two high symmetry directions.

fast decay of scattering intensities with the surface temperature. Elastic scattering intensities on Bi are even observed at room temperature, which suggested that the initial electronic density corrugation is extremely large when derived by approximate methods[71]. Questions arise whether this strong electronic surface corrugation is a result of the approximate treatment of thermal attenuation. The inclusion of inelastic channels into the CC calculation[73] provides a natural inclusion of the attenuating effects into the plain CC calculation. Since the decay of elastic scattering intensities is now allowed to stray from the simple exponential factor presented by the DW-factor, the true surface electronic density corrugation can be estimated with much higher accuracy.

8.2 Bismuth Surface Structure and dynamics

Bulk bismuth (Bi), like all of the heavier pnictogens, crystallizes in the rhombohedral A7 structure with two atoms per unit cell (space group $R\bar{3}m$). A typical structural property of this crystal structure is the existence of puckered bilayers of atoms perpendicular to the [111] direction, as is illustrated in Fig.8.1(b).

The bonding of the atoms within these bilayers is of a strong covalent type, while the inter-bilayer bonding is closer to a van der Waals-type. This is reflected in the relative distances between the layers, as labeled in Fig. 8.1(b). Due to this strong contrast in binding energies, bismuth crystals preferably cleave perpendicular to the [111] direction. The topmost layer of a so prepared crystal reveals a sixfold symmetry, as illustrated in Fig.8.1(a). Despite the crystals' threefold symmetry, the Bi(111) surface can be treated

as being sixfold symmetric in low-energy HAS experiments[89,90]. The lattice constant of this hexagonal-like surface structure has been determined to be $a = 4.538$ Å by LEED and HAS measurements[71,75]. This hexagonal surface structure leads to two distinguishable high symmetry directions in reciprocal space that are commonly denoted as $\overline{\Gamma M}$ and $\overline{\Gamma K}$, as illustrated in Fig.8.1(c). The reciprocal directions in Fig.8.1(c) correspond with the real-space directions in Fig.8.1(a).
The surface Debye temperature of Bi(111) has been determined to be $\Theta_D = 71(+7/-5)$ K using LEED- and $\Theta_D = (84 \pm 8)$ K using the specular beam in HAS experiments[71,75]. The surface Debye temperature determined from the attenuation of the first order scattering peaks was $\Theta'_D = (75 \pm 8)$ K. The appearance of two different values for the surface Debye temperature for specular and scattered contributions occurs since the theoretical basis for the Debye-Waller factor relies on scattering processes without momentum transfer (see Section 8.4). Especially the specular HAS value reproduces the theoretical approximation of van Delft[96] that estimates the surface Debye temperature to be lower than the bulk value, which is 120 K[33,78], by a multiplicative factor of $1/\sqrt{2}$.

8.3 Experimental Setup

All measurements mentioned and used in this work have been carried out on a helium atom scattering apparatus with a fixed source-target-detector angle of 91.5° that has been described in a previous publication[91]. The helium-atom beam is produced via supersonic expansion of He-gas through a cooled nozzle at 50 bar which is followed by a skimmer creating a spatially and energetically narrow beam ($\Delta E/E \approx 2\%$). The Bi-sample is positioned on a 7-axis manipulator in the main chamber at a base pressure of 10^{-11} mbar. The sample can be cooled using LN_2 or heated using a button heater while the temperature is measured by a type K thermocouple. The scattered He-atoms are then detected by a quadrupole mass spectrometer followed by a multi channel analyzer. Angular elastic scans can be carried out by rotating the manipulator leading to diffraction spectra (0.1° resolution). Time of flight measurements allow to record inelastic scattering spectra and are realized using a pseudo random chopper disc and subsequent deconvolution of the measured signal. The disc-shaped Bi(111) single crystal sample with a diameter of 15 mm and a thickness of 2 mm has been cleaned using several cycles of Ar^+ sputtering and followed annealing at 150 °C. Surface cleanliness and contamination were checked via Auger electron spectroscopy (AES) and the intensity of the diffuse elastic peak, its orientation has been aligned using a low-energy electron diffraction (LEED) system. Experiments can be carried out within a beam energy range of 15 meV to 25 meV with the sample cooled (113 K) or at room-temperature in the two main symmetry directions of the crystal surface.

8.4 Debye-Waller Attenuation

As observed in earlier measurements[71], diffraction peak intensities are surface temperature dependent. This thermal attenuation can be described via the so-called Debye-Waller (DW) factor[56]. It is a result of the zero-point motion and the thermal vibrations of the surface atoms, which cause inelastic scattering of the impinging atoms. The DW factor relates the intensity $I(T_S)$ of diffraction peaks at temperature T_S to the intensity I_0 at zero surface temperature by

$$I(T_s) = I_0 \mathrm{e}^{-2W(T_S)} \tag{8.1}$$

where $exp(-2W(T_S))$ is the Debye-Waller factor. Although the theoretical basis for the DW factor has been developed for neutron and X-ray diffraction[28], a reasonable approximation for surfaces can be given by

$$2W(T_S) \simeq \left\langle u_z^2 \right\rangle (\Delta k_z)^2 \tag{8.2}$$

assuming zero parallel momentum transfer to the surface and final angles near the specular angle. $\langle u_z^2 \rangle$ describes the average displacement of the atom perpendicular to the surface and Δk_z is the momentum transfer perpendicular to the surface during the scattering event. Assuming a harmonic oscillator within the Debye model $W(T_S)$ becomes

$$W(T_S) = \frac{3\,(\hbar^2 \Delta k_z^2)\,T_S}{2 M k_B \Theta_D^2} \tag{8.3}$$

with M being the mass of the surface atom, k_B the Boltzmann constant and Θ_D the surface Debye temperature[28,60].

The applicability of the conventional DW-factor which was introduced for X-ray diffraction in atom-surface scattering models[36,47] has been discussed extensively in theory as well as in experiments. Different models have been discussed by A. C. Levi[59], who for example predicts an increase of diffraction intensities for soft potentials. Deviations from the predicted temperature dependencies of DW-factors especially at high surface temperatures have been experimentally observed on the He-Cu(001) system. These deviations have been analyzed with special focus on the role of the interaction potentials and scattering from surface defects[99]. Multiphonon and resonance effects concerning the dependency of the initial particle energy on the DW-factor for a coupled channel approach which can not be described by the Born approximation are described in a comparatively new publication of W. Brenig[17]. Multiphonon effects in the evolution of the DW-factor have already been observed on popular scattering targets like LiF[97] and still lack a proper treatment in the standard DW-model.

8.5 Inelastic Close-Coupling

The close-coupling (CC) formalism provides a method for calculating the intensities of scattering experiments exactly (up to numerical convergency) in the elastic and inelastic regimes[80]. The helium atom is considered to be a structureless and non-penetrating particle, while the surface corrugation contains a static and a dynamical time dependent contribution.

The time-dependent Schrödinger equation for a structureless particle is written as

$$\mathrm{i}\hbar \frac{\partial \Psi(\boldsymbol{r},t)}{\partial t} = \left[-\nabla^2 + V(\boldsymbol{r},t)\right] \Psi(\boldsymbol{r},t), \tag{8.4}$$

where squared wave vector quantities are given in energy units with $\hbar^2/2m = 1$, m being the mass of the incident particle. The standard notation is also used here where capital letters are for vectors parallel to the surface (2D) and small letters for vectors in 3D. The gas–surface interaction, V, turns out to be dependent on time through the instantaneous position of the surface atoms, $\mathbf{R}+\mathbf{u}(\mathbf{R},t)$, with $\mathbf{u}(\mathbf{R},t)$ being the deviation or displacement from the equilibrium position. If this displacement is considered to behave as a Gaussian function within the unit cell, it can be written as[73]

$$\begin{aligned} \mathbf{u}(\mathbf{x},t) &= \mathbf{u}_{\mathbf{z},0} \exp(-x^2/\sigma_c^2) \cos\omega t, \\ \mathbf{u}(\mathbf{y},t) &= \mathbf{u}_{\mathbf{z},0} \exp(-y^2/\sigma_c^2) \cos\omega t, \end{aligned} \tag{8.5}$$

with $\mathbf{u}_{\mathbf{z},0}$ the initial amplitude, ω the frequency of the active phonon mode and σ_c the parameter to describe the width of the Gaussian function.

As long as the relative displacements $\mathbf{u}$ are small compared to the lattice constant, the interaction potential can be Taylor expanded up to first order (within the so-called single-phonon approximation) as[25]

$$V(\mathbf{r},t) \;\simeq\; V(\mathbf{r}) \;+\; \mathbf{u}(\mathbf{R},t) \cdot \nabla V(\mathbf{r}). \tag{8.6}$$

From the layer description of lattice dynamics it is well–known that the $\boldsymbol{u}$–displacement can be, in general, written as

$$\boldsymbol{u}(\boldsymbol{R},t) = \sum_{\boldsymbol{Q},\nu} \boldsymbol{A}(\boldsymbol{Q},\nu,T)\, \mathrm{e}^{\mathrm{i}\boldsymbol{Q}\cdot\boldsymbol{R}} \cos\left[\omega_\nu(\boldsymbol{Q})t\right], \tag{8.7}$$

where the amplitude $\mathbf{A}$ includes the phonon polarization vector and the dependence on the surface temperature and $\omega_\nu(\mathbf{Q})$ is the frequency of the mode with quantum numbers $(\mathbf{Q},\nu)$. For most practical purposes, only displacements of atoms on one layer (or two at most) significantly contribute to the interaction potential. In the Taylor expansion given by Eq. 8.6, the zero order or static part of the interaction, $V(\mathbf{r})$, is evaluated at

zero displacements. Considering the periodicity of the lattice surface, this function can then be expanded into a Fourier series

$$V(\mathbf{r}) \;=\; \sum_{\mathbf{G}} V_{\mathbf{G}}(z)\mathrm{e}^{i\mathbf{G}\cdot\mathbf{R}} \tag{8.8}$$

with $\mathbf{G}$ being the reciprocal lattice vector.

On the other hand, the wave function, $\Psi(\boldsymbol{r},t)$, has to take into account the double periodicity given by the Hamiltonian in space and time. Thus, according to the Bloch theorem, $\Psi(\boldsymbol{r},t)$ can be expanded as

$$\begin{aligned}\Psi(\boldsymbol{r},t) = \mathrm{e}^{-\mathrm{i}\boldsymbol{k}_i^2 t/\hbar} \;& \textstyle\sum_{\boldsymbol{G},\boldsymbol{Q},\nu,n_{\boldsymbol{Q},\nu}} \Psi_{\boldsymbol{G}+\boldsymbol{Q},n_{\boldsymbol{Q},\nu}}(z) \\ & \cdot\mathrm{e}^{\mathrm{i}(\boldsymbol{K}_i+\boldsymbol{G}+\boldsymbol{Q})\cdot\boldsymbol{R}}\,\mathrm{e}^{\mathrm{i}n_{\boldsymbol{Q},\nu}\omega_\nu(\boldsymbol{Q})t},\end{aligned} \tag{8.9}$$

where $n_{\boldsymbol{Q},\nu}$ stands for the number of phonons of the mode $(\boldsymbol{Q},\nu)$. In this work, we are going to consider the inelastic effects on the elastic intensities. Thus, the Bragg law (for $\mathbf{Q}=0$) is written as

$$\Delta\mathbf{K} = \mathbf{K}_f - \mathbf{K}_i = \mathbf{G}. \tag{8.10}$$

Moreover, we also assume that only one mode is active in the scattering process. Thus, we can drop the subindex $(\boldsymbol{Q},\nu)$ in $n_{\boldsymbol{Q},\nu}$ for the number of phonons, writing only n. Similarly, for the frequency of the active mode we can write simply ω. After substituting Eqs. (8.6), (8.8) and (8.9) into Eq. (8.4), multiplying the resulting expression by $\exp[-\mathrm{i}(\boldsymbol{K}_i+\boldsymbol{G})\cdot\boldsymbol{R}]$ and $\exp[-\mathrm{i}n\omega t]$, and then integrating over both time and the area of a single unit cell, one obtains[73] the following set of coupled differential equations for the diffracted waves

$$\begin{aligned}\left[\frac{\mathrm{d}^2}{\mathrm{d}z^2} \;+\; \mathbf{k}^2_{\mathbf{G},n,z} - V_{\mathbf{0}}(z)\right]\Psi_{\mathbf{G},n}(z) &= \sum_{\mathbf{G}'\neq\mathbf{G}} V_{\mathbf{G}-\mathbf{G}'}(z)\,\Psi_{\mathbf{G}',n}(z) \\ &+ \mathbf{A}\cdot\sum_{\mathbf{G}'\neq\mathbf{G}} \mathbf{F}_{\mathbf{G}-\mathbf{G}'}(z)\left[\Psi_{\mathbf{G},n+1}(z)+\Psi_{\mathbf{G},n-1}(z)\right],\end{aligned} \tag{8.11}$$

and

$$\begin{aligned}\left[\frac{\mathrm{d}^2}{\mathrm{d}z^2} \;+\; \mathbf{k}^2_{\mathbf{G},n+1,z} - V_{\mathbf{0}}(z)\right]\Psi_{\mathbf{G},n+1}(z) &= \sum_{\mathbf{G}'\neq\mathbf{G}} V_{\mathbf{G}-\mathbf{G}'}(z)\,\Psi_{\mathbf{G}',n}(z) \\ &+ \mathbf{A}\cdot\sum_{\mathbf{G}'\neq\mathbf{G}} \mathbf{F}_{\mathbf{G}-\mathbf{G}'}(z)\left[\Psi_{\mathbf{G},n+2}(z)+\Psi_{\mathbf{G},n}(z)\right],\end{aligned} \tag{8.12}$$

where

$$\boldsymbol{k}^2_{\boldsymbol{G},n,z} = \boldsymbol{k}_i^2 - (\boldsymbol{K}_i+\boldsymbol{G})^2 - n\hbar\omega \tag{8.13}$$

is the z–component of the kinetic energy for the $\boldsymbol{G}$–diffracted wave, and

$$\mathbf{F}_{\boldsymbol{G}-\boldsymbol{G}'}(z) \equiv [\mathrm{i}(\boldsymbol{G}-\boldsymbol{G}')V_{\boldsymbol{G}-\boldsymbol{G}'}(z), V'_{\boldsymbol{G}-\boldsymbol{G}'}(z)] \tag{8.14}$$

is the contribution of the gradient of the interaction potential or vector force field (V' represents the first derivative with respect to z); the first component represents the (x,y) components of the force and the second one its z component. Within this scheme, each channel is then represented by an effective potential formed by $V_{\mathbf{0}}(z)$ plus the asymptotic energy, given by

$$(\boldsymbol{K}_i + \boldsymbol{G})^2 + n\hbar\omega \tag{8.15}$$

Such a channel is called an inelastic diffraction channel, and each inelastic event — annihilation or creation— is represented by one of these channels with (n-1) or (n+1). Similarly, the wave functions associated to the discrete spectrum (bound states labelled by v) are denoted by $|\boldsymbol{K}_i+\boldsymbol{G}, n, v\rangle$ and those associated to the continuum one (diffracted beams) by $|\boldsymbol{K}_i+\boldsymbol{G}, n, \boldsymbol{k}^2_{\boldsymbol{G},n,z}\rangle$. In the literature it is said that the channels are *dressed* by the phonon field. The number of channels dressed by a given number of phonons form a block, called a *Floquet block*. Thus, if only single–phonon scattering is considered, three Floquet blocks must be at least included in the calculation: the blocks dressed by minus and plus one phonon of the active mode, and the block dressed by zero phonons (the latter corresponding to the pure elastic contribution). The number of diffraction channels within a given block is formed at least for those used to obtain numerical convergence in an elastic CC calculation. Multiphonon contributions of the same active mode are taken into account by including more Floquet blocks - those dressed by two, three, or more phonons by following the staircase structure of Eqs. (8.11) and (8.12) through $n \pm 1$. Furthermore, two coupling terms of very different nature are now present: $V_{\boldsymbol{G}-\boldsymbol{G}'}(z)$ is responsible for the intrablock coupling, and the scalar function

$$\boldsymbol{A}(T) \cdot \mathbf{F}_{\boldsymbol{G}-\boldsymbol{G}'}(z) \tag{8.16}$$

for the interblock one. The latter is responsible for the thermal attenuation of the diffraction intensities (see Eqs. (8.11) and (8.12)) described many times from a phenomenological viewpoint by a DW factor.

In previous publications on the phonon dispersion of the Bi(111) surface[89,90], the lowest-lying, isolated Rayleigh mode was identified as the shear-vertical mode corresponding to the sole phonon dispersion line in the Debye model. According to the shear-vertical polarization of the suggested mode, the horizontal displacement of the lattice atoms can be neglected, simplifying the force term Eq. 8.14 to the horizontal term

$$\mathbf{F}_{\boldsymbol{G}-\boldsymbol{G}'}(z) \simeq V'_{\boldsymbol{G}-\boldsymbol{G}'}(z), \tag{8.17}$$

and consequently the inelastic coupling term to

$$\boldsymbol{A}(T) \cdot \mathbf{F}_{\boldsymbol{G}-\boldsymbol{G}'}(z) \simeq \boldsymbol{A}(T) \cdot V'_{\boldsymbol{G}-\boldsymbol{G}'}(z). \tag{8.18}$$

The average thermal displacement $A_z(T)$ is related to the effective mean square displacement and has been estimated[73] to be

$$\boldsymbol{A}(T) \;=\; \frac{1}{aQ_c}\sqrt{\frac{384\hbar^2\pi T}{Mk_{\mathrm{B}}\Theta_{\mathrm{D}}^2}}, \tag{8.19}$$

with T the actual surface temperature, Θ_{D} the surface Debye temperature, M the mass of a surface particle, a the lattice constant and Q_c is a fitting parameter for the Gaussian cut-off factor given by $Q_c = 2/\sigma_c$ with σ_c being the width parameter introduced in Eq.8.5.

On the other hand, when solving the inelastic CC equations, frequency dependent diffracted intensities are obtained and these have to be averaged by assuming a density of phonons in order to compare with the experimental ones. The corresponding integration over phonon frequencies is naturally weighted by the Debye spectral density given by

$$\rho(\omega) = \frac{2\omega^2}{\omega_{\mathrm{D}}^3}. \tag{8.20}$$

with ω_{D} the Debye frequency. In this respect, the final intensities are caused by the virtual phonon events only, no real phonon events are taken into account since the corresponding momenta are not involved in Bragg's law. The term 'virtual events' denotes that when the photon is created in the dynamics, it has to be annihilated in order to have a net energy balance equal to zero. The origin of the attenuation in the iCC formalism is precisely due to the virtual phonon events since they are responsible for the appearance of the new inelastic channels.

For antimony, the elastic coupling parameters for a lattice with the same surface structure has been calculated in a previous publication[53] for a corrugation represented as a sum of cosine functions from a Fourier expansion up to the second term, such as

$$\begin{aligned}\xi(x,y) \;=\; \xi_0\left(\cos\left[\frac{2\pi}{a}\left(x-\frac{y}{\sqrt{3}}\right)\right]\right. \\ \left.+\cos\left[\frac{2\pi}{a}\left(x+\frac{y}{\sqrt{3}}\right)\right]\right)+\xi_0\cos\left[\frac{2\pi}{a}\frac{2y}{\sqrt{3}}\right]+h.o.,\end{aligned} \tag{8.21}$$

with ξ_0 the corrugation amplitude. By assuming a corrugated Morse potential leading to

$$V_{\mathbf{G}-\mathbf{G}'}(z) \;=\; D\frac{\nu_{h,k}}{\nu_{0,0}}e^{-2\kappa z} \tag{8.22}$$

where D is the well depth of the Morse potential, the $G(n,m)$-specific coupling constants $\nu_{n,m}$ are given by

$$\begin{aligned}\nu_{n,m} \;=\; \frac{\sqrt{3}}{2}\frac{a^2}{\pi}\frac{1}{2}\sum_{k=-\infty}^{\infty} & I_k(\alpha)\left(I_{k+n}(\alpha)I_{k-m}(\alpha)+\right. \\ & \left.+I_{k-n}(\alpha)I_{k+m}(\alpha)\right),\end{aligned} \tag{8.23}$$

where I_k are the modified Bessel functions of first kind and $\alpha = 2\kappa\xi_0$.

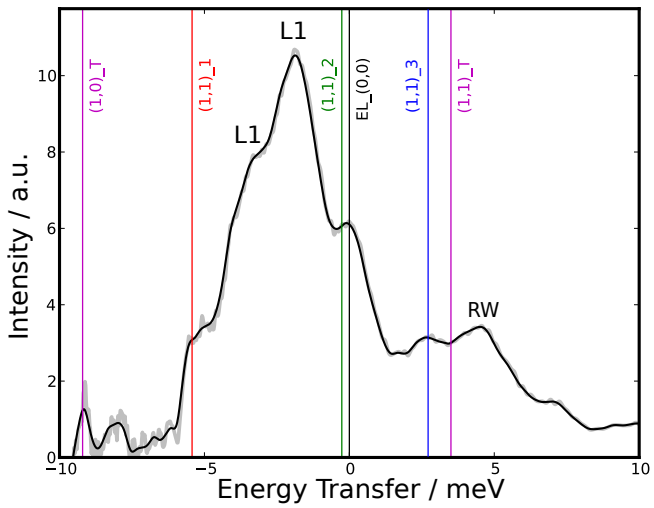

Figure 8.2: Time-of-Flight spectrum of Bi(111) in $\overline{\Gamma M}$ direction at an incident angle of 54.9° and an incident energy of 17.5 meV. The suggested bound state energy level coincides with an observed increase in intensity around an energy transfer of +3 meV.

8.6 Results and Discussion

8.6.1 Inelastic TOF and Interaction Potential

Previous investigations of the He-Bi(111) interaction potential[55] revealed three well defined bound state energies and the associated 9-3 interaction potential shape. However, preceding studies of close-coupling routines using various potential shapes on Sb(111)[53] suggest that Morse- or Morse-like potential shapes perform better in representing the bound state energies as well as in the elastic close-coupling simulation of semimetal surfaces. Given only three low-lying bound state energies, the long-range interaction shape would not be represented in the fitting procedure.

To propose a more accurate Morse-like interaction potential, indications of inelastic resonance effects in time-of-flight (TOF) spectra were analyzed to identify an additional bound state level at smaller bound state energies. Figure 8.2 illustrates one of the spectra with an isolated feature originating from the fourth identified bound state as listed in Table 8.1.

The last line of Table 8.1 lists the obtained bound state energy levels for the fitted central part of the corrugated Morse potential.

$$V_{00}^{\mathrm{M}}(z) = D\left[e^{-2\kappa z} - 2e^{-\kappa z}\right] \tag{8.24}$$

with a potential depth D of (7.898 $\pm$0.126) meV and a potential stiffness κ of (0.884 $\pm$ 0.024) Å^{-1}. With the highest identified bound state level much closer to the thresh-

Table 8.1: Measured and fitted bound state energy levels for the He-Bi(111) interaction potential. The first three measured values were taken from[55].

Level no. / #	0	1	2	3
Measured / meV	6.18	3.49	1.42	0.327
Morse-fit / meV	6.20	3.43	1.47	0.327

old, the attractive part of the fitted potential may be considered to describe the real interaction accurately.

8.6.2 eCC and iCC Analysis of Bi(111)

Previous investigations[71] treated the electron density corrugation of the Bi(111) from the Helium Atom Scattering (HAS) data using the GR method and the Eikonal approximation, including the Beeby correction. Thermal attenuation effects were included using the Debye-Waller factor as described in Section 8.4 with two different surface Debye temperatures to account for the different attenuation characteristics obtained in the measurements. The surface Debye temperature being an intrinsic surface property given by the maximum energy of the phonons in the Debye model, it seems unsatisfactory to include a second temperature in order to account for the different attenuation of the scattering channels. Thus, all the intensities in the eCC+DW model were achieved using only one surface Debye temperature. Since approximate methods are widely used in surface science, the majority of corrugation effects measured still lack a quantum mechanically exact treatment such as a close-coupling approach.

To find appropriate values for the surface corrugation and the surface Debye temperature (two parameters for the eCC calculation) as well as the Gaussian cut-off factor Q_C in the iCC case (three parameters for the iCC calculation), two sets of optimization routines were used. In the first case the electron density corrugation was fitted from four complete angular scans in $\overline{\Gamma M}$ and $\overline{\Gamma K}$ at 113 K as well as at 300 K surface temperature using an eCC algorithm attenuated with a simple DW factor. Correspondingly, the corrugation height as well as the Debye temperature had to be optimized simultaneously. In the second case, an iCC algorithm was used, expanding the parameter space by one dimension through adding the Gaussian cut-off factor Q_C. In both cases, the overall deviation of the measured intensities from the calculated intensities

$$\sigma = \frac{1}{N}\sqrt{\sum_{n=1}^{N}(I_n^{calc} - I_n^{exp})^2} \tag{8.25}$$

with N being the total number of scattering intensities considered (in this case 12) was minimized. The optimization algorithm terminated after a relative accuracy of 0.1 % in all of the considered parameters.

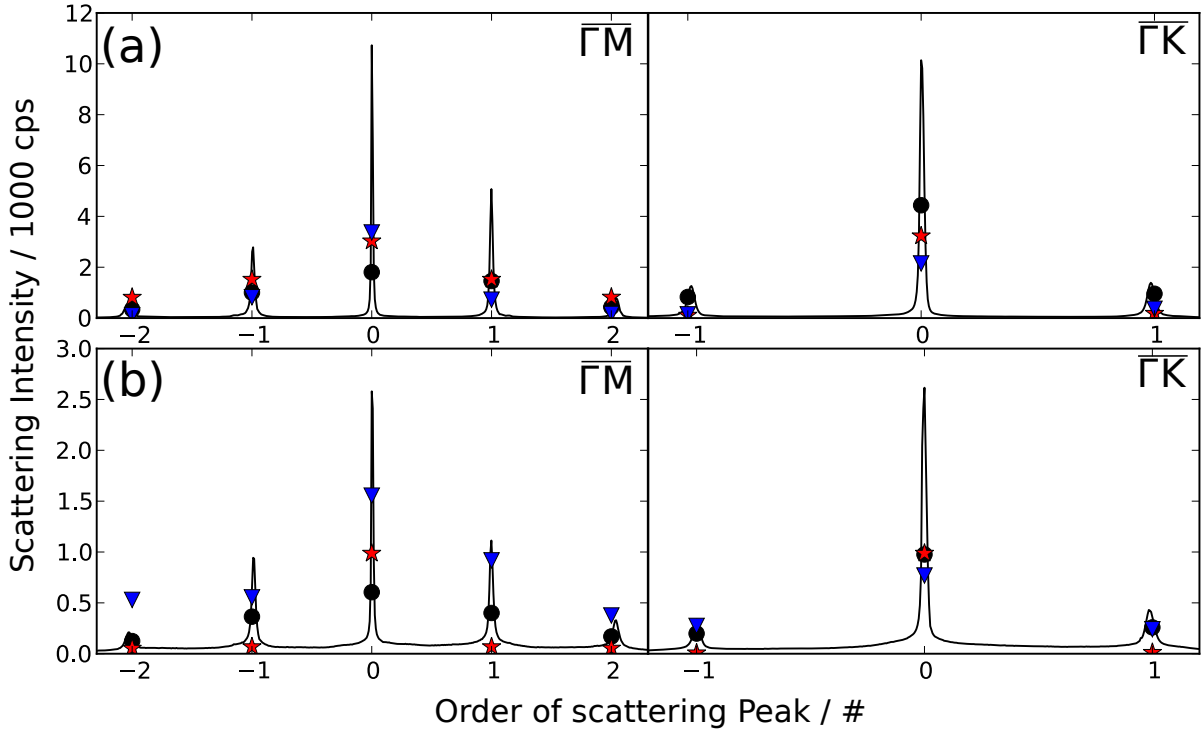

Figure 8.3: Measured and calculated scattering peak intensities in both distinguishable lattice directions at two surface temperatures and a beam energy of 16 meV. Black dots signify measured peak areas, red stars calculated peak intensities using elastic close-coupling with a Debye-Waller attenuation, blue downward triangles calculated peak intensities using the inelastic close-coupling approach. (a) Angular scans in $\overline{\Gamma M}$ and $\overline{\Gamma K}$ direction at a surface temperature of 113 K. (b) Angular scans in $\overline{\Gamma M}$ and $\overline{\Gamma K}$ direction at a surface temperature of 300 K.

Table 8.2: Comparison of earlier relative peak-to-peak corrugation values to corrugation values calculated by eCC and iCC. All values are given in % of the lattice constant a

GR Method[71]	9.7 - 10.1
Eikonal Approx.[71]	10.6 - 11.2
eCC + DW	8.13
iCC	6.32

Figure 8.3 displays the best-fitting results in both cases of elastic and inelastic close coupling calculations. To obtain comparable values, the experimental scattering peak areas were normalized to the specular peak area of the 113 K measurement for each direction separately. The elastic CC-calculation with the Debye-Waller attenuation (red stars) represents the measurements more closely only at lower surface temperatures in $\overline{\Gamma M}$-direction (a), but seems unable to reproduce the data in the case of the sample being at room temperature (b). The inelastic calculation (blue downward triangles) on the other hand seems to underestimate the scattering intensity in the low temperature measurements, while producing plausible scattering intensities at room temperature. The elastic calculation is furthermore not capable of predicting the first order scattering intensities in $\overline{\Gamma K}$ direction, an issue that also occurred in earlier scattering simulations on the Sb(111) surface when using the plain Morse potential[53,69].
These values were obtained for the corrugation values listed in Table 8.2.

The obtained corrugation values are significantly lower than the ones obtained by approximate methods[71]. While the elastic approach with the simple numeric attenuation factor already settles at a peak to peak corrugation of 8.13 % of the lattice constant, the inelastic close-coupling calculation returns a value of 6.32 %, with a Gaussian cut-off factor of 0.869 Å^{-1} and a Debye-Temperature of 84.26 K, which coincides well with the value obtained by Mayrhofer et al.[71]. The inelastic calculations were carried out using 150 scattering channels in 3 Floquet blocks from -7 Å to 16 Å with 100 steps within the shortest calculated wavelength. The phononic energy integration was performed via a simple weighted Legendre quadrature from zero energy to the Debye frequency with 10 evaluated roots.
While the small Debye Temperature of Bi(111) influences both the Debye-Waller factor and the inelastic coupling constant (see Section 8.5, Eq. 8.19), the iCC approach is the only one that would allow a deviation of the temperature dependence of the elastic scattering peaks from the exponential characteristic. Thus, while the Debye-Waller factor explains the temperature dependence of the specular peak better than the iCC calculation, the latter is not bound to attenuate the scattered peaks at the same rate,

producing intensity predictions far from zero also when the surface temperature is much higher than the surface Debye temperature.
However, the present model only accounts for interactions without any parallel momentum transfer (see Section 8.5) and assumes all phonons to be polarized completely parallel to the surface normal with a uniform polarization amplitude, which is clearly not the case in any realistic crystal. Earlier ab-initio calculations[90] for example reveal a mixed polarization of the Rayleigh branch, which shifts from shear vertical to longitudinal polarization when reaching higher phonon momentum.

We are aware that the dynamical corrugation given by Eq.8.5 for x and y assumes a different geometry of the unit cell than encountered in the case of Bi(111). This is the first attempt to apply this theory to a real 2D surface. Obviously, the iCC framework has to be better adapted to the actual geometry of the surface unit cell under consideration and, in our opinion, the main discrepancies between the experimental and inelastic results should be attributed to this important point. At higher surface temperatures, where the corresponding dynamical corrugation is higher, the general shape of the dynamical displacement function does not seem to play an important role and the overall agreement with the experimental results is better. An extension of the coupling calculations including a complete treatment of the overall force (Eq. 8.14) and the correct geometry on the scattered helium atom in surface parallel directions could account for the different polarization directions and improve the quality of the calculated scattering intensities significantly. The overall ability of the iCC calculations to model the measured scattering features could be vastly improved if the in this case previously determined interaction potential parameters would enter the fitting procedure directly instead of being pre-determined solely from bound state feature fitting. However, expanding the included parameter space to five dimensions (corrugation height, Debye temperature, Gaussian cut-off, potential depth, potential stiffness) would raise the number of necessary function evaluations enormously, resulting in unfeasible calculation times. Furthermore, including a more realistic interaction potential shape, probably determined by ab-initio approaches would render the iCC method a remarkable tool for simulating the effects of inelastic scattering contributions in temperature dependent measurements.
Using the inelastic close-coupling approach to simulate the scattering from surfaces with finite temperatures clearly renders the inclusion of an additional surface Debye temperature futile and furthermore resolves the $\overline{\Gamma K}$ prediction problems encountered in eCC calculations with the plain corrugated Morse potential[53,69]. By not being bound to an exponential attenuation characteristic, the method is more adaptive and thus better suited to describe the temperature dependent behavior of surfaces with a comparatively low surface Debye temperature.

9 Summary

The present work presents the development of the exact treatment of the surface-probe particle interaction for the pnictogen surfaces Bi(111) and Sb(111) as well as the benefits such a description poses compared to earlier approximative methods.

9.1 He-surface interaction potential

Intensity variations in between elastic helium scattering features on Bi(111) and Sb(111) lead to the measurement of a set of bound state energies for the interaction potentials of both surfaces with the helium atoms. These bound state energies represent a subset of the eigenenergies of the bound He-surface system. The surface-averaged interaction potential for both systems was derived in accordance to those eigenvalues. Using the known positions of these resonance possibilities, experiments on Bi(111) were conducted to selectively enhance the sub-surface optical phonon modes which would otherwise be concealed by the Jacobi-amplified background noise on the phonon creation side of TOF measurements. The depths of both potentials can be used for the Beeby correction in Debye-Waller analysis, if such an approach is necessary. In the subsequent research presented in chapter 7 several different interaction shapes were included in the analysis within the limits of the experimental uncertainty of the bound state analysis. In order to accomplish this, the commonly used least-squares fit was exchanged with a weighting function taking the probability distribution of the measured values into account. The performed fits for the He-Sb(111) interaction potential reveal that most interaction potential shapes are at least equivalent when solely observing the bound state energies, as can be viewed in table 7.1. Only the additive-potencies potentials, namely the 9-3 and the 12-3 potentials seem to fail in this kind of description.

9.2 Scattering description using the CC-formalism

The newly found knowledge about the potential shape renders a quantum mechanically exact treatment of the scattering process possible. During the course of this work the one-dimensional elastic close-coupling *Fortran* code supplied by Prof. Miret-Artés was adapted to a full two-dimensional inelastic code written in *Python* and supplied with the analytical expressions to make calculations on a hexagonal surface grid viable.

Table 9.1: Comparison of derived corrugation heights from earlier approximative methods and close-coupling analysis with respect to the corresponding lattice constants. All listed close-coupling corrugations were calculated using the fitted Morse potential.

	Approx. Methods	eCC	iCC
Bi(111)	10 - 11 %[71]	8.13%	6.32%
Sb(111)	13 %[70]	13-14%	-

The implications of elastic as well as inelastic close-coupling treatment of the scattering analysis are dramatic. Earlier works[69–71] described the surface corrugation of the semimetals antimony and bismuth and drew the seemingly contradictory conclusion that despite the presence of conducting surface states on both materials, the surface corrugation is extraordinary high with values ranging from 12-13% for antimony and around 10% for bismuth. While a first analysis using the close-coupling formalism on Sb(111) resulted in a corrugation value of even 17%, a subsequent analysis using a wide range of possible interaction potential shapes revealed a whole spectrum of possible corrugation heights ranging from 13.5-19.1% depending on the potential used. The usually well-fitting Morse potential completely fails in describing second-order $\overline{\Gamma M}$ or first-order $\overline{\Gamma K}$ scattering intensities. While this was usually attributed to the incorrectly described attractive interaction alone, further investigations on Bi(111)[54] using a version of the close-coupling formalism including inelastic interactions produced predicted intensities in these positions, indicating the possibility for a helium atom to reach an elastic scattering channel through scattering into an inelastic channel first. Considering this process the calculated corrugation of the He-Bi(111) interaction potential can be reduced to 6.32 % when including inelastic interaction only for the Rayleigh branch and ignoring the phonon momentum.

Table 9.1 lists the obtained corrugation values for the Morse potentials in comparison with the approximative methods conducted by earlier group members.

Acknowledgements

Finally the time has come to say thank you for everything everyone ever did for me. My time in this project didn't seem too long, neither did my time studying physics up to now, even if it have been some years. The complexity of the problems encountered changed slightly - from my severe problems in struggling with the French language when I was in school - to summarizing an article on integration methods for coupled differential equations written in Spanish to integrate it into my English-written thesis. Honestly, to this day I prefer the latter issue. As can be expected I had a lot of help on the way - some direct and obvious - some indirect and subtle. If I should be honest I would have to thank everyone beginning at the very system that allowed me to undergo 21 years of education (no, I don't count the military service) at a great expense for both our society and for my parents, down to that Arabic shepherd - whose name has long been forgotten - who first deducted from the behavior of his sheep after eating from the *Coffea Arabica* bush that its berries could keep you awake. To narrow this section of my thesis down I will only thank the core of the most direct supporters.
First of all, I have to thank my supervisor Prof. Wolfgang E. Ernst, whose patience kept this project running. I am sure a machine failing and SO dramatically SO many times before completion would have been cut off money and support in most other institutions. The more I have to thank the former members of the HAS group Michael Mayrhofer-Reinhartshuber and Anton Tamtögl, who led H.Å.N.S to maturity and me through the darkness of complexity that were my first years trying to grasp the technique. Mike has been a friend since first semester, when we shared a room in the probably most terrifying dorm in Graz. I don't believe my time as a student would have turned out the same if we omitted the late-night linear-algebra study sessions till 3 a.m. (including considerable consumption of Mirto...), or the regular Go sessions in front of the institute building. I am also convinced the optimism and general reluctance to take ourselves too seriously of our group prevented Toni from prematurely ragequitting his PhD. Toni has been the best *Captain* imaginable and only his endurance in repairing H.Å.N.S over and over enabled us to steer our little *UHV-pirate-submarine* through the shallows into the harbor of scientific publishability. The loss of both my teammates at the end of 2013 hit me pretty hard, but their replacements Florian Apolloner and Christian Gösweiner proved themselves to be respectable substitutes who seem to be more than willing to carry on the spirit of the *He-Surfers*. The introduction of Petra and Alicia, our much beloved Coffeemachines lead to frequent social interaction, which is more than common prejudice

"Piled Higher and Deeper" by Jorge Cham, www.phdcomics.com

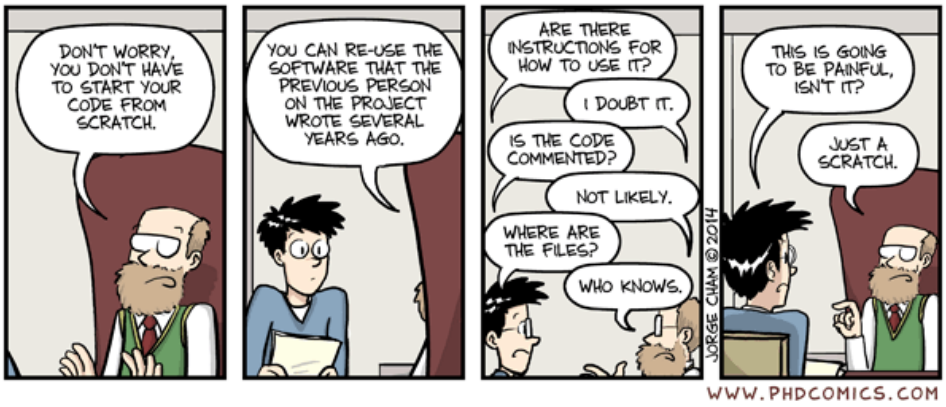

would assume in a physics institute. During these valuable coffee breaks the views of grad-school life and outdoor activities lead to a lot of discussions with Michaela Ellmeier and Günter Krois, who I also thank for lots of very *Austrian* philosophy discussions in the style of '*Live every day as if it's your last - lots of whining, moaning and general pitifulness*'. One of the events that steered the trajectory of my work into the path it followed up to now was the first visit of Prof. Girgio Benedek right after I started my Master Thesis at this project. His influence and constant support motivated us to join the PCAM doctorate and enabled me not only to work with him in Milano, but also later in San Sebastián. Without Prof. Benedek's advise and frequent and patient answers to my (uninformed) questions, the whole issue of surface interaction and resonances would never have caught our attention at all. Through Prof. Benedek I also had the pleasure to meet Davide Campi, who I will always regard as the DFT-Archmage that he really is, even if he belittles his talent. At my six-month stay in Spain, I had the fortune to meet Prof. Salvador Miret-Artés, who introduced the *Close-Coupling* formalism to us, which serves as the backbone of the work you are currently holding in your hands. Reviving and extending his old *Fortran* code was thrilling, even if it lead to several issues so common in science, it was even featured on PhDcomics.com (see the supplied figure). During this time I had to rely on a lot of financial support, so at this point I want to thank the TU Graz office for international relations, the Austrian Research Association and especially the Federation of Carinthian Industries, whose extremely generous support enabled me to go to Spain and realize this work. I also have to thank the staff of the secretariat and the mechanical and electrical workshops, which whose help neither the organization nor the realization of this project would be imaginable.

I also need to thank my family, who at first proved patient enough to keep me in school and then suffered through numerous visits where I just sat on the couch talking about nerdy stuff only physics students might find interesting. Finally I want to thank Heike, my friend, girlfriend and partner, who listened when there was something to say, and who always supported me when I needed it most. Thank you.

Danksagung

Nun ist endlich der Moment gekommen, an dem ich mich bei allen, die mir je geholfen haben bedanken kann. Meine Zeit an diesem Projekt, ebenso wie meine gesamte Studienzeit wirkt rückblickend nicht so lange wie sie tatsächlich war. Der Grad an Komplexität meiner Probleme hat sich leicht verändert - von meinen schweren Problemen mit der französischen Sprache in der Schule - zu Problemen damit, einen spanisch abgefassten Artikel über Lösungsmethoden für gekoppelte Differentialgleichungssysteme ins englische zu übersetzen, damit ich ihn in meine Dissertation einbauen kann. Um ganz ehrlich zu sein bevorzuge ich bis heute das zweite genannte Problem. Natürlich genoss ich auf diesem Weg einiges an Hilfestellung - einige direkt und offensichtlich - und einige indirekt und versteckter. Wenn ich vollständig ehrlich sein sollte müsste ich allen danken, angefangen von unserem Schulsystem, welches mir 21 Jahre Bildung (nein, der Grundwehrdienst wird nicht gezählt) - nicht nur zu Lasten der Finanzen meiner Eltern, sondern auch vom Staat gefördert - ermöglichte - bis zu dem lange vergessenen arabischen Schafhirten, welcher als erster die Wirkung der Bohnen des *Coffea arabica* Busches auf das Verhalten seiner Schafe beobachtete und die richtigen Schlüsse zog. Um diesen Teil meiner Dissertation nicht so weit auszudehnen, werde ich mich allerdings nur auf den Kern der wichtigsten Unterstützer einschränken.

Zuallererst muss ich mich bei meinem Betreuer, Prof. Wolfgang E. Ernst bedanken der vor allem mit seiner Geduld dieses Projekt am laufen halten konnte. Ich bin mir sicher, dass eine Maschine welche SO oft SO katastrophal Schaden erleidet/verursacht, auf den meisten anderen Institutionen aufgegeben worden wäre. Umso mehr will ich auch den vergangenen Mitarbeitern am Projekt, Michael Mayrhofer-Reinhartshuber und Anton Tamtögl danken, welche nicht nur H.Å.N.S. zur Vervollständigung, sondern auch mich durch die ersten Jahre brachten, in denen ich die Methode zu verstehen lernen versuchte. Mike und ich sind schon seit dem ersten Semester gute Freunde, wo wir uns ein Zimmer im wohl schrecklichsten Studentenheim von Graz teilten. Ich glaube nicht dass meine Studienzeit die selbe gewesen wäre, wenn wir die nächtlichen Lineare Algebra Lernsessions bis 3 Uhr morgens (und mit reichlich Mirto...), oder die regelmäßigen Go Sessions vor dem Gebäude ausgelassen hätten. Ich bin weiters davon übrezeugt, dass der Optimismus und die generelle Abneigung uns selbst zu ernst zu ernst zu nehmen, welche in dieser Gruppenkonstelation herrschte, Toni davor bewahrte sein Doktorat aus Frustration aufzugeben. Toni war der beste *Captain* den man sich vorstellen kann und nur durch seine Ausdauer bei den immer wieder anfallenden Reparaturarbeiten ermöglichte

"Piled Higher and Deeper" by Jorge Cham, www.phdcomics.com

uns, unser kleines *UHV-Piraten-U-Boot* durch die Untiefen in den sicheren Hafen der Veröffentlichungen zu schiffen. Der Verlust meiner Teamkollegen ende 2013 traf mich schwer, doch traten an ihre Stelle Florian Apolloner und Christian Gösweiner, welche ihren Wert als zukünftige Oberflächenphysiker schon lange bewiesen haben und mehr als gewillt erscheinen, den Geist der *He-Surfer* weiterzutragen.

Die Einführung von Petra und Alicia, unsere viel geliebten Kaffeemaschinen, führte zu häufiger und umfangreicher sozialer Interaktion, was mehr ist als man laut gängigen Vorurteilen auf einem Physikinstitut erwarten kann. Diese wertvollen Kaffeepausen führten zu umfangreichen Diskussionen über das Doktorandenleben und Outdoor-Aktivitäten mit Michaela Ellmeier und Günter Krois, denen ich auch für viele, sehr *österreichische* Diskussionen im Stil á la *'Lebe jeden Tag als wäre es dein letzter - unter vielem jammern, weinen und generellem Selbstmitleid'*.

Eines der Ereignisse, welches langfristig gesehen die Richtung unserer Forschung am meisten prägte war der erste Besuch von Prof. Giorgio Benedek wenige Wochen nachdem ich mit meiner Masterarbeit an diesem Projekt begonnen hatte. Sein Einfluss und seine permanente Hilfestellung bei den absurdesten Fragestellungen ermutigte uns, dem PCAM Doktorat beizutreten und ermöglichte mir nicht nur mit ihm in Mailand zu arbeiten, sondern auch meinen sechsmonatigen Forschungsaufenthalt in San Sebastián. Ohne Prof. Benedek's Ratschläge und häufige, geduldige Antworten auf meine oft trivialen Fragen wäre das Thema der Oberflächeninteraktion sowie das der Oberflächenresonanzen wohl vollständig an uns vorübergegangen. Durch Prof. Benedek hatte ich das Vergnügen Davide Campi zu treffen, den ich für immer als den DFT-Hexenmeister ansehen werde, der er wirklich ist - auch wenn er sein eigenes Talent nur zu häufig herunterspielt. Während meines Aufenthaltes in Spanien hatte ich Gelegenheit, Prof. Salvador Miret-Artés kennenzulernen, welcher uns an den *close-coupling* Formalismus heranführte, der jetzt das Rückrad dieser vorliegenden Arbeit ausmacht. Das Wiederbeleben und Erweitern seines *Fortran*-Codes war abenteuerlich, auch wenn man auf dem Weg auf Probleme stößt, welche an der Wissenschaft anscheinend so gewöhnlich sind,

dass sie sogar in manchen Webcomics (abgebildet von www.PhDcomics.com) thematisiert werden. Während dieser gesamten Zeit war ich anhängig von viel finanzieller Unterstützung von außen und vieles dieser Arbeit währe auf gar keinen Fall möglich gewesen, wenn die vielen Reisekostenanträge ect. nicht auf fruchtbaren Boden gefallen wären. Somit will ich hier auch dem TU Graz Büro für Internationale Beziehungen, dem ÖFG und vor allem der Industriellenvereinigung Kärnten danken, deren überaus großzügige Unterstützung diese Arbeit erst möglich machten. Weiters will ich den Mitarbeitern des Sekretariats, der Mechanischen- und der Elektro-Werkstatt danken, ohne die weder die Organisation noch die Realisierung eines so großen Projektes wie H.Å.N.S. vorstellbar wäre.
Hier am Schluss will ich meiner Familie danken, welche zuerst geduldig genug waren mich durch die Schule zu bringen und sich danach bei den Heimbesuchen immer mehr Dinge anhören mussten, die eigentlich nur Physiker interessieren können. Zu guter Letzt will ich noch Heike, meiner Freundin, besten Freundin und Partnerin danken, die mir immer zuhörte wenn ich etwas zu sagen hatte, und mich immer unterstütze, wenn ich es am meisten brauchte. Danke.

10 Bibliography

[1] C. R. Ast and H. Höchst. Fermi Surface of Bi(111) Measured by Photoemission Spectroscopy. *Phys. Rev. Lett.*, 87:177602–1 – 177602–4, 2001.

[2] C. R. Ast and H. Höchst. Electronic structure of a bismuth bilayer. *Phys. Rev. B*, 67:113102–, 2003.

[3] N. Balak. Charakterisierung, Aufbau und Steuerung einer Ultrahochvakuum Atomstrahlanlage. Master's thesis, Graz University of Technology, 2009.

[4] L. A. Baring, R. R. da Silva, and Y. Kopelevich. Local and Global Superconductivity in Bismuth. *J. Low Temp. Phys.*, 37:889, 2011.

[5] C. S. Barrett, P. Cucka, and K. Haefner. The crystal structure of antimony at 4.2, 78 and 298° K. *Acta Crystallographica*, 16(6):451–453, Jun 1963.

[6] K. Behnia. Elemental Complexity. *Science*, 321:497–498, 2008.

[7] G. Benedek. Van Hove Singularities of the Surface Phonon Density from Inelastic Reflection of Atoms. *Phys. Rev. Lett.*, 35:234–237, Jul 1975.

[8] G. Benedek, M. Bernasconi, V. Chis, E. Chulkov, P. M. Echenique, B. Hellsing, and J. P. Toennies. Theory of surface phonons at metal surfaces: recent advances. *J. Phys.-Cond. Mat.*, 22:084020, 2010.

[9] G. Benedek, G. Brusdeylins, J. P. Toennies, and R. B. Doak. Experimental evidence for kinematical focusing in the inelastic scattering of helium from the NaF(001) surface. *Phys. Rev. B*, 27:2488–2493, Feb 1983.

[10] G. Benedek, P. M. Echenique, J. P. Toennies, and F. Traeger. Atoms riding Rayleigh waves. *J. Phys.-Cond. Mat.*, 22:304016, 2010.

[11] S. Bengió, J. W. Wells, T. K. Kim, G. Zampieri, L. Petaccia, S. Lizzit, and Ph. Hofmann. The structure of Sb(111) determined by photoelectron diffraction. *Surface Science*, 601(14):2908 – 2911, 2007.

[12] G. Bian, T. Miller, and T.-C. Chiang. Passage from Spin-Polarized Surface States to Unpolarized Quantum Well States in Topologically Nontrivial Sb Films. *Phys. Rev. Lett.*, 107(3):036802, July 2011.

[13] G. Bian, X. Wang, Y. Liu, T. Miller, and T.-C. Chiang. Interfacial Protection of Topological Surface States in Ultrathin Sb Films. *Phys. Rev. Lett.*, 108:176401, Apr 2012.

[14] G. Bracco. PhD thesis, University of Genova, 1987.

[15] G. Bracco, M. D'Avanzo, C. Salvo, R. Tatarek, S. Terreni, and F. Tommasini. Observation of Acoustic and Optical Surface Phonons in LiF(001) by Inelastic He Scattering. *Surface Sci.*, 189:684–688, 1987.

[16] J. Braun, P. Ruggerone, G. Zhang, J. P. Toennies, and G. Benedek. Surface phonon dispersion curves of thin Pb films on Cu(111). *Phys. Rev. B*, 79:205423, 2009.

[17] W. Brenig. Multiphonon Resonances in the Debye-Waller Factor of Atom Surface Scattering. *Phys. Rev. Letters*, 92(5):056102, 2004.

[18] G. Brusdeylins, R. B. Doak, and J. P. Toennies. Observation of selective desorption of onephonon inelastically scattered He atoms from a LiF crystal surface. *J. Chem. Phys.*, 75:1784, 1981.

[19] V. Celli, N. Garcia, and J. Hutchison. Interpretation of selective adsorption in atom-surface scattering. *Surface Sci.*, 87:112–128, 1979.

[20] V. Chis, G. Benedek, P. M. Echenique, and E. V. Chulkov. Phonons in ultrathin Bi(111) films: Role of spin-orbit coupling in electron-phonon interaction. *Phys. Rev. B*, 87:075412, 2013.

[21] H. Chow. Atomic band structure effects on resonant scattering of atoms from solid surfaces. *Surface Science*, 66(1):221 – 237, 1977.

[22] M. W. Cole and T. T. Tsong. Bound State vibrational Spectrum of the 3-9 Atom-Surface Interaction. *Surface Sci.*, 69:325–335, 1977.

[23] C.Schwartz, M. W. Cole, and J. Plíva. Semiempirical determination of the atom-surface interaction. *Surface Science*, 75(1):1 – 16, 1978.

[24] A. F. Devonshire. The Interaction of Atoms and Molecules with Solid Surfaces. V. The Diffraction and Reflexion of Molecular Rays. *Proceedings of the Royal Society of London. Series A, Mathematical and Physical Sciences*, 156(887):pp. 37–44, 1936.

[25] D. Eichenauer, U. Harten, J. P. Toennies, and V. Celli. Interaction potential for one-phonon inelastic He-Cu(111) and He-Ag(111) scattering. *Journal of Chemical Physics*, 86(3693):18, 1986.

[26] T. Engel and K. H. Rieder. Structural studies of surfaces with atomic and molecular beam diffraction. In *Structural Studies of Surfaces*, volume 91 of *Springer Tracts in Modern Physics*, pages 55–180. Springer Berlin Heidelberg, 1982.

[27] D. Evans, V. Celli, G. Benedek, J. P. Toennies, and R. B. Doak. Resonance-Enhanced Atom Scattering from Surface Phonons. *Phys. Rev. Lett.*, 50:1854–1857, 1983.

[28] D. Farias and K. H. Rieder. Atomic beam diffraction from solid surfaces. *Reports on Progress in Physics*, 61(12):1575, 1998.

[29] L. Fox. *The Numerical Solution of Two-point Boundary Value Problems*. Oxford University Press, 1957.

[30] G. Armand and J. R. Manson. Scattering of neutral atoms by a periodic potential : the Morse corrugated potential. *J. Phys. France*, 44(4):473–487, 1983.

[31] N. García. The scattering of He atoms from a hard corrugated surface model using the GR method. I. *The Journal of Chemical Physics*, 67(3):897–916, 1977.

[32] N. García and N. Cabrera. New method for solving the scattering of waves from a periodic hard surface: Solutions and numerical comparisons with the various formalisms. *Phys. Rev. B*, 18:576–589, Jul 1978.

[33] R. M. Goodman and G. A. Somorjai. Low-Energy Electron Diffraction Studies of Surface Melting and Freezing of Lead, Bismuth, and Tin Single-Crystal Surfaces. *J. Chem. Phys.*, 52(12):6325–6331, 1970.

[34] D. Gorse, B. Salanon, F. Fabre, A. Kara, J. Perreau, G. Armand, and J. Lapujoulade. Diffraction of Helium from Cu(110), (113), (115), and (117); Interaction Potential and Surface Crystallography. *Surface Science*, 147(147):611–646, 1984.

[35] I. S. Gradshteyn and I. M. Ryzhik. *Table of Integrals, Series and Products*. Academic Press, 7 edition, 2007.

[36] B. Gumhalter. Different aspects of the Debye-Waller factor in various atom-surface scattering theories. *Surface Science*, 347(347):237–248, 1996.

[37] M. Hengsberger, P. Segovia, M. Garnier, D. Purdie, and Y. Baer. Photoemission study of the carrier bands in Bi(111). *Eur. Phys. J. B*, 17:603–608, 2000.

[38] H. Höchst and C. R Ast. The Fermi surfaces of thin Sb(111) films. *Journal of Electron Spectroscopy and Related Phenomena*, 137-140(0):441–444, 2004. ICESS-9 Proceedings of the 9th International Conference on Electronic Spectroscopy and Structure.

[39] Ph. Hofmann. The surfaces of bismuth: Structural and electronic properties. *Prog. Surf. Sci.*, 81:191–245, 2006.

[40] H. Hoinkes. The physical interaction potential of gas atoms with single-crystal surfaces, determined from gas-surface diffraction experiments. *Rev. Mod. Phys.*, 52:933–970, 1980.

[41] H. Hoinkes and H. Wilsch. *Helium Atom Scattering from Surfaces*, chapter 7, pages 113–173. Springer Verlag Berlin Heidelberg New York, 1992.

[42] J. M. Horne, S. C. Yerkes, and D. R. Miller. An Experimental Investigation of the Elastic Scattering of He and H2 from Ag(111). *Surface Sci.*, 93:47–63, 1980.

[43] D. Hsieh, Y. Xia, L. Wray, D. Qian, A. Pal, J. H. Dil, J. Osterwalder, F. Meier, G. Bihlmayer, C. L. Kane, Y. S. Hor, R. J. Cava, and M. Z. Hasan. Observation of Unconventional Quantum Spin Textures in Topological Insulators. *Science*, 323(5916):919–922, 2009.

[44] G. Q. Huang and J. Yang. Surface lattice dynamics and electronâphonon interaction in ultrathin Bi(111) film. *J. Phys.-Cond. Mat.*, 25:175004, 2013.

[45] E. Hulpke and J. Lüdecke. The giant surface phonon anomaly on hydrogen saturated W(110) and Mo(110). *Surf. Sci.*, 287/288(2):837–841, 1993.

[46] R. W. James and N. Tunstall. XXVI. The crystalline structure of antimony. *Philosophical Magazine Series 6*, 40(236):233–239, 1920.

[47] P. K. Johansson and B. N. J. Persson. On the Debye-Waller Factor in Molecular Beam Scattering Experiments. *Solid State Communications*, 36(36):271–273, 1980.

[48] D. S. Kaufman, R. M. Aten, E. H. Conrad, L. R. Allen, and T. Engel. A helium diffraction study of the structure of the Ni(115) surface. *Journal of Chemical Physics*, 86(3682):11, 1986.

[49] T. K. Kim, J. Wells, C. Kirkegaard, Z. Li, S. V. Hoffmann, J. E. Gayone, I. Fernandez-Torrente, P. Häberle, J. I. Pascual, K. T. Moore, A. J. Schwartz, H. He, J. C. H. Spence, K. H. Downing, S. Lazar, F. D. Tichelaar, S. V. Borisenko, M. Knupfer, and Ph. Hofmann. Evidence against a charge density wave on Bi(111). *Phys. Rev. B*, 72(085440):7, 2005.

[50] Ch. Kittel. *Introduction to Solid State Physics.* John Wiley & Sons Inc, 2005.

[51] W. Kohn. Image of the Fermi Surface in the Vibration Spectrum of a Metal. *Phys. Rev. Lett.*, 2(9):393, 1959.

[52] P. Kraus. Measurements of the He-Bi(111)) interaction potential using elastic helium atom scattering. Master's thesis, Graz University of Technology, 2011.

[53] P. Kraus, M. Mayrhofer-Reinhartshuber, Ch. Gösweiner, F. Apolloner, S. Miret-Artés, and W. E. Ernst. A Comparative Study of the He-Sb(111) Interaction Potential from Close-Coupling Calculations and Helium Atom Scattering Experiments. *submitted to Surface Science*, 2014.

[54] P. Kraus, A. Tamtögl, M. Mayrhofer-Reinhartshuber, F. Apolloner, Ch. Gösweiner, S. Miret-Artés, and W. E. Ernst. The surface structure of Bi(111) calculated from Helium Atom Scattering measurements using the inelastic Close Coupling formalism. *Physical Review B*, submitted, 2014.

[55] P. Kraus, A. Tamtögl, M. Mayrhofer-Reinhartshuber, G. Benedek, and W. E. Ernst. Resonance-enhanced inelastic He-atom scattering from subsurface optical phonons of Bi(111). *Phys. Rev. B*, 87:245433, Jun 2013.

[56] S. V. Krishnaswamy, G. Derry, D. Wesner, T. J. O'gorman, and D. R. Frankl. Debye-Waller effects in atom-surface scattering . *Surface Science*, 77(3):493 – 504, 1978.

[57] J. Lapujoulade, Y. Lejay, and N. Papanicolaou. Diffraction of Helium from a stepped Surface: Cu(117)- an experimental study. *Surface Sci.*, 90:133–161, 1979.

[58] J. E. Lennard-Jones and A. F. Devonshire. The Interaction of Atoms and Molecules with Solid Surfaces. VII. The Diffraction of Atoms by a Surface. *Proceedings of the Royal Society of London. Series A-Mathematical and Physical Sciences*, 158(894):253–268, 1937.

[59] A. C. Levi. Quantum Theory of Atom-Surface Scattering: Debye-Waller Factor. *Surface Science*, 88(88):221–254, 1979.

[60] J. R. Manson. Inelastic scattering from surfaces. *Phys. Rev. B*, 43(9):6924–6937, March 1991.

[61] A. A. Maradudin, E. W. Montroll, and G. H. Weiss. *Solid State Physics*, chapter III. Theory of Lattice Dynamics in the Harmonic Approximation, page chapter III. Academic, New York, 1963.

[62] R. Martínez-Casado, G. Mallia, D. Usvyat, L. Maschio, and S. Casassa. He-atom scattering from MgO(100): calculating diffraction peak intensities with a semi ab initio potential. *Phys. Chem. Chem. Phys.*, 13(14750):7, 2011.

[63] R. Martínez-Casado, B. Meyer, S. Miret-Artés, F. Traeger, and Ch. Wöll. Diffraction patterns of He atoms from the MgO(100) surface calculated by the close-coupling method. *Journal of Physics: Condensed Matter*, 19(30):305006, 2007.

[64] R. Martínez-Casado, S. Miret-Artés, B. Meyer, F. Traeger, and Ch. Wöll. He atom scattering from ZnO surfaces: calculation of Diffraction peak intensities using the close-coupling approach. *J. Phys. Cond. Mat.*, 22(30):304011, 2010.

[65] R. Martínez-Casado, D. Usvyat, L. Maschio, G. Mallia, S. Casassa, J. Ellis, M. Schütz, and N. M. Harrison. Approaching an exact treatment of electronic correlations at solid surfaces: The binding energy of the lowest bound state of helium adsorbed on MgO(100). *Phys. Rev. B*, 89(205138):7, 2014.

[66] B. F. Mason and B. R. Williams. The inelstic scattering of He and Ne from a (001) surface of sodium fluoride. *Journal of Chemical Physics*, 61(2765), 1974.

[67] L. Mattera, F. Rosatelli, C. Salvo, F. Tommasini, U. Valbusa, and G. Vidali. Selective adsorption of 1 H2 and 2 H2 on the (0001) graphite surface. *Surface Science*, 93(2):515–525, 1980.

[68] M. Mayrhofer-Reinhartshuber. Helium Atom Scattering from Surfaces including the Pseudo Random Chopper Technique. Master's thesis, Graz University of Technology, 2010.

[69] M. Mayrhofer-Reinhartshuber, P. Kraus, A. Tamtögl, S. Miret-Artés, and W. E. Ernst. Helium-surface interaction potential of Sb(111) from scattering experiments and close-coupling calculations. *Phys. Rev. B*, 88:205425, Nov 2013.

[70] M. Mayrhofer-Reinhartshuber, A. Tamtögl, P. Kraus, and W. E. Ernst. Helium atom scattering investigation ofÂ the Sb(111) surface. *J. Phys.: Condens. Matter*, 25(39):395002, 2013.

[71] M. Mayrhofer-Reinhartshuber, A. Tamtögl, P. Kraus, K. H. Rieder, and W. E. Ernst. Vibrational dynamics and surface structure of Bi(111) from helium atom scattering measurements. *J. Phys.-Cond. Mat.*, 24:035410, 2012.

[72] D. R. Miller. *Atomic and Molecular Beam Methods*, ed. G. Scoles, volume 1, chapter 2, pages 14–53. Oxford University Press, 1983.

[73] S. Miret-Artés. Resonant inelastic scattering of atoms from surfaces. *Surf. Sci.*, 339(339):205–220, 1995.

[74] S. Miret-Artes, J. P. Toennies, and G. Witte. Surface-scattering study of the interaction potential of He atoms with the step edges of the Cu(211) and Cu(511) vicinal surfaces. *Phys. Rev. B*, 54:5881–5892, Aug 1996.

[75] H. Mönig, J. Sun, M. Yu. Koroteev, G. Bihlmayer, J. Wells, E. V. Chulkov, K. Pohl, and Ph. Hofmann. Structure of the (111) surface of bismuth: LEED analysis and first-principles calculations. *Phys. Rev. B*, 72:085410, Aug 2005.

[76] F. M. Muntyanu, A. Gilewski, K. Nenkov, A. Zaleski, and V. Chistol. Superconducting crystallite interfaces with Tc up to 21 K in Bi and Bi-Sb bicrystals of inclination type. *Solid State Commun.*, 147(5-6):183–185, August 2008.

[77] A. Ogg. XV. The crystalline structure of antimony and bismuth. *Philosophical Magazine Series 6*, 42(247):163–166, 1921.

[78] K. G. Ramanathan and T. M. Srinivasan. Specific Heat of Bismuth at Liquid Helium Temperatures. *Phys. Rev.*, 99(2):442–, July 1955.

[79] T. Reisinger, G. Bracco, S. Rehbein, G. Schmahl, W. E. Ernst, and B. Holst. Direct Images of the Virtual Source in a Supersonic Expansion. *J. Phys. Chem. A*, 111(111):12620, 2007.

[80] A. S. Sanz and S. Miret-Artés. Selective adsorption resonances: Quantum and stochastic approaches. *Phys. Rep.*, 451:37, October 2007.

[81] D. Schiferl and C. S. Barrett. The crystal structure of arsenic at 4.2, 78 and 299°K. *Journal of Applied Crystallography*, 2(1):30–36, May 1969.

[82] I. Yu. Sklyadneva, G. Benedek, E. V. Chulkov, P. M. Echenique, R. Heid, K.-P. Bohnen, and J. P. Toennies. Mode-Selected Electron-Phonon Coupling in Superconduccting Pb Nanofilms Determined from He Atoms Scattering. *Phys. Rev. Lett.*, 107:095502, 2011.

[83] G. A. Somorjai. *Chemistry in two Dimensions: Surfaces*. Cornell University, 1981.

[84] W. A. Steele. *The Interaction of Gases with Solid Surfaces*. Pergamon Press Ltd., 1974.

[85] B. Stegemann, C. Ritter, B. Kaiser, and K. Rademann. Characterization of the (0001) cleavage surface of antimony single crystals using scanning probe microscopy: Atomic structure, vacancies, cleavage steps, and twinned interlayers. *Phys. Rev. B*, 69:155432, Apr 2004.

[86] K. Sugawara, T. Sato, S. Souma, T. Takahashi, M. Arai, and T. Sasaki. Fermi Surface and Anisotropic Spin-Orbit Coupling of Sb(111) Studied by Angle-Resolved Photoemission Spectroscopy. *Phys. Rev. Lett.*, 96:046411, Feb 2006.

[87] K. Sugawara, T. Sato, S. Souma, T. Takahashi, M. Arai, and T. Sasaki. Anisotropic spin-orbit interaction in Sb(111) surface studied by high-resolution angle-resolved photoemission spectroscopy . *Journal of Magnetism and Magnetic Materials*, 310(2, Part 3):2177 – 2179, 2007.

[88] A. Tamtögl. *Surface Dynamics and Structure of Bi(111) from Helium Atom Scattering.* PhD thesis, Graz University of Technology, 2012.

[89] A. Tamtögl, P. Kraus, M. Mayrhofer-Reinhartshuber, D. Campi, M. Bernasconi, G. Benedek, and W. E. Ernst. Erratum: Surface and subsurface phonons of Bi(111) measured with helium atom scattering. *Phys. Rev. B*, 87:035410(E), 2013.

[90] A. Tamtögl, P. Kraus, M. Mayrhofer-Reinhartshuber, D. Campi, M. Bernasconi, G. Benedek, and W. E. Ernst. Surface and subsurface phonons of Bi(111) measured with helium atom scattering. *Phys. Rev. B*, 87:035410, 2013.

[91] A. Tamtögl, M. Mayrhofer-Reinhartshuber, N. Balak, W. E. Ernst, and K. H. Rieder. Elastic and inelastic scattering of He atoms from Bi(111). *J. Phys.-Cond. Mat.*, 22:1–6, 2010.

[92] A. Tamtögl, M. Mayrhofer-Reinhartshuber, P. Kraus, and W. E. Ernst. Surface Debye temperature and vibrational dynamics of Antimony(111) from helium atom scattering measurements. *Surface Science*, 617(0):225 – 228, 2013.

[93] M. Tian, N. Kumar, M. H. W. Chan, and T. E. Mallouk. Evidence of local superconductivity in granular Bi nanowires fabricated by electrodisposition. *Phys. Rev. B*, 78:045417, 2008.

[94] M. Tian, J. Wang, Qi Zhang, N. Kumar, T. E. Mallouk, and M. H. W. Chan. Superconductivity and Quantum Oscillations in Crystalline Bi Nanowire. *Nano Letters*, 9(9):3196â3202, 2009.

[95] A. Tsuchida. Scattering of molecules by a crystal surface: I. He and LiF surface. *Surface Science*, 14(2):375 – 394, 1969.

[96] F. C. M. J. M. van Delft. Bulk and surface Debye temperatures in relation to cohesive energy and Lennard-Jones potentials. *Surface Science*, 251/252:690–695, 1991.

[97] G. Vidali and Ch. Hutchings. Measurement of the Debye-Waller factor for He-LiF(001). *Phys. Rev. B*, 37(17):10374, 1988.

[98] C. Vossloh, M. Holdenried, and H. Micklitz. Influence of cluster size on the normal- and superconducting-state properties of granular Bi films. *Phys. Rev. B*, 58:12422–12426, 1998.

[99] A. Šiber and B. Gumhalter. Debye-Waller factor in He-Cu(001) collisions revisited: the role of the interaction potentials. *Surface Science*, 385(385):270–280, 1997.

[100] B. Weitzel and H. Micklitz. Superconductivity in Granular Systems Built from Well-Defined Rhombohedreal Bi Clusters: Evidence for Bi-Surface Superconductivity. *Phys. Rev. Lett.*, 66:385–388, 1991.

[101] J. Wittig. Zur Supraleitung von Germanium und Silizium unter hohem Druck. *Zeitschrift für Physik*, 195:215–227, 1966.

[102] H. Zhang, C.-X. Liu, X.-L. Qi, Xi Dai, Z. Fang, and S.-C. Zhang. Topological insulators in Bi2Se3, Bi2Te3 and Sb2Te3 with a single Dirac cone on the surface. *Nature Physics*, 5:438–442, 2009.

[103] X. Zhu, L. Santos, C. Howard, R. Sankar, F. C. Chou, C. Chamon, and M. El-Batanouny. Electron-Phonon Coupling on the Surface of the Topological Insulator Bi2Se3 Determined from Surface-Phonon Dispersion Measurements. *Phys. Rev. Lett.*, 108:185501, 2012.

[104] X. Zhu, L. Santos, R. Sankar, S. Chikara, C. Howard, F. C. Chou, C. Chamon, and M. El-Batanouny. Interaction of Phonons and Dirac Fermions on the Surface of Bi2Se3 : A Strong Kohn Anomaly. *Phys. Rev. Lett.*, 107:186102–1–5, 2011.